PhD program in Astronomy, Astrophysics and Space Science

XXXII Cycle

The Explosion of Massive Stars and Their Compact Remnant

PhD Thesis

PhD Student	**Supervisors**
Alessio Marino	Prof. Marco Limongi
	Prof. Luigi Stella

Academic Year 2018/2019

Contents

Abstract

Massive stars ($M \geq 8M_\odot$) end their life exploding as Core Collapse Supernovae (CCSN). As a result of such a kind of explosions, a very dense and compact remnant, either a Neutron Star (NS) or a Black Hole (BH), is left. The understanding of how the remnant is formed and how its mass is linked with the properties of both the progenitor star (initial mass and initial metallicity) and the explosion (explosion energy, light curve and spectra) is fundamental in several astrophysical areas: for example, the formation of high massive remnants (1) limits the ejection of the heavy elements produced during either the hydrostatic and explosive nucleosynthesis and therefore this may have a significant impact on the chemical evolution of the galaxies as well as on the behavior of the light curve and spectra; (2) contributes significantly to the population of high mass compact objects, and (3) constitutes potential sources of gravitational waves (GWs) through BH-BH or NS-BH mergers. Unfortunately, at present, there is no self consistent hydrodynamic model for CCSN in which the explosion is obtained naturally and systematically. Even in those few cases where the explosion is successful, the results are not fully compatible with the observations (e.g., the energy of the explosion in these cases is a factor of 3 to 10 lower than that usually observed). In addition, these sophisticated 3D hydro simulations cannot predict with certainty of precision the mass of the remnant. The reason is that the fallback occurs on timescales (few hours) much longer than the typical timescales followed by the hydro calculations (few seconds). For all these reasons, at present, the systematic simulations of CCSNe are are still based on artificially induced explosions. In these calculations an arbitrary amount of energy is injected in the presupernova model (typically close to the edge of the iron core) and the shock wave that is generated in this way is followed during its propagation within the exploding mantle.

In this context we substantially improved the 1D hydrodynamic code (HYPERION), extensively used for the explosive nucleosynthesis calculations (among the others Limongi and Chieffi 2018 [45]), mainly with the inclusion of the radiative transport in the flux limited diffusion approximation and with a better treatment of

the inner boundary conditions. By means of this new version of the code we computed the explosions, and the associated bolometric light curves, remnant masses and explosive nucleosynthesis, of a subset of red super giant presupernova models extracted from the database published by Limongi and Chieffi 2018 [45]. In total 203 explosions have been computed, for different values of the explosion energy. In this way we were able to study the dependence of the light curve behavior (the maximum luminosity, the luminosity at 50 days, the plateau duration, the radioactive tail) and the mass of the remnant on the properties of the progenitor star (mass, metallicity) and on the explosion energy. Such a theoretical predictions constitute a fundamental reference framework for the interpretation of a number of astrophysical topical subjects among which the gravitational waves and their sources.

Chapter 1

Introduction

1.1 Massive Stars

The stars are similar to the cells of the human body: they are the fundamental building blocks of some larger structures (the galaxies), they are a source of energy and, just as human cells, they have a life-cycle as summarized in figure 1.1. The stars act as enormous powerhouses obtaining energy by nuclear reactions: in the core, indeed, temperatures and densities are so high to win the electromagnetic repulsion of two nuclei which are put close enough (with some assistance form the quantistic tunnel effect) to merge into an heavier nucleus. This kind of processes free a certain amount of energy: the difference in mass between the reagents and the products in the reaction is transformed in energy according to the well known formula $E_r = \sqrt{(m_0c^2)^2 + (pc)^2}$ (m_0 and p are respectively the rest mass and the momentum of the particle, and c is the light speed in void). This energy is necessary for the stellar structure to maintain its high pressure gradient and avoid the collapse under its own self-gravity. The nuclear reactions continue until the exhaustion of the chemical fuel in the core: then the core undergoes to a new contraction due to the weakening of the pressure gradient. This contraction increases the temperature and the density of the core, allowing new chemical reactions involving heavier nuclei, while the lighter elements keep on burning in the outer layers of the structure: this is how the hydrostatic nucleosynthesis works. The initial fuel of this process is the Hydrogen while the last product could be the Iron, but this depends on mass of the star. Indeed, the mass is the fundamental physical parameter which determines the evolution of a star: in objects with an initial mass inferior to 8 $M_\odot$ the inner physical quantity would not reach the conditions to ignite some further nuclear reactions for heavy elements. This because temperature and density values allow the onset of high
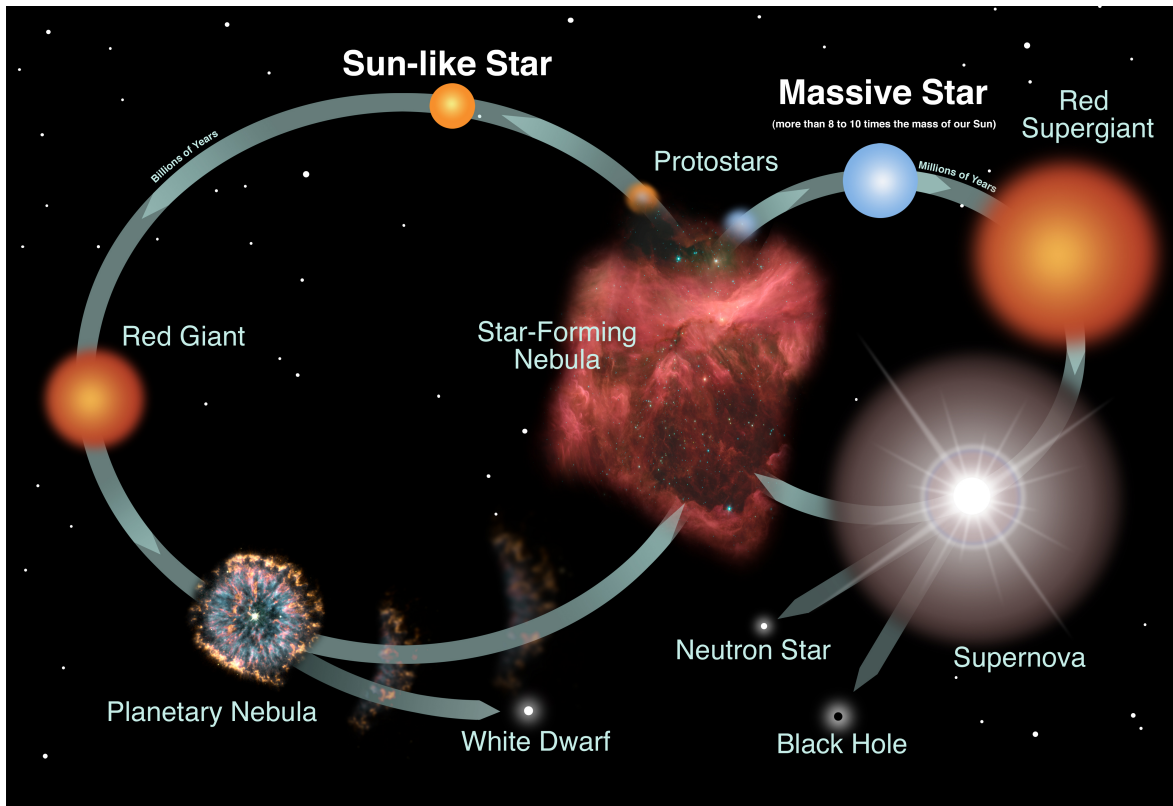
Figure 1.1: The life-cycle of the stars: their fate is determined by the mass of the stellar structure which can lead to a Supernova or to a white dwarf. The figure also shows the typical timescales of the stellar evolution. (Credit: NASA and the Night Sky Network)

values of electronic degeneracy which halts the collapsing process. In this way the star ends its life as a white dwarf, a cooling structure sustained only by the electronic degeneracy pressure (figure 1.1).

For stellar masses higher than 8 $M_\odot$, electron degeneracy only plays a marginal role, and it is possible to reach the formation of an Iron core: if we could take a snapshot of the inner parts of a massive fully evolved star we would see the typical onion structure with different layers burning different chemical elements as shown in figure 1.2.
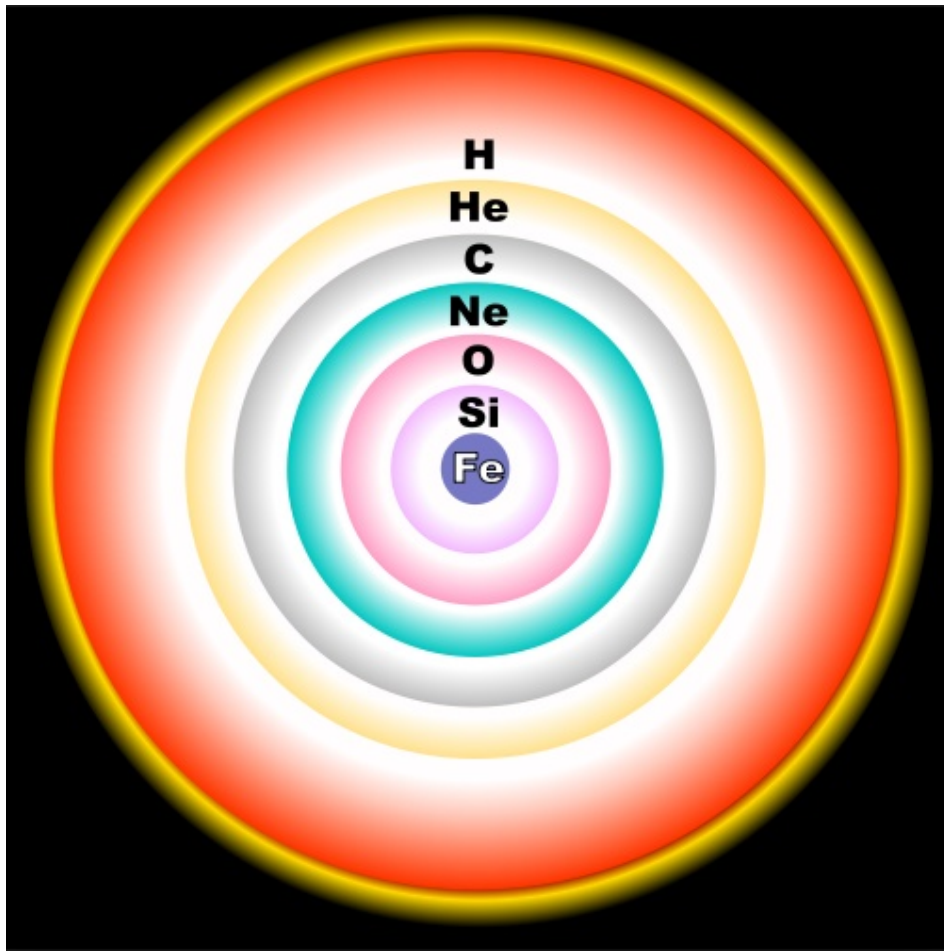
Figure 1.2: Not-in-scale representation of the onion structure of a fully evolved star, this could be a picture of the last stable moments during the life of a massive star. The lighter elements are floating on the heavier ones. (figure taken from the website http://hildaandtrojanasteroids.net)

As the Silicon (the last possible fuel) is exhausted within the core, no more energy can be used to maintain the pressure gradient. The lack of a pressure gradient makes the structure collapse and bounce on a dense proto-neutron star, in a complex, and still unclear, series of events. The structure explodes releasing a huge amount of energy. This event is called Supernova (from now on SN), or better Core Collapse Supernova (CCSN) because the explosion arises from the collapse of the stellar core.

During this destructive phenomenon the external layers of the star are launched towards the outer space as ejecta, while the iron core (and some of the most internal layers of the mantle of the star) remains as a dense and compact body which is the star remnant (SR). CCSNe are fundamental in the life-cycle of the stars: the ejecta, getting colder, can become new molecular clouds which are the suitable environment for star formation, and also the kinetic energy released during the explosion could be the dynamic trigger of star formation (figure 1.1).

Particular attention requires the explosion of stars with masses higher than 140 $M_\odot$: these structures do not explode as CCSNe but instead undergo a process in which the supporting pressure is removed by pairs (e^+,e^-) formed by extremely high energetic photons. This process is called pair instability and it causes the progenitor star to be completely destroyed during the explosive event, leaving no SR behind. The limiting mass of 140 $M_\odot$ depends on physical parameters as the initial metallicty or rotation of the star and should not be considered written in stone. Even in the lower part of the mass range for a CCSNe explosion, it is possible to find some objects between 8 $M_\odot$ and 10 $M_\odot$ which undergo to an electron capture by heavy nuclei. These stars, which can form a degenerated Oxygen-Neon-Magnesium core, are hence deprived of the mobile particles which are the most relevant term of pressure, and thus they are subject to a collapse. The associated CCSN event, in general, results less energetic than the ones obtained by more massive objects but these event are still considered CCSNe. In literature, however, some studies [65] tend to consider also small stars with $8 \pm 1 M_\odot$ as CCSNe, while others [44] prefer to work only with slightly more massive bodies (higher than 13 $M_\odot$).

In this work we will focus on the explosion of massive stars as CCSNe, investigating the different outcomes of these events as the resulting electromagnetic track and compact remnant.

1.2 How does a star explode?

1.2.1 The explosive mechanism

The process known as CCSN is very complicated and still not totally clearly understood in all its stages. The transition from the stable configuration of the star to the violent explosion is the result of the complex interplay among several fields of physics: hydrodynamics, quantum physics, gravitation, general relativity, nuclear

physics, neutrino physics and magnetohydrodynamics. Due to such a complexity, a definitive answer to the question "how does a massive star explode?" is still far from being settled (see, e.g. [66]).

The first studies regarding the nature of CCSNe have been done in 1934 by Baade and Zwicky, who have associated the Supernova event to the transition from the iron core to the compact objects, just few years later from the discovery of a brand new particle in 1932 by Chadwick: the neutron. To the present days further information about CCSNe and their explosive mechanism have been unveiled: we will describe the knowledge obtained so far on this phenomenon.

Once a massive star gets through all the standard nuclear burning stages, its structure consists of a dense Iron core and, above it, a series of envelopes containing progressively lighter elements. The Iron core has a typical mass of about 1.4 $M_\odot$ in which the most internal 0.9 $M_\odot$ are in a degenerate state while the remaining external part is only in a partially degenerate state. From this initial configuration, the Iron core undergoes a further evolution: two phenomena tend to take away energy from the Iron core, depriving it of the necessary pressure to sustain the structure. The first phenomenon (more likely to happen in massive stars, where entropy is high) is the result of the contraction of the Iron core itself which brings the structure to a further rise of temperature and density. This causes changes in the nuclear statistical equilibrium of particles which distribution will favour light particles: in this way the energy obtained in the contraction tends to divide the Iron peak nuclei into light particles. Due to this effect, the gravity is not balanced anymore by the slowly-growing pressure gradient, causing the decrease of the adiabatic index Γ_1. The other concurrent phenomenon (favorite in lower mass stars, where the degeneration is more important), always linked to the gravitational contraction, consists in the rising of the Fermi energy of the degenerate electrons which would increase the captures of electrons by means of free protons: the electrons (which grant the most important term of pressure) are removed and the neutrino emission lowers entropy. This phenomenon allows the onset of low temperatures and high densities, which are the conditions for the electrons to gain a relativistic regime. This process, also, tends to lower Γ_1.

When Γ_1 drops below 4/3, the pressure is not able to sustain the structure anymore and the core becomes unstable, allowing the collapse of the core itself. During the collapse the density increases, causing more electrons to be caught by free protons with heavy neutrino emission. This causes a further decrease of the pressure gradient.

9

After the central density reaches a value of about 10^{12}g/cm^3, the neutrinos begin to be trapped in the central zones and start to diffuse outward through a neutrinosphere, which is located at about 50 km from the center.

As the value of the density exceeds the threshold of $10^{14}g/cm^3$, the matter cannot be compressed anymore. This gives birth to a shock wave direct towards the outer regions of the core that causes an heating and a compression of the matter encountered. During its travel the shock wave loses about $10^{51}ergs$ of energy per each 0.1 $M_\odot$ of matter due to the induction of the photodisintegration of the iron peak nuclei. Because of this energy loss, after $100\,ms$ the shock wave stops its run and stalls at about $200-300\,km$ from the center. This stalling problem of the shock wave is one of the most discussed between astrophysicists: to these days a lot of different physical phenomena have been proposed to give a satisfactory explanation to the processes, which may give the stalling shock wave enough energy to continue its run across the stellar structure. In this work we will focus on the *Neutrino Driven Mechanism* (NDM), the theory which encounters the greatest consent of the scientific community. In the following description we used, as base, some works as [13] and [34].

In the NDM, the neutrinos, which were left behind into the inner part of the proto-neutron star, may be absorbed by free protons and neutrons: to be precise the zone between the neutrinosphere and the stalled shock wave is heated and cooled by neutrino and antineutrino absorption and emission. The two zones of cooling and heating show different radial profiles as reported in figure 1.3. In this way, during a very short time, two different zones (one of cooling, the other of heating) are formed and are separated by a *gain radius*, where there is a match between cooling and heating.

The constant deposition of energy, due to the neutrinos, makes the pressure high enough to pull the shock wave outward again. The neutrino-supported shock wave has now enough energy to propagate through the remaining parts of the star: as it abandons the core, the shock wave encounters the envelopes formed by different layers of processed elements like Silicon, Carbon and Oxygen, Helium and possibly Hydrogen.

To be precise, the NDM is the base for solving the stalling problem of the shock wave, but its action seems to be not enough energetic to completely reignite the explosion. This is the reason why further theories and processes have been proposed to improve the performance of the NDM. We present some of the most important ones, remembering that these processes act together with NDM:
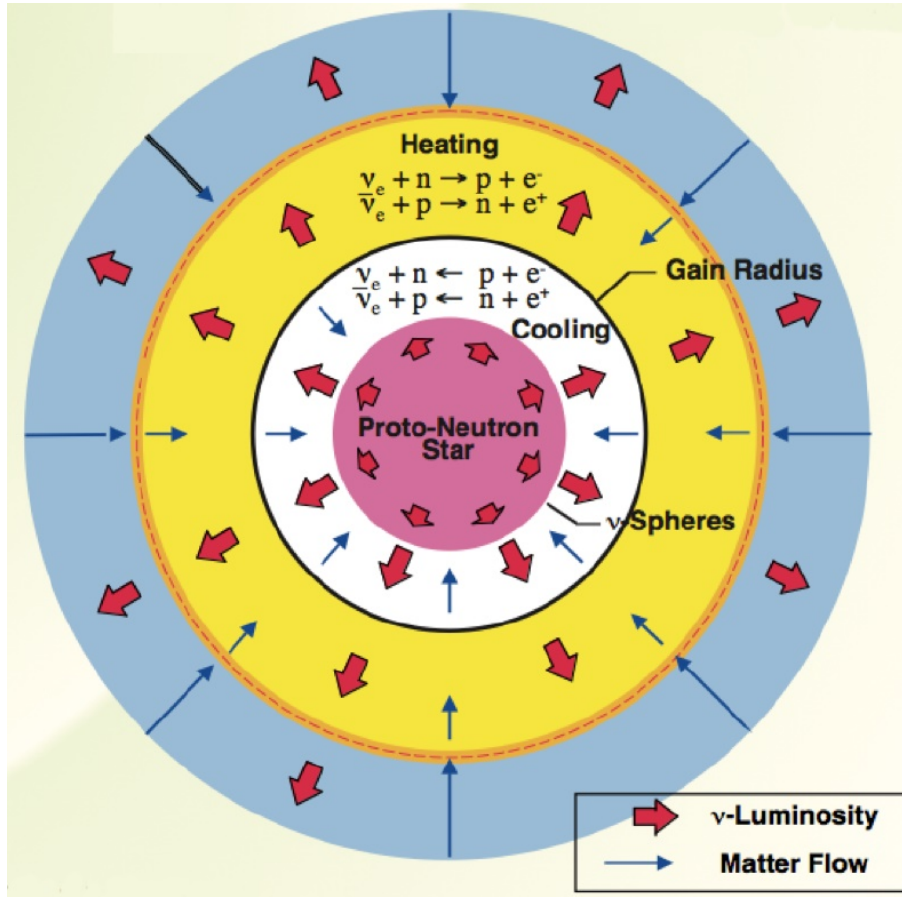
Figure 1.3: The two different radial profiles during neutrino driven mechanism (figure from Forrest M. Hoffman on www.researchgate.net)

-The *Magneto-Hydrodinamical Rotation* involves a rapid rotation of the structure which leads to an amplification of the magnetic field. This would lead to the propagation of powerful magnetic field jets [11].

-The *Acoustic Mechanism* in which the excitation of the proto-neutron star oscillations generate acoustic energy able to reheat the stalled shock wave [10].

-The *Phase Transition Induced Explosion Mechanism* in which a further compacting of the proto-neutron star is caused by a phase transition from hadronic matter

to quark matter [62].

Even if the NDM is the most accepted theory, some problems have been found: for example, the calculation could yield a sufficient explosion energy, but the energy deposition rate is not high enough for the synthesis of ^{56}Ni. In order to resolve this problem, we must take in account a lot of different contributions coming from the rotation of the structure, the asymmetries of the star, the magnetic field or even the uncertainties on neutrino transport. Due to the complexity of the problem, scientists have started to treat it by means of complex 3D simulations that require a lot of computational time.

For example, some recent observations put a light on the possible evidences for asymmetric explosions due to the NDM. Some studies have shown different observational features pointing in this direction: the sudden increase of polarization of the light observed from a supernova explosion after 90 days at the moment of transition from the photospheric phase to the nebular phase [39]; or even the spatial distribution of ^{44}Ti that shows a global asymmetry [31]. These features could be interpreted as the intrinsic asymmetry of the NDM due to the perturbations within the presupernova progenitor.

1.2.2   The fallback

As the shock wave exerts its ram pressure on those parts that are less dense than the core, these regions are pulled away outward like in the general idea of explosion: this process removes the greatest part of the envelope from the star. In this stage of relative short time, resides the *fallback*, which is one of the most important phenomenon regarding the determination of the mass of the stellar remnants. The fallback process has been originally proposed by Colgate in 1971 [15]. As the shock wave reaches the mantle, the latter is subject to a strong impulse which allows it to reach an escape velocity high enough to leave the star. However the inner layers of the escaping envelope are closer to a strong gravity source (the proto-remnant) which exercises an extremely strong attraction. In this way those layers are pulled back by the gravity falling again towards the proto-remnant, adding their mass to it: therefore fallback has a predominant role in determining the mass of the remnant. Two opposing factors contribute to the determination of the fallback and its influence on the remnant: the energy of the explosion and the binding energy of the proto-remnant. The first factor is the energy of the explosion: a more energetic explosion will cause a lighter fallback because a great amount of matter will obtain enough energy to free itself

12

from the gravitational attraction of the proto-remnant. The second factor is the binding energy of the proto-remnant: the more the Carbon-Oxygen core of the star is massive, the more is high the binding energy the remnant, and, at a fixed energy, the more would be the amount of matter involved in the fallback effect. The mass of the Carbon-Oxygen core is linked to the mass of the Helium core and therefore to the Hydrogen one (also considering which kind of nuclear reactions are efficient in the Hydrogen burning stage), and all these quantities depend on the initial mass of the star.

The timescales of the fallback represent a controversial part of the problem: since, as explained above, the exact physical events behind the explosive process are still debated and not totally understood, a theoretical precise determination of timescales of the fallback *a priori* is not possible, also because the observations cannot give us clear information about the event. The only estimates about the subject can be inferred *a posteriori* from the outcomes of the simulations of the explosions. There is a general accordance about the relative short timescale of the fallback compared to other events characteristic of the stellar evolution. More specifically, different studies show uncertainties about two or three orders of magnitude of difference: some authors tend to consider the fallback an effect of shorter duration [80] [26] (as about $20s$), while others thin that the fallback is a more long lasting effect [44] (as even 4-5 hours).

1.3   Compact remnant left by massive stars

As previously mentioned, after the explosion, the progenitor star is separated in two different parts: the SR and the ejecta. The SR is a dense and compact object, which could become a neutron star (NS) or a black hole (BH) according to its final mass: in this work we will only focus on Stellar Black Holes (SBH) which are those bodies potentially born from star progenitors, other kind of black holes will not be treated. We will not discuss here the theoretical features of the compact objects, but as reference it is possible to read [63].

An idea of the effect caused by a CCSN event can be found by observing the Crab Nebula (or NGC 1952) in Taurus constellation 1.4: this structure is formed by huge expanding ejecta (now extended for over $1.84\,pc$, with a mass of $4.6 \pm 1.6\,M_\odot$ [23]) with a velocity of about $1.5\,km/s$. In the center of this structure lies a NS (a pulsar, PSR B0531+21) with a diameter of $28 - 30\,km$ [79].
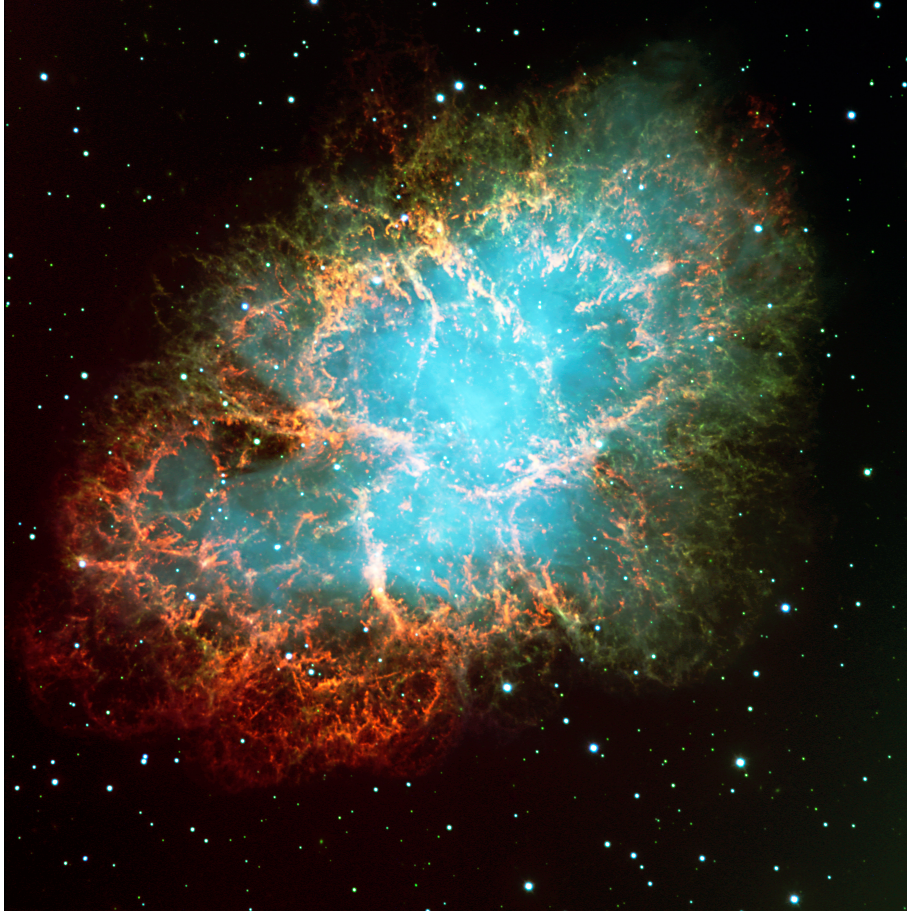
Figure 1.4: Image of the Crab nebula taken with Hubble's WFPC2 camera: it is obtained by assembling 24 individual exposures. Image taken from https://www.spacetelescope.org/images/heic0515a/

Recently the interest about the remnants from massive stars has enormously increased, in particular since the very first two observations of gravitational waves associated to the merging of two rather massive BHs ([1] and [2]). The gravitational wave emission from compact objects could be generated at the moment of the formation of SRs (i.e. during the CCSN explosion) or at later times when two of those compact objects (NS-NS, BH-NS or even BH-BH) may be attracted by the mutual gravitational pull up to the coalescence (the orbit decays due to gravitational wave emission). In general, the coalescence of compact objects releases a huge quantity of energy and, in particular, unequivocal signals of gravitational waves, mostly in

the last moment before the proper coalescence. Even simulations ([58]) show as two identical NSs of mass 1.6 $M_\odot$ with a radius of 15 km could release a peak of luminosity of $10^{55} erg/s$, which is obtained in a timescale of 1 ms. In a similar case the amplitude reaches from GWs is $3 \cdot 10^{-23}$ for an assumed distance of 1 Gpc, with a frequency of 2 kHz.

The compact objects are not only important for the gravitational waves emission, but they are also interesting because they represent some of the most exotic objects in the whole Universe. Within these objects, indeed, it is possible to observe the almost most extreme conditions of matter: these features allow us to study even some manifestations of General Relativity. The physical features proper of the compact objects, indeed, are unreachable on land laboratories and represent some huge sources of information about dense matter and neutrino physics. These objects are also relevant in the *ecology* of the Galaxies, due to the role of CCSNe in the stellar life-cycle: the pollution of heavy elements from CCSNe could be limited by remnants because they can steal some portions of the ejecta, avoiding the spread of high metal-rich matter, affecting the metallicity of possible newborn stars. For this purpose, knowing the mass distribution of stellar remnant could also be an important parameter for galactic evolutionary scenarios, controlling the metallicity of the molecular clouds. Another reason of interest about these objects could be found in gravitational lensing: since their relative high mass is concentrated in such a (relative) small-radius body, SRs tend to modify the neighborhood space, as predicted by GR. In this way, a background passing luminous object could receive an amplification of its luminosity as if the SR would be a magnifying lens: this allows the observer to find even faint or distant objects. SRs could have also a role in Cosmology, since they have being considered Baryonic Dark Matter.

The study of compact objects is fundamental in different branches of the astrophysics (and not only), however it is not easy to accomplish direct measurements on the remnants because of their nature (SBH do not posses even any form of electromagnetic emission), and it is more likely to search for them by looking on the nearby surroundings (as in X-ray binaries, X-ray burst or binary pulsars) to infer the physical properties of each single object. An estimate of their mass could only be obtained by measuring the effects of the compact body on a companion star. Among the several physical features of a dense body the most interesting one is its mass. The mass of a remnant can give us information about the progenitor star and can help us to distinguish whether the body is a NS or a BH.

The NSs show some extreme physical features in stellar structures: their radii are of the order of 10 kilometers, they have a typical density of about $10^{14}g/cm^3$, an hard and solid crust, high rotation frequencies (from 1 to 1000 Hz) and a very intense magnetic field (up to 10^{12} gauss). They start their second life as very hot objects $(T > 10^{10}K)$, but they undergo a quick cooling, due to their neutrino emission, which can lead them to a temperature of $T = 10^9 K$ in about one day and to $T = 10^8 K$ in 100 years [36]. The classification of NSs results to be huge and complicated, we will address below the three most important classes.

The *pulsars* are featured by their rapid rotation and high magnetic field that may bring them to have particular radio emissions. Describing them in a simple way, we can compare them to a lighthouse, therefore we can sense their emission, which often results to be very precise, as a series of pulses.

The *X-ray binaries* are NSs coupled with a low-mass binary companion. The NS may extract some matter from this companion star: if this happens the in-falling matter gains an enormous quantity of energy which results in X-ray emission.

Magnetars are cases in which the NS shows a particularly huge magnetic field (also 10^{15} gauss) and a relatively slow rotation (about $10s$ of periods): the intensity of magnetic field is so strong to cause real *starquakes* that leads to the fracture of the solid crust of the star with the emission of a huge quantity of energy in X or γ-rays. Usually their magnetic field decays within 10^4 years.

Since the very first observations, the mass of the NSs has always been a controversial topic because it exceeds the theoretical limit of 0.7 $M_\odot$ originally proposed by Tolman, Oppenheimer and Volkoff in 1939, but then raised up to 2.17 $M_\odot$ after several years due to the uncertainties on the physical equations (in particular the equation of state) governing the matter in those extreme conditions. The uncertainties are also strengthen by the intrinsic difficulties in obtaining complete data from NS [17]: the determination of the masses of NSs is only possible if they are in a binary system, where we can measure their masses through the dynamical effects caused on the companion. This kind of measurement is not available for the majority of the pulsars: about 90% of radio pulsars are isolated objects [52], therefore it is impossible to collect information about their mass (for a more detailed description of the observational methods, it is possible to read [52]). Recent observations have allowed us to determine the distribution in masses of NSs with a very narrow profile around $1.35M_\odot$ [69], but, as data have increased and become more refined, it has become

clear that the mass distribution is at least bimodal, and it likely has a wide spread ranging from low masses up to the maximum NSs mass limit [61]. High masses seem to be favoured in this distribution by the last measurements of NS [52]. In figure 1.5 is presented a collection of measurements of NSs.

With the support of these measurements we can define the observational mass range for NSs from 1.02 to 2.74 $M_\odot$.

Measuring BH masses it is a very difficult and challenging task: BHs are extremely difficult to disclose due to the lack of electromagnetic emission, furthermore the data about them rely on a complex combination of dynamical (the measurement of the speed of any binary companion may be disturbed by the emission raised by the presence of an accretion disk around the BH or even by the tilting of the system) and spectroscopic data. The uncertainties associated with these measurements are more significant than in the case of NSs. Early analysis argued that the measurements are consistent with a relatively narrow mass distribution [5] around 7.0 $M_\odot$. More recent analysis [21] have found that the statistically favoured models have mass distributions that extend towards high masses ($15 - 20\ M_\odot$), and, also, stated that there is a clear evidence of a low-mass gap in the distribution, with no (or very few since the most recent observations) compact objects found in between the maximum NSs mass (about 2.74 $M_\odot$) and $4.3 - 4.5\ M_\odot$. Figure 1.6 shows some recent determinations of the BH masses.

With these measurements we can define a range for the masses of observed galactic SBH from 4.9 to about 23.0 $M_\odot$. This was the scenario before the first detection of the GWs: according to Abott (2016) [1], the estimations of the masses of the two coalescing BHs are about 36^{+5}_{-4} and $29^{+4}_{-4}\ M_\odot$. This discovery has expanded the observational upper limiting mass of BHs up to about 36 $M_\odot$. It is also possible to define a theoretical upper limiting mass for SBH: since stars with a mass over 140 $M_\odot$ explode as pair instability supernovae (no remnant), it is possible to think to the upper limiting mass for SBH as the mass of the most massive star which collapse directly and all its matter forms a SBH. At this purpose we can consider an 80 $M_\odot$ star as one of the most massive stars exploding as CCSN (beside being the highest mass used in this work): in this way, we can consider 80 $M_\odot$ as a theoretical upper limit for the mass of SBH. From a theoretical point of view we can put a lower mass limit for BHs, considering properly BHs all those dense bodies with a mass superior to the Tolman-Oppenheimer-Volkoff limit.
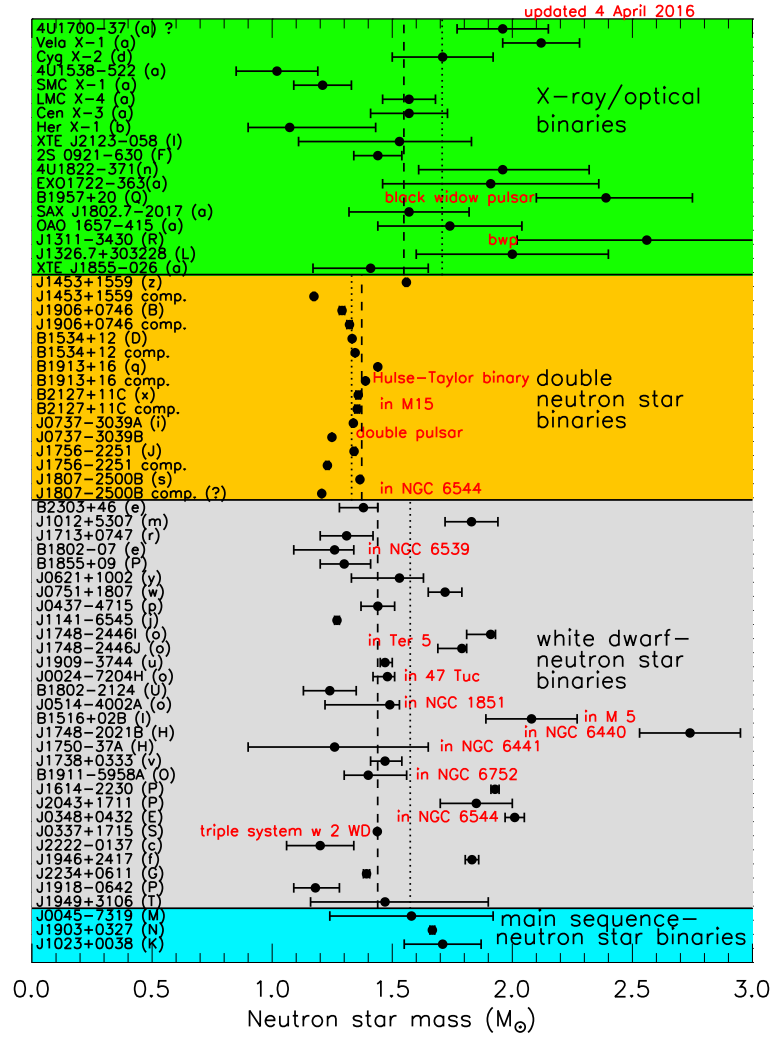
Figure 1.5: Masses of the observed NS, figure taken from [37] updated at April 2016 by https://stellarcollapse.org/nsmasses (here also the references for the single measurements)

18
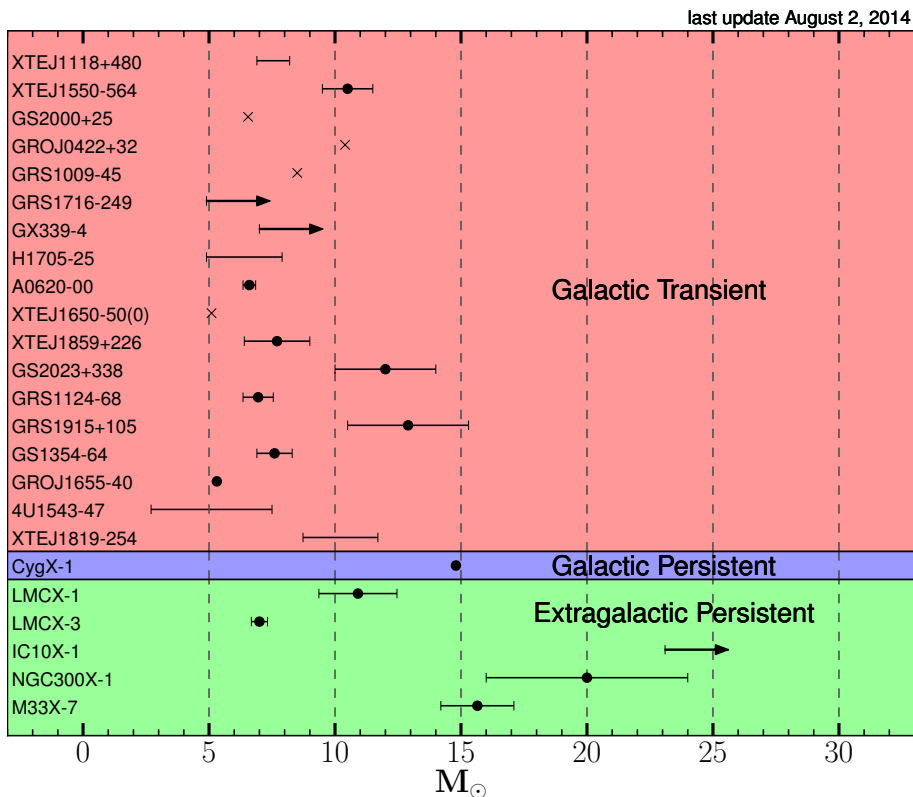
Figure 1.6: Masses of the observed galactic SBH at August 2014, figure taken from https://stellarcollapse.org/bhmasses and references herein

1.4 SNe and CCSNe in the Universe

The name Supernova comes from the latin word *Novus* which means *new*: this is because a Supernova appeared in the night sky as a shiny brand new star, never seen before. Even if the word Supernova has been first used by Baade and Zwicky only in 1934 [51], the observation of such phenomena has been made since ancient Greek times and it has allowed to show that the perfect sphere of the fixed stars was a wrong idea. Therefore the night sky was not perfect and immutable: this view also helped to switch from a Tolemaic-Aristotelic point of view to an Heliocentric one. For these reasons we can guess how much important was the power and the relevance of similar astrophysical events in a time when often stars were the only way to travel or keep orientation.

19

Today the number of observations of SN in the universe has been increased to more than thousands of objects (and will be much more in the next future) [1].

A first empirical classification for SNe has been proposed in 1941 by R. Minkowskii [48] and it acted as base for the current classification. This current classification relies on the properties of both the light curves (LC) and the spectra [25]. Since this first step the empirical classification has been expanded up to reach the current version summarized in figure 1.7. According to this classification, SNe are divided in two main types: Type I and Type II. Type I includes events in which there are no signs of Hydrogen emission or absorption lines in the spectra. It is possible to make a further divisions as Type Ia with no Helium but some Silicon absorption features, Type Ib where the Helium features are shown and Type Ic where no Helium and not even Silicon is found (but in both Type Ib and Type Ic some features of Oxygen, Magnesium or Calcium can be found). On the other hand, the Type II SNe show all strong signs of the presence of Hydrogen, and further classifications (within the Type II SNe) can also derive from the light curves: Type II-P SNe display a constant luminosity that lasts for about 100 days after the peak, while Type II-L SNe show a linear decrease after the peak. There are some further spectral classifications in Type II: the Type IIn SNe which show Hydrogen lines in emission (often with different velocity components and strong narrow profiles), the Type IIb SNe which, at the beginning, show Hydrogen as Type II but have a fast transition with the decreasing of Hydrogen features and the increasing of helium ones. Other rare events may exist showing peculiar behaviours that cannot be included in no one of the previous classes.

Concerning the classification of SNe an important distinction is the theoretical differentiation between thermonuclear and core collapse events. The first class includes the Type Ia SNe in which the explosion is caused by an external accretion of matter. The second class, is represented by the CCSNe, which are the results of a complete evolution of massive stars, and the explosion is reached due to the collapse of the stellar structure under its own gravity.

The various SN types are associated to different stellar progenitors [3]. The most precise and verified coupling between a progenitor and its explosive counterpart is for Type II-P SNe: these events are related to exploding single massive stars with a huge Hydrogen rich envelope, which are typical features of Red Super Giant Stars (from now on RSGs) [65]. More complex, and still uncertain, is the identification

---

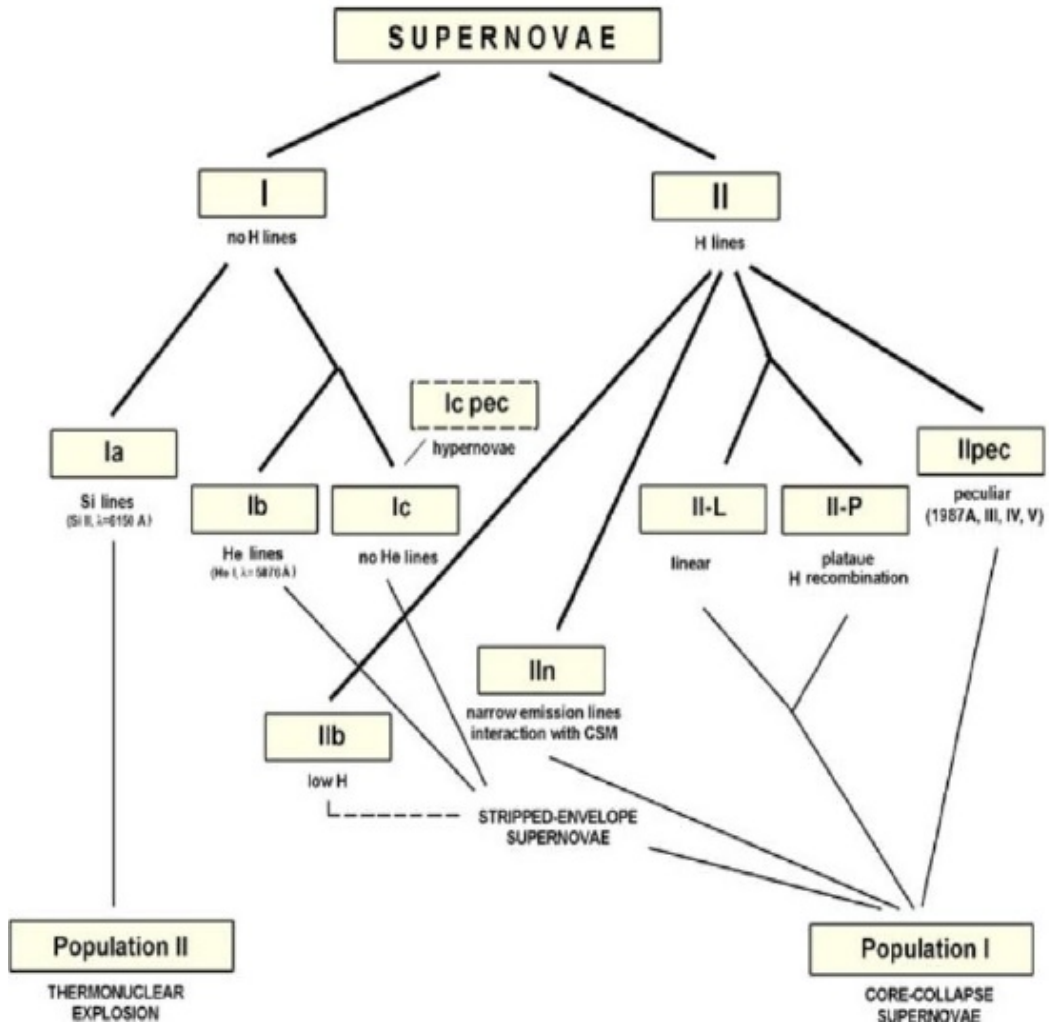[1]Source: https://www.lsst.org/science/transient-optical-sky/supernovae

Figure 1.7: The classification of SNe, this scheme includes Type I and Type II with the different classes (this figure is taken from the website of the University of Belgrade, department of Astronomy)

of the progenitors of Type II-L SNe: there are debates [18] whether they could be Yellow Super Giants (YSGs) or RSGs. In general, it is still not clear, whether they represent a different event from a Type II-P or if they can be the results of an exploding RSGs-like star with a progressively lower amount of Hydrogen in the envelopes. Concerning Type IIb SNe, there are hypothesis that they may descend from YSG with a binary companion [54] (this may explain the presence of Hydrogen lines in the spectra) or even being the transition phase between II-P and Ib SNe [24]. Regarding Type IIn SNe, they seem [28] to be related to the Luminous Blue Variables (LBV). These stars, indeed, are supposed to lose huge quantities of matter (somehow related to a Wolf-Rayet transition): this lost matter is spread as stellar wind from the star, and may be placed in the nearby of the star becoming circum-stellar matter (CSM). The interaction between the CSM and the exploding star could be the cause for the spectral features of this type of SNe. Even for very peculiar object, as the 87A-like events, some explanations have been given: these events seem to be related to Blue Super Giant Stars (BSGs) [4] with the presence of a binary companion, low metallicity or fast rotation [53]. All these features could bring the progenitor star to have a smaller radius compared to RSGs, and cause the absence of any kind of plateau. Other important events are represented by Type Ia SNe. The identification of the progenitors of Type Ia SNe is currently still a debated problem: along with the other models (violent mergers, core-degenerates) some studies, as [9], used a single degenerates, while other works as [41], proposed a double degenerate scenario. The process behind a Type Ia SN is the transfer of matter in a binary star from one companion to the other up to the ignition of Carbon in a degenerate environment. This causes the the star explosion and the expulsion of matter. Sometimes Type Ia SNe are periodical event. They are also used as standard candles because they are very bright and homogeneous, and a precise calibration relation, which has been derived from the observed shapes of the LCs, exists.

Typically, 60-80 SNe events per year can be seen in all those galaxies for which reliable physical parameters i.e. morphology or luminosity are known [70]. It is surprisingly that since the invention of telescopes, no SN (of any sort) has been found in the Milky Way: the expected rate for a SN event to happen in this kind of galaxies is one in about 40 years [68], and, since the last reliable observation in our galaxy is dated 1604, the odds in Milky Way case seem to be sensibly lower.

To talk more in depth of the SN rates, we must introduce a quantity called SN unit (SNu) which is defined as the number of events per century per $10^{10}L_\odot$ in a certain optical band. Mannucci and Della Valle (2005) [46] correlated the luminosity of the galaxies to their mass, and they obtained the SNu for the stellar mass

Table 1.1: SN rates normalized to the stellar mass. The columns indicate (from left to right) the morphology of the galaxies, the SNuM for Ia, the SNuM for Ib/Ic and the SNuM for Type II. Table taken from [46].

Type	Ia (SNuM)	Ib/Ic (SNuM)	II (SNuM)
$E/S0$	$0.044^{+0.016}_{-0.014}$	≤ 0.0093	≤ 0.013
$S0a/b$	$0.065^{+0.027}_{-0.025}$	$0.036^{+0.026}_{-0.018}$	$0.12^{+0.059}_{-0.054}$
Sbc/d	$0.17^{+0.068}_{-0.063}$	$0.12^{+0.074}_{-0.059}$	$0.74^{+0.31}_{-0.30}$
Irr	$0.77^{+0.42}_{-0.31}$	$0.54^{+0.66}_{-0.38}$	$1.7^{+1.4}_{-1.0}$

(SNuM). Considering also the morphology of different galaxies, they calculated the rates reported in table 1.1.

In this work we will only focus on CCSNe, and among them we will deal with the Type II-P, which are the most common CCSNe.

But how do these objects appear to our eyes? It should be enough thinking to the luminosity released in the process: about $10^{10}L_{\odot}$, comparable to the one emitted by a whole galaxy, or thinking about the typical total involved energy, about $10^{53}erg$, or even to the ejecta which can reach velocities as high as $10^4 km/s$ [65] [76]. A typical timescale for a CCSN is about several $10^7 s$ which corresponds to the whole evolution of the phenomenon, but a residual long-term luminosity effect can be observed for even a year. In general this kind of phenomena produce a typical luminosity at peak higher of $10^{43}erg/s$.

The observations of CCSNe events are usually obtained by targets of opportunity. Since there are very few indications of a CCSN explosion (as both neutrino flow or gravitational waves cannot give precise information about the exploding star) it results very challenging to sample a complete explosion since the time of the shock breakout (the first photometric and spectroscopic indication of the explosion). At

present, great portions of the Universe are constantly monitored by Sky Surveys, which record all the changes in the sky (i.e. CLASH [56], CANDELS [32] etc.). A great contribution in this field will be given, starting from 2022, from the Large Synoptic Survey Telescope: this is a huge project of a great terrestrial telescope which will cover over 18.000 deg^2 [2] of the austral hemisphere. This instrument will be used for survey purposes for the 90% of time (the rest 10% will be used for particular circumstances). In general after locating the CCSN, both spectroscopic and photometric follow up are done. In the case of the Type II-P, mostly the photometric data are relevant: generally, the luminosity at different wavelengths is measured with different filters, then they are combined together to build a bolometric LC, as reported in figure 1.8.

The LC, as we will see in Chapter 4, reflects the physical features of the progenitors and the energy of the explosion: this link could be useful to infer the properties of the exploding star like the metallicity, the radius or the mass.

Recent observations (i.e. [57] [29]) have found few supernova-like objects that exceed the typical luminosity ($7 \cdot 10^{43} erg/s$) even of a couple of orders of magnitude more, which are considered super luminous supernovae (SLSN). These phenomena are rare in nearby metal rich and luminous host galaxies [57]. They seem to be related only to Type IIn or Type Ic [30] but the extra luminosity of their electromagnetic emission may suggest some differences in the stellar progenitors respect to the less luminous CCSNe. Even if the number of studied objects is very poor, some information have been found and allowed us to divide the objects in three different classes. The first and most studied class of objects is the SLSN-R, which shows a particularly high amount of energy due to the ^{56}Ni radioactive decay coming from very massive stars and so their luminosity would be constantly sustained by the γ-rays of those unstable isotopes. SLSN-II is the most frequently observed class [30] and it shows heavy features coming from the Hydrogen in the envelope of the stellar progenitor: their increased luminosity would come from a bigger radius than the less luminous counterparts. This feature would allow a more efficiency in the interaction between the Hydrogen-rich envelope and the shock wave coming from below. The less studied and observed class is the SLSN-I: these objects show a very fast evolution with very high luminosity in the peak with huge UV flux and the exhaustion of the effects within 50 days, after this time the LC is only sustained by the radioactive decay. The lack of Hydrogen in the spectra suggests that the progenitor stars would be stripped (without envelope) and particularly hot, and the luminosity of SLSN-Is seems coming from a huge deposition of internal energy into the high velocity Hydrogen-low
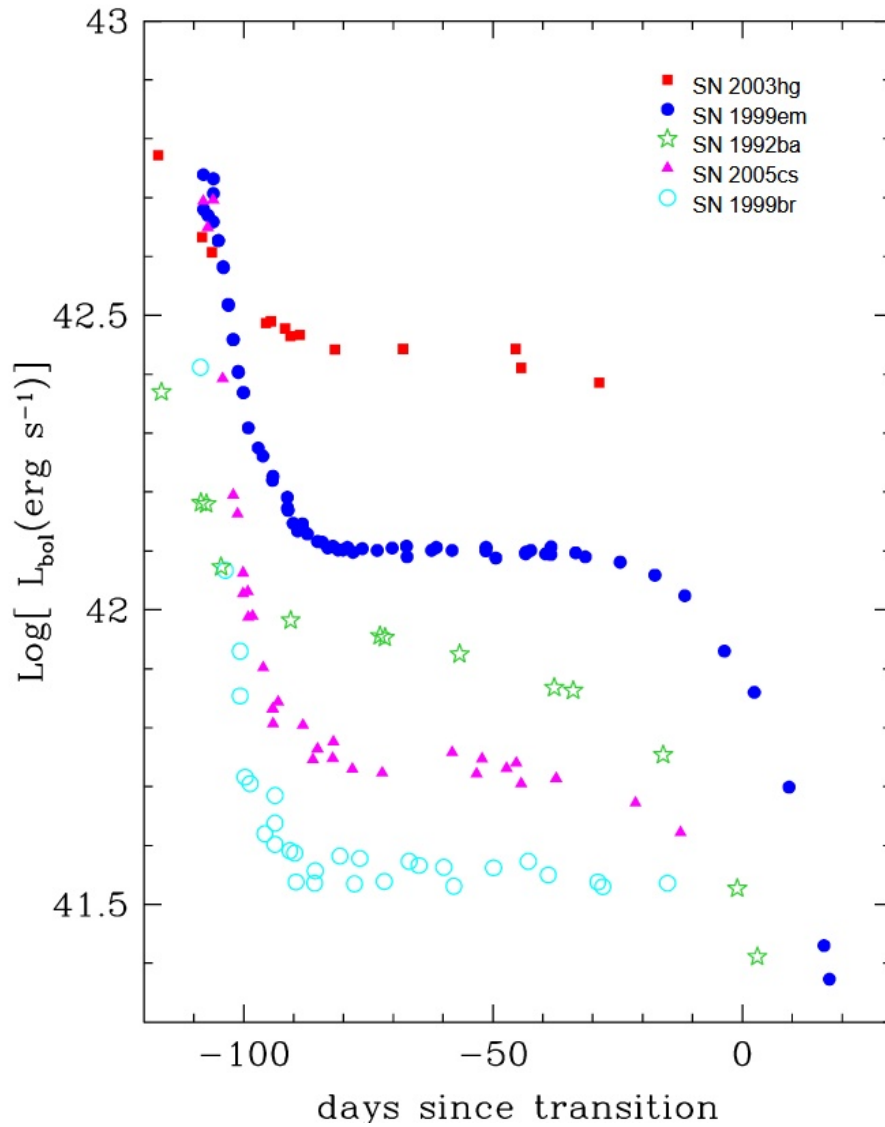
---

[2]www.lsst.org

Figure 1.8: Five different Type II-P CCSNe bolometric LC: it is possible to note the differences in luminosity from each one due to the inner differences of the progenitor stars. Figure taken from [6]

ejecta [12]. Despite all these hypothesis, there is still a veil of uncertainties around these objects which may be solved by further observations or simulations.

1.5   The importance of studying CCSNe

CCSNe are some of the most observed and studied objects in the Universe: because of their brightness they are rather easy to be measured and quite impossible to be ignored. This is the reason why we have a lot of data available regarding these phenomena.

CCSNe have a fundamental role in the life cycle of the stars: as mentioned above, they can be seen as the *last will* of massive stars just before their death. The kinetic energy released in the explosion propagates as a wave in the space and it may encounter a cold molecular cloud: the wave can be the trigger to make the molecular cloud collapse, planting the seeds of newborn stars. Furthermore, the ejecta of CCSNe are full of chemically processed matter (both by the explosion and by hydrostatic nuclear reactions): this metal-rich matter is thrown away from the star during the explosion, and can pollute the neighborhood with metal enriched matter which could be the starting point for the formation of new metal-rich stars.

As already mentioned, CCSNe are not only studied for their remnant, but also the light curves can be a huge source of information: their shape, the luminosity, the steepness of the tail and the peak are the most relevant features which can be analyzed in a LC. The LCs can provide us a lot of data about the physical properties of the progenitor star as its mass range, its radius or even a sort of chemical analysis (presence or absence of Hydrogen or Helium), giving us information about the environment (for example if the progenitor belonged to a stellar cluster) and about its population. Some parts of the LCs can also give us an estimate of the quantity of the radioactive ^{56}Ni formed in the explosion and so further information about the chemical evolution of the exploding object and its interaction with the surrounding space.

One of the most interesting ideas is using II-P LC to infer information by treating them as standard candles, like it happens with Ia at present. In a relatively recent past, Type II-P were already used [60] as standard candles using the Expanding Photosphere Method [59] in which is assumed that a II-P expands its ejecta freely in a homologous expansion. In this way it is possible to measure the photospheric angular size occupied by the structure, the time and the velocity of the expanding ejecta, and it is possible to gain a estimate of the distance. This kind of approach has been surpassed, with apparently better results [33], and now studies are focused on the velocity of expansion of the ejecta, but only in the plateau phase of Type II-P,

obtaining similar results to the ones for obtained for Type Ia. This method is based on the correlation between the velocity of the expansion in the plateau phase and the luminosity of the plateau itself. In particular it results that $v_p \propto L_p^{0.33\pm0.04}$, and, since $L \propto 1/R^2$ (where R is the distance from the observer), with some measurement of the apparent magnitude and velocity of the envelope, it is possible to obtain a precise estimation for the distance. A similar approach can be very useful because CCSNe Type II-P are the most common SNe in the Universe, in this way it is possible to obtain a lot of independent and accurate values for the distances of their host galaxies.

Beside all these reasons, some features of neutrino physics can be studied by means of CCSNe.

1.6 Purpose of this work

We want to study the death of massive stars, focusing on the CCSNe events. In this work we put our attention on two particular outcomes of the explosion: the Stellar Remnant and the Light Curves, and we have investigated them by means of a great number of simulations starting from a huge and extended set of presupernova models provided by Limongi and Chieffi (2018) [45]. To accomplish this task, one of the main goals of this work has been the development of a one-dimensional, Lagrangian hydrodynamic code able to follow a CCSN explosion (starting from the moment when the shock wave leaves the Iron core) and give in return a set of reliable values for the most important outcomes of the explosion. This code has been used on a grid of PSN models to study how the outcomes could be influenced by the features of the progenitor star (mass, initial metallicity, initial rotation velocity) and from the energy of the explosion. As an ideal conclusion of this work some LCs from real observational data have been fitted by means of the outcomes obtained in our simulations: in this way we could obtain some information about the progenitor star.

This thesis is organised as follows. In Chapter 2 we will describe the technical part of the problem, discussing the most important computational problems in simulating CCSNe and then describing the main features of the developed hydrodynamic code and the grid of PSNPs used as starting points. In Chapter 3 we will show the results obtained by all our 203 simulations, including the masses found for the SRs. We will also investigate, according to our models and approximations, the limiting masses of the progenitor to obtain a NS or a BH. In Chapter 4 we will describe in depth a SNII-P LC obtained using our code, explaining the physical processes behind each

part of the LC. We will also study how the LC could be influenced by the features of the stellar progenitor and by the energy of the explosion. Furthermore, the observed LCs of two typical II-P CCSNe (the 1999em and the 2012A) have been reproduced by means of outcomes of our simulations: we will describe our strategy to match observational data and simulations, this allows us to provide information about the stellar progenitors. At last, in Chapter 5, the summary and some conclusions of this work are reported.

Chapter 2

Numerical Methods and Code

2.1   Simulations of CCSNe

Most effort of this work has been devoted to the development of a one-dimensional, Lagrangian hydrodynamic code able to simulate a CCSN event since the moment when the shock wave leaves the Iron core. In this Chapter the main features of the code, as well the numerical and computational techniques, are described in detail: before this, we must spend few words about the general problems concerning this kind of simulations.

One of the critical problems in studying CCSNe is the lack of self consistent models in which the explosion is obtained naturally and in a systematic way. To these days, even using full detailed numerical codes containing, for example, relevant contributions from an improvement of neutrino transport [47] or General Relativity [42], it is extremely difficult to reach a self-consistent explosion from a presupernova model without an external support. Even in the very few cases in which an explosion is correctly reached, the simulations are only able to cover a short period of time (in the order of few seconds) due to their very high computational time cost. Additional problems are also found in the outcomes: the estimates for the energies of the ejecta result to be inferior (even an order of magnitude) respect to the observed values causing some problem is the nucleosynthesis of ^{56}Ni. For those reasons, at present, 1D codes are preferred for systematic works which require a great number of simulations.

The general idea behind a 1D CCSN simulation is the injection, in a presupernova model, a chosen quantity of energy in a given zone generally close to the edge of the

Iron core, that induces the formation of a shock wave, whose propagation is then followed by means of an hydro code.

2.2 Our code

The main goal of this work is to simulate the explosion of a great number of progenitor models and to study the associated remnant mass and light curve. For this reasons we improved the hydro code widely adopted to investigate the explosive nucleosynthesis and the remnants of massive stars. The new code is called HYPERION (HYdrodynamic Ppm Explosion with Radiation DiffusION). This tool has its starting point in a code developed by Limongi and Chieffi (widely described in [43]) able to simulate an adiabatic CCSN event and is the source of several articles (among the others [43], [45]) and has been widely adopted to compute the explosive nucleosynthesis, chemical abundances of massive stars that are used in models of dynamical evolution of galaxies. Furthermore this tool is able to calculate the mass of the SRs, but, due to the nature of adiabatic explosions, it is not able to obtain the light curve generated in the explosion. This is why, we needed to improve the code.

The starting version of the code presented some simplifications about the treatment of gas (considered only as a perfect gas), and neglected some important features as degeneracy or ionization (this because their effects are scarce in an adiabatic explosion environment). We implemented in this code: a more reliable equation of state (EOS), the calculation of the opacities, a radiative transport treatment, an atmosphere tracking and a ^{56}Ni energy deposition strategy have now been included in the code.

2.2.1 The general frame

The computational flow of our code is reported below:

1) We read both a presupernova model and an input file containing the options of the simulation (i.e. the explosion energy, the length of the simulation, some option as the importance of the mixing in chemical composition etc...).

2) After the initial set up, we remove the most internal zones of the star (a portion of the Iron core), then the energy is released and the evolution begins. This energy is given as thermal energy in a shell of 0.1 $M_\odot$ of matter at a mass coordinate of 0.8 $M_\odot$. This allows the shock wave, that is produced in this way, to reach the

edge of the Iron core losing memory of how the energy has been injected. From this moment on, the time is advanced by a Δt and we follow the reaction of the star at the passage of the shock wave: in this way we can update some dynamical quantities as radius, velocity and density. Once these values are updated we can calculate the physical input (opacity, EOS, etc...) and update the equation for the energy and the chemical composition, then the old physical values are substituted by the new ones. The equations describing this process are the mass conservation 2.1, the energy conservation 2.2 and the momentum conservation 2.3 equations.

$$\frac{\partial r}{\partial m} - \frac{1}{4\pi r^2 \rho} = 0 \tag{2.1}$$

$$\frac{\partial E}{\partial t} + 4\pi \frac{\partial (r^2 u p)}{\partial m} - ug - \frac{\partial L}{\partial m} - \epsilon_{Ni} = 0 \tag{2.2}$$

$$\frac{\partial u}{\partial t} + 4\pi r^2 \frac{\partial p}{\partial m} - g = 0 \tag{2.3}$$

In the previous equations (describing the single zone of the star) r is the radius, m is the mass, ρ is the density, E is the total energy per unit mass, u is the velocity, p is the pressure, g is the gravity, ϵ_{Ni} is the energy release due to the ^{56}Ni decay, while L is the radiative luminosity that, assuming a flux-limited diffusion, is given, as in [49], by equation 2.4.

$$L = -(4\pi r^2)^2 \frac{\lambda a c}{3k} \frac{\partial T^4}{\partial m} \tag{2.4}$$

where a is the radiation constant, c is the speed of light and λ is the flux limiter, which is given by (2.5)

$$\lambda = \frac{6 + 3R}{6 + 3R + R^2} \tag{2.5}$$

and R is a quantity defined as

$$R = \frac{4\pi r^2}{kT^4} \left| \frac{\partial T^4}{\partial m} \right| \tag{2.6}$$

while k is Rosseland's mean opacity given by (2.7)

$$\frac{1}{k} = \frac{\pi \int_0^\infty \frac{\partial B_\nu(T)}{\partial T} \frac{1}{k_\nu} d\nu}{4\sigma T^3}. \tag{2.7}$$

In addition to the previous equations, we calculate the explosive nucleosynthesis solving a system of equations 2.8 where its members represent the evolution of each considered nuclear species.

$$\dot{Y}_i = \sum_j c_j(j)\lambda_j Y_j + \sum_{j,k} c_i(j,k)\rho N_A \langle \sigma v \rangle_{j,k} Y_j Y_k + \sum_{j,k,l} c_i(j,k,l)\rho^2 N_A^2 \langle \sigma v \rangle_{j,k,l} Y_j Y_k Y_l$$

(2.8)

where $\dot{Y}_i$ is the time derivative of the abundance in number of the nuclear species i, N_A is the Avogadro number, $c_j(j), c_i(j,k)$ and $c_i(j,k,l)$ are the number of particles created or destroyed in each reaction, λ_i is the rate of $\beta + -$ decays or $e^{\pm}$ captures, Y_j is the chemical abundance of the product element, $\langle \bar{\sigma} v \rangle$ is an indicator of the rate of the reaction. The equation 2.8 describes the evolution of the abundance of each isotope due to β decays, electron capture and photodisintegration (first term) and due to two and three bodies reactions (respectively second and third term).

3) Step 2) is repeated until the desired time length for the event is reached.

To solve this system, we write (introducing $\bar{A}$ as the average value of the surface at the interface) the previous equations as:

$$r_{i+1/2}^{n+1} = r_{i+1/2}^n + \bar{u}_{i+1/2}\Delta t$$

(2.9)

$$\bar{A}_{i+1/2} = \frac{4}{3}\pi \frac{(r_{i+1/2}^{n+1})^2 - (r_{i+1/2}^n)^2}{\bar{u}_{i+1/2}\Delta t}.$$

(2.10)

$$\rho_i^{n+1} = \frac{3\Delta m_i}{4\pi[(r_{i+1/2}^{n+1})^3 - (r_{i-1/2}^n)^3]}.$$

(2.11)

$$u_i^{n+1} = u_i^n + \frac{1}{2}(\bar{A}_{i+1/2} - \bar{A}_{i-1/2})\frac{\Delta t}{\Delta m_i}(\bar{p}_{i-1/2} - \bar{p}_{i+1/2}) + \frac{\Delta t}{2}(g_i^n + g_i^{n+1})$$

(2.12)

$$\frac{E_i^{n+1} - E_i^n}{\Delta t} =$$
$$\frac{\bar{A}_{i-1/2}\bar{u}_{i-1/2}\bar{p}_{i-1/2} - \bar{A}_{i+1/2}\bar{u}_{i+1/2}\bar{p}_{i+1/2}}{\Delta m_i} +$$
$$+ \frac{1}{2}(u_i^{n+1}g_i^{n+1} + u_i^n g_i^n) - \frac{L_{i+1/2}^{n+1} - L_{i-1/2}^n}{\Delta m_i} - \epsilon_{Ni}^{n+1}$$

(2.13)

we must specify that the subscript i refers to the zone-averaged values, while the subscripts $i - 1/2$ and $i + 1/2$ refer to values at left and right-hand interfaces of the zone. The suffix labeled as $n + 1$ is intended for the values at time $t + \Delta t$ while old values at time t are labeled as n. The luminosity and its associated quantities are written as:

$$L_{i+1/2}^n = -\bar{A}_{i+1/2}^2 \left(\frac{1}{k_{i+1/2}}\right)^n \frac{ac\lambda_{i+1/2}^n}{3} \frac{(T_{i+1}^n)^4 - (T_{i-1}^n)^4}{\Delta m_i} \tag{2.14}$$

$$\left(\frac{1}{k_{i+1/2}}\right)^n = \frac{(T_{i+1}^n)^4/k_{i+1}^n + (T_i^n)^4/k_i^n}{(T_{i+1}^n)^4 + (T_i^n)^4} \tag{2.15}$$

$$\lambda_{i+1/2}^n = \frac{6 + 3R_{i+1/2}^n}{6 + 3R_{i+1/2}^n + (R_{i+1/2}^n)^2} \tag{2.16}$$

$$R_{i+1/2}^n = \frac{2\bar{A}_{i+1/2}}{(T_{i+1}^n)^4 + (T_i^n)^4} \frac{|(T_{i+1}^n)^4 - (T_i^n)^4|}{\Delta m_i} \left(\frac{1}{k_{i+1/2}}\right)^n. \tag{2.17}$$

The quantities $\bar{u}$ and $\bar{p}$ are the values of the time averaged velocity and the time averaged pressure at the zone interface, which are obtained by means of the Piecewise Parabolic Method or PPM. First presented by Colella and Woodward [14] this is an high-order enhancement of Godunov's method, which gains more reliability in the treatment of the discontinuities. This numerical method is very complicated and requires different stages to be accomplished; we will give here only the most important information, but a precise and detailed mathematical discussion can be found in [14]. The application of this method requires, at first, an interpolation of distribution of the dependent variables with parabolas using three points of the variables, then we must compute a solution, at the zone edges, as a function of time to the initial value problem implied by the interpolated distributions, using characteristic equations and Riemann solvers. Then we can calculate, with these solutions, the conservatively effective fluxes. The PPM scheme gives us the dynamic evolution of each zone: with the values of $\bar{u}$ and $\bar{p}$ we can calculate the new values of other dynamical variables. With these two values we can update the radius (eq. 2.9) which allows to calculate the evolution for the surface in the interface (eq. 2.10) and for the density (eq. 2.11). At last the velocity in the zone can be updated (eq. 2.12).

With the presented scheme, the PPM can give us the dynamic evolution of each zone: it allows to calculate the whole $'PdV'$ work of the zone caused by the passage of the shock wave. Then to update the energy conservation equation 2.2 we must

include the calculation of the radiative transport. For this task we used the same approach as [49]: we work in Local Thermal Equilibrium (LTE) condition which implies radiation and matter to have the same temperature. This assumption is not strictly true in all the phases of a LC, but a study from Bersten (2010) [7] shows how this assumption is well in agreement with multi-group code for all the duration of the LC. As already mentioned above, to calculate the radiative luminosity L we used a flux-limited diffusion approximation which is satisfied until photon's mean free path is smaller than the typical scale lengths of the system: this means it is well satisfied in the inner zones of the star, while near the surface this approximation drops and we need the flux limiter (2.5) to keep a fine solution and avoiding solving the complete equation for radiative transport. The role of the flux-limiter is to grant continuity in passing from a diffusive to a free streaming flux.

In our numerical scheme, for each time step equations 2.1 and 2.3 are solved separately (as explained in the PPM description) then we solve the equation for the conservation of the energy 2.2 in an iterative way as in a relaxation method coupled with a Newton-Rhapson iterations. To this purpose we give to the equation 2.2 some trial values for the temperature (i.e. the temperature at the previous time step): with those values the equation, likely, will not be solved and some discrepancies may rise between the obtained value and the actual solution of the equation. During the iterations we intend to minimize those discrepancies by adjusting the trial values for the temperature until a numerical (or a computational) tolerance is reached for the whole solution: we will use these reached values as the fitting solution for this time step. During the iterations, for each stellar zone (excluding the border ones which are coupled with boundary conditions) we must also consider in the calculation the values of the previous and the following zones: due to the luminosity description in equation 2.14, it needs three values of the temperature, one in the considered zone and the two in the adjacent ones. This feature leads to a very particular system of equations as a band matrix with only (at maximum) three values different to zero for each line. The associated band matrix can be solved and we obtain the new values for the temperature.

More in details, in the linearized equation for the energy 2.13, we consider the total energy written as:

$$E_i^n = E_{int,i}^n + E_{grav,i}^n + E_{kin,i}^n + E_{rad,i}^n \tag{2.18}$$

we can divide the total energy in different contributes

34

$$E^n_{int,i} = E^n_{int,i} + E^n_{rad,i} \tag{2.19}$$

$$E^n_{grav,i} = -\frac{\Delta t}{2}(u^{n+1}_i g^{n+1}_i + u^n_i g^n_i) \tag{2.20}$$

$$E^n_{kin,i} = \frac{1}{2}(u^n_i)^2 \tag{2.21}$$

where $E^n_{int,i}$, $E^n_{rad,i}$, $E^n_{grav,i}$ and $E^n_{kin,i}$ are respectively the internal, the radiative, the gravitational and the kinetic energy. Considering such a division it is possible to separate the energy contributes in dependent and independent from the temperature: the only temperature dependent contribution is the internal energy, while the others are constant respect to this variable and it is possible to write (from now on we will drop some of the suffixes, for sake of simplicity)

$$M^n_i = E^{n+1}_{kin,i} + E^{n+1}_{grav,i} - E^n_{kin,i} + E^n_{grav,i} \tag{2.22}$$

and adding this term to the other constant (not dependent from the temperature) terms of the equation 2.13 we have

$$C_i = M_i + \frac{\Delta t}{\Delta m_i}(\bar{A}_{i-1/2}\bar{u}_{i-1/2}\bar{P}_{i-1/2} - \bar{A}_{i+1/2}\bar{U}_{i+1/2}\bar{p}_{i+1/2}) + \epsilon_{Ni}. \tag{2.23}$$

In this way we transform 2.13 in 2.24

$$E^{n+1}_{int,i} - E^n_{int,i} = C_i - (L^{n+1}_{i+1/2} - L^{n+1}_{i-1/2})\frac{\Delta t}{\Delta m_i}. \tag{2.24}$$

Now the iterative process is ready to begin: starting from 2.24 the trial values for the temperature (the ones from the presupernova model if is the first time step, or the values at previous time step otherwise) are substituted in this equation. Very likely, these values would not satisfy the equation 2.24 which will not result zero, but some discrepancies Δ_i will raise as shown in equation 2.25.

$$E^{n+1}_{int,i} - E^n_{int,i} - C_i + (L^{n+1}_{i+1/2} - L^{n+1}_{i-1/2})\frac{\Delta t}{\Delta m_i} = \Delta_i. \tag{2.25}$$

At this point, our goal is to minimize the discrepancies at each iteration (until a tolerance is reached) by correcting the trial values of the temperature at each step. To accomplish this we must study how the temperature affects the quantities in 2.25. We found that:

$$k_{i-1/2} = f(\rho_{i-1}, T_{i-1}, T_i) \tag{2.26}$$

$$k_{i+1/2} = f(\rho_i, T_i, T_{i+1}) \tag{2.27}$$

$$\lambda_{i-1/2} = f(T_{i-1}, T_i) \tag{2.28}$$

$$\lambda_{i+1/2} = f(T_i, T_{i+1}) \tag{2.29}$$

$$L_{i-1/2} = f(T_{i-1}, T_i) \tag{2.30}$$

$$L_{i+1/2} = f(T_i, T_{i+1}) \tag{2.31}$$

$$E_{int,i}^n = f(T_i) \tag{2.32}$$

therefore three different temperatures enter in game in our numerical scheme, and three different derivatives must be taken in account to minimize the Δ_i as reported in 2.33

$$d\Delta_i = \frac{\partial \Delta_i}{\partial T_{i-1}} \Delta T_{i-1} + \frac{\partial \Delta_i}{\partial T_i} \Delta T_i + \frac{\partial \Delta_i}{\partial T_{i+1}} \Delta T_{i+1}. \tag{2.33}$$

At this point we calculated all the derivatives necessaries to complete the whole expression of those terms: the general mathematics expression of these quantities is very complicated because temperature affects also opacity and flux limiter in the luminosity description. We found that a good convergence in our calculations can be found even neglecting the contributes in the derivatives from opacity and flux limiter: to these purposes we used the following terms (a similar procedure have been used by Morozova and Piro (2015) [49]):

$$\frac{\partial \Delta_i}{\partial T_{i-1}} \Delta T_{i-1} = -4\bar{A}_{i-1/2}^2 \left(\frac{1}{k_{i-1/2}} \right) \frac{ac\lambda_{i-1/2} T_{i-1}^3}{3\Delta m_i} \frac{\Delta t}{\Delta m_i} \tag{2.34}$$

$$\frac{\partial \Delta_i}{\partial T_i} \Delta T_i =$$

$$\frac{\delta(E_{int,i}^{n+1} - E_{int,i}^n)}{\delta T_i} + 4\bar{A}_{i+1/2}^2 \left(\frac{1}{k_{i+1/2}}\right) \frac{ac\lambda_{i+1/2}T_i^3}{3\Delta m_{i+1}} \frac{\Delta t}{\Delta m_i} \qquad (2.35)$$

$$+ 4\bar{A}_{i-1/2}^2 \left(\frac{1}{k_{i-1/2}}\right) \frac{ac\lambda_{i-1/2}T_i^3}{3\Delta m_i} \frac{\Delta t}{\Delta m_i}$$

$$\frac{\partial \Delta_i}{\partial T_{i+1}} \Delta T_{i+1} = -4 \cdot \bar{A}_{i+1/2}^2 \left(\frac{1}{k_{i+1/2}}\right) \frac{ac\lambda_{i+1/2}T_{i+1}^3}{3\Delta m_{i+1}} \frac{\Delta t}{\Delta m_i}. \qquad (2.36)$$

Considering only three values (T_{i-1}, T_i and T_{i+1}) the matrix associated to this system of equations, altought being very huge, would be different to zero only in a narrow band of three elements across the diagonal line of the matrix as in the figure 2.1.

$$\begin{pmatrix}
B_1 & A_1 & 0 & 0 & \cdots & 0 \\
C_2 & B_2 & A_2 & 0\cdots & 0 & \\
0 & C_3 & B_3 & A_3 & \cdots & 0 \\
\cdots & \cdots & \cdots & \cdots & \cdots & \cdots \\
0 & \cdots & 0 & C_{n-1} & B_{n-1} & A_{n-1} \\
0 & \cdots & 0 & 0 & C_n & B_n
\end{pmatrix}$$

Figure 2.1: A band matrix, similar to the one associated to our system of equations

Taking into account also the boundary conditions of $L = 0$ at the center of the star, and $\frac{dT}{dm} = 0$ at the very top of the stellar atmosphere, the system can be fully solved and new values for the temperature are obtained for each zone of the star. To achieve the solution of the system, it is necessary to invert the diagonal matrix we associated to the system. Such a goal is reached by means of two steps, that are suitable for the particular structure of the matrix itself. The first consists in writing the matrix into a Compressed Sparse Row (CSR) format: in this format the matrix is substituted by three arrays, where the first contains all the values of the non-zero terms of the matrix, the second array keeps in account a sort of progressive number

of non-zero elements present in each row, and the third contains the column index (in the matrix) of each element present is the first array. Once the matrix is set in this way, it can be solved by means of the SPARSEKIT package, in particular using a Flexible version of Generalized Minimu RESidual method (FGMRES).

Once the new values for the temperature are obtained, they are substituded in the equation 2.24 and this goes on until one (or even both) of the following two conditions are reached

$$\left| log_{10} \frac{\frac{E_{int,i}^{n+1} - E_{int,i}^n}{\Delta t}}{CCC_i - \frac{L_{i+1/2}^{n+1} - L_{i-1/2}^{n+1}}{\Delta m_i}} \right| \leq \epsilon_1 \qquad (2.37)$$

$$\left| \frac{\Delta T_n}{T_n} \right| \leq \epsilon_2 \qquad (2.38)$$

where ϵ_1 and ϵ_2 are 10^{-8} and 10^{-7} respectively.

Few words must be spent on the boundary conditions: since the PPM scheme requires the interpolation of parabolas, we need some further points at the left or right side of the considered grid of the zones in which the stellar model is divided. At this purpose, we must implement some *ghost zones* which are non-physical portions of the star used only for computational reasons and can be used to set the boundary conditions for the problem. We set two different kind of boundary conditions whether we are considering the inner or the outer border of the grid: in the inner border we set reflecting boundary conditions while at the outer border we used zero gradient border condition. In the reflecting conditions we can image a wave hitting the border and being reflected back conserving energy and mass: this is achieved by giving, to the ghost zones, the same values for density and pressure but an opposite value for the velocity. In this way the resulting collision, produces no motion of the border but a lot of dense, hot and stationary matter is set: the expansion of this matter provides the reflection of the boundary condition. This is a possible choice for inner borders because, in a CCSN event, the dense Iron core which takes no part in the dynamical simulation. Another choice could be moving the inner boundary due to a certain law, but all these choices are arbitrary. In the outer boundaries, instead, we imagine that the flow of matter could leave the domain smoothly, and a similar behaviour can be achieved by giving zero gradient values for all the variables in the ghost zones.

2.2.2 Explosive Nucleosynthesis

One of the most important feature of the previous version of the hydro code is the calculation of the explosive nucleosynthesis occurring during a CCSN event. It is important in the first second of a CCSN event, when temperatures in the inner parts of the star are increased of several $10^9 K$ and there are a lot of nuclei ready to be forged to new one as the shock propagates through the star, changing the condition in temperature and density. In our code the explosive nucleosynthesis calculation is followed up to $T_{END} = 2.5 \cdot 10^4 s$ when the temperature are getting considerably lower respect to the initial values: to be precise explosive nucleosynthesis is well concluded within a second since the moment of the explosion, due to the sudden lowering of the temperature. We chose such a relative high temporal limit to have a reassuring margin to let the system evolve and allow all the expected nuclear decays to happen. In our nuclear network we consider 338 different isotopes (including protons, neutrons and α particles). The complete scheme and description of the nuclear reactions can be found in [43], as in this work the same setting has been used. The cross sections for all the nuclear reactions included in the network can be found in the same article [43]

As said in the previous paragraph, the evolution of the single chemical species is calculated by means of the equations 2.8. The solution of this set of equations gives us back the chemical composition of the star at each time step. The nuclear reactions considered give us the values for the cross sections σ allowing us to calculate the evolution. In this way we have information about the location and the quantity of some fundamental isotopes as ^{56}Ni which are obtained in a natural way.

2.2.3 Equation Of State and Saha Equation

In the first version of the code a perfect gas EOS was adopted. In the updated version of the code, on the contrary, we adopted the Timmes EOS as in [71]. Timmes EOS provides the values of pressure and internal energy along with their analytic derivatives respect to different variables as function of density, temperature and chemical composition in form of average atomic charge and average atomic weight of the zone. This EOS takes in account the radiation, the ions, the electrons and the positrons contributions and the Coulomb corrections, also for the energy is taken into account the ionization potential.

We take in account the effects due to the ionization of gas: at high temperatures the thermal collisions between atoms may cause the most external electron to gain enough energy to free itself from the attraction of the nucleus, becoming a free particle. Since free electrons scattering is the dominant radiative process in a CCSN environment, those particles may interact in a significant way with the radiation; therefore it is important to study the ionization state of atoms. The ionization is fundamental in studying the impact of the recombination wave (see Chapter 4), which is the responsible for the existence of the plateau features of the light curves of Type II-P CCSNe. In this calculation we use the approach proposed by [78], which allows us to find the fractions of atoms in each ionization state. The tools that allows the calculation of this feature are the Saha-Boltzmann equations 2.39 defined as:

$$\frac{n_{s+1}n_e}{n_s} = 2\frac{g_{s+1}}{g_s}\left[\frac{2\pi m_e k_B T}{h^2}\right] exp(-\frac{\chi_s}{k_B T})s = 1, 2...Z \tag{2.39}$$

where n_s and n_e are respectively the numerical density of the atoms in the s-th ionization state and the numerical density of the electrons, g_s is the statistical weight of the s-th state, m_e is the mass of the electron, while χ_s is the ionization energy required for the passage from the state s to the state $s + 1$ and Z is the atomic number of the element. These equations must be solved together with the equation for the electro-neutrality 2.40 and the one for the conservation of heavy nuclei 2.41 which build a system of equations.

$$\sum_{s=2}^{Z+1}(s + 1)n_s = n_e \tag{2.40}$$

$$\sum_{s=1}^{Z+1}n_s = n_k = cost \tag{2.41}$$

Where k is the index for the chosen element.

With the results of the Saha-Boltzmann equations 2.39 we can know the number of free electrons and use them to calculate the effects of the degree of ionization on the EOS. Since a similar system of equations is invoked for each chemical element, it is important to control the computational time required in each invocation: this is why we chose to consider only the Hydrogen and Helium as target for this calculation, leaving all the other chemical elements fully ionized (due to the number of electrons, the ionization of other elements is even more important than in the Hydrogen and Helium case, but the presence of metals results negligible in the envelope, where the contribute of ionization is considerable).

2.2.4 Opacity and photosphere tracking

Opacity covers a fundamental role in computing luminosity and, therefore, in the determination of the light curve. We adopted a Rosseland's mean opacity as in 2.7 starting the calculation from some tables where the values of the opacities are reported. The tables we used are provided by Alexander and Ferguson (2005) [22] for low temperatures range, and by Iglesias and Rogers (1996) (OPAL tables) [35] for high temperatures regimes. The OPAL tables [35] are given in two different structures one for the mixtures (where Hydrogen is negligible) and the other for pure elements (with the presence of Hydrogen): whether in the considered zone the total amount of Hydrogen is different from zero, we use the tables for pure elements and we proceed to calculate the opacities by computing a linear combination on all those elements. In the other case, in the regions where the quantity of Hydrogen is negligible, we use the tables for the mixtures of chemical elements and we get the values of the opacities by means of cubic interpolations both in temperature and in density. The problem with these tables is found at their borders: a single table can not cover the entire range of opacities for at all the temperature and density values reached during a CCSN event, and this is why more tables must be used together to have a full coverage of the opacities.

The photosphere position is fundamental in determining the quantity of energy per second emitted by the star or by nuclear decays. During a CCSN event the position of the photosphere recedes back as the ejecta are thrown away from the explosion, and encounters all the different chemical layers of the progenitor star, exposing, in this way, all the internal matter of the stellar structure. As pointer for the photosphere we considered the value of the optical depth τ (where $\tau = - \int_0^r k\rho dr$, r is the radius of the zone, k is the Rosseland's mean opacity and ρ is the density). In this way we define the photosphere as the geometrical place of the star where $\tau = \frac{2}{3}$, as in [49] (working in spherical symmetry we only consider the position of the photosphere as the zone where the optical depth reaches that value).

2.2.5 Deposition of energy from Nickel decay

In order to compute the contribution of the energy released in the nuclear decay of heavy elements we developed a code which is based on [67], and its duty is to calculate the ϵ_{Ni} term in 2.2. The general idea is to determine a sphere in the inner part of the stellar structure, where the quantity of ^{56}Ni (formed during the explosive nucleosynthesis) is not negligible (we set a threshold in the code) and, starting from this sphere, we calculate the solutions, in grey body approximation, of the energy

transfer equation for all the γ-rays which start their travel from this sphere. During their travel from this sphere towards the ejecta, the γ-rays may be absorbed by the matter, heating it and rising its temperature. A figure 2.2 could help to give an idea of the procedure adopted.

Figure 2.2: The scheme used in our approximation. The central circle is the zone where the presence of ^{56}Ni is not negligible. For each zone of the star the angle θ states the position of the single γ-ray and its path from the border of the sphere to the chosen zone of the star. This figure is a adaptation of a similar figure found in the manual of SNEC, an hydro code presented by Morozova and Piro (2015) [49]

As degrees of freedom it is possible to select the opacity of the γ-rays, and the angular separation between the different rays used in the calculation. To be clear, without this calculation it is still possible, in our scheme, to calculate the amount of energy coming from nuclear processes and its quantity leaving or arriving into a particular zone of the star. Such a calculation is fundamental because it allows to compute the energy contribution for all those zones which are positioned beyond the photosphere, where the approximation of diffusion could be not be respected due to

a huge increase of the mean free path of photons. The quantity of energy deposited in each zone of the star is calculated as $\epsilon_{rad}d$ where ϵ_{rad} is the time dependent rate of energy release per gram of ^{56}Ni defined as

$$\epsilon_{rad} = 3.9 \cdot 10^{10} exp(-t/\tau_{Ni}) + 6.78 \cdot 10^{9}[exp(-t/\tau_{Co}) - exp(-t/\tau_{Ni})] \frac{erg}{gs} \quad (2.42)$$

where τ_{Ni} and τ_{Co} are the lifetime of ^{56}Ni and ^{56}Co respectively (8.8 and 113.6 days), and the deposition function d is given by

$$d = \frac{1}{4\pi} \oint I'd\omega \quad (2.43)$$

where ω is the solid angle and I' is $I' = (4\pi k_\gamma/\epsilon_{rad})I$, $k_\gamma = 0.06Y_e cm^2 g^{-1}$ is the opacity of the gamma ray which is assumed only dependent from the electron fraction. I is the energy-integrated intensity obtained by solving the equation 2.44

$$\frac{\delta I}{\delta z} = \eta - k_\gamma \rho I \quad (2.44)$$

where z is the path of the ray, ρ is the density of matter, $\eta = X_{Ni}\epsilon_{rad}\rho/4\pi$ is the local γ ray emissivity and X_{Ni} is the mass fraction of ^{56}Ni. Using τ which is the optical depth along the ray described as

$$d\tau = -k_y \rho dz \quad (2.45)$$

and working on equation 2.44 we can reach

$$I'(\tau_{j+1}) = I'(\tau_j)e^{-(-\tau_j - \tau_{j+1})} + X_{Ni,j}\left[1 - e^{-(t - \tau_{j+1})}\right] \quad (2.46)$$

and using these formulas we can fully calculate, at each stellar zone, the quantity $\epsilon_{rad}d$ required in equation 2.2.

We end the description of the numerical code by placing two *caveat* on this treatment. The first one is that this approach could not be applied to a whole LC: this because, at late times, the ejecta becomes optically thin and the major contribution to the luminosity is due to the decay of ^{56}Ni. It is possible to set a sort of arbitrary threshold in which, once surpassed, the black body can not be trusted anymore: we chose this threshold at the moment when the luminosity contribution due to ^{56}Ni above the photosphere amounts to more than the 5% of the total luminosity as in [49]. The second remark, well known in literature, is about the fact that the one-temperature codes can not reproduce in the right way the observed B- and U-band

of real SN due to, after some days, the line blanketing of the iron group on these bands.

2.3   The grid of models

One of the most interesting feature of this work is the opportunity to test the code just described on a set of PSN models covering a huge variety of different combinations of stellar features available in the Universe. This set is taken from the work by Limongi and Chieffi [45] and they all come from evolutionary processes starting from the pre-Main Sequence phase to the presupernova stage which is the moment when the typical equations of stellar equilibrium do not converge anymore. The evolution if followed by the FRANEC code [43]. The models cover a wide range of different initial masses: 13, 15, 20, 25, 30, 40, 60 $M_\odot$. All the different stars have been evolved with four different initial metallicities: [Fe/H]=0,-1,-2,-3. Each combination of initial mass and metallicity have been considered having an initial rotation velocity of 0 km/s. Only for metallicity [Fe/H]=-3 we also calculated the entire set for 80 $M_\odot$. Combining these two features we obtained 29 different evolutionary models. Each one of these 29 models exploded with seven different quantity of energies: these energies are 0.01, 0.05, 0.10, 0.50, 1.00, 1.50 and 2.00 foe. In this way over 203 explosion simulations have been done and each simulation have been followed up to 350 days, this to examine the late effects on the light curves. Only concerning the light curves (Chapter 4), we excluded from the analysis the models not exploding as Super Giant stars with huge hydrogen-rich envelopes resulting as II-P CCSNe. We did not investigate in a systematic way the effects of rotating stellar models in the explosions for time reasons, but some considerations about rotation can be found in the conclusions.

Chapter 3

The results of the simulations

3.1 The results

In this Chapter we will now show all the results of the simulations, focusing on the remnant masses and some other linked features, leaving, for Chapter 4, the light curves.

To organize the work, we used a particular nomenclature to recognize the metallicity associated to the respective model: a means [Fe/H]=0, b [Fe/H]=-1, c [Fe/H]=-2, d [Fe/H]=-3, so i.e. a model with 20 $M_\odot$ and a metallicity of [Fe/H]=-2 will be labeled as 20c. Below we report two tables 3.1 and 3.2: the first is filled with the summary of the most important physical quantities of the models used in this work at the presupernova stage, while the second contains information about the chemistry of the star. In table 3.1, starting from left to right, the columns stand for: the label of the model, the initial mass, the effective temperature, the luminosity, the total mass, the binding energy of the matter outside the Iron core, the mass of the Hydrogen envelope (defined as the difference between the total mass and the mass coordinate in which the Hydrogen mass fraction drops below 10^{-4}) in units of $10M_\odot$, the total radius in units of $500R_\odot$. The second table 3.2 shows, in the order, the label of the model, the initial mass, the total mass, the mass of the Helium core, the mass of the Carbon-Oxygen core, the mass of the Iron core, the total mass of Hydrogen in the envelope, the total mass of Helium in the envelope.

We present four tables (3.3,3.4,3.5,3.6), one for each different metallicity, which summarize the most important outcomes obtained from our simulations. Before describing the different components of this table we must define the net energy of

Table 3.1: Physical properties of the presupernova models

Model Id.	Initial Mass (M$_\odot$)	Log(T_{eff}) (K)	Log($L/L_\odot$)	M (M$_\odot$)	E_{bind} ($10^{51}erg$)	M_{10} ($10M_\odot$)	R_{500} ($500R_\odot$)
13a	13	3.55	4.82	11.9	0.65	0.78	1.32
15a	15	3.54	4.98	13.3	0.95	0.83	1.68
20a	20	4.01	5.23	7.54	2.00	0.03	0.25
25a	25	5.09	5.38	8.54	2.24	0.85	$2 \cdot 10^{-3}$
30a	30	5.16	5.55	10.8	4.75	1.08	$2 \cdot 10^{-3}$
40a	40	5.27	5.70	14.1	6.17	1.41	$1 \cdot 10^{-3}$
60a	60	5.35	5.85	17.0	9.28	1.70	$1 \cdot 10^{-3}$
13b	13	3.60	4.85	12.5	1.08	0.83	1.13
15b	15	3.59	5.05	14.2	1.33	0.90	1.48
20b	20	3.59	5.26	18.4	1.79	1.09	1.86
25b	25	3.58	5.48	20.6	4.02	1.05	2.52
30b	30	3.75	5.48	28.3	4.45	1.65	1.16
40b	40	3.65	5.63	28.7	6.59	1.22	2.17
60b	60	3.65	5.89	42.0	18.0	1.57	2.95
13c	13	3.65	4.88	13.0	0.85	0.60	1.37
15c	15	3.64	5.01	14.8	1.70	0.96	1.09
20c	20	3.64	5.27	19.7	1.83	1.23	1.48
25c	25	3.67	5.20	24.7	2.54	1.49	1.22
30c	30	4.27	5.52	29.9	3.96	1.84	0.11
40c	40	4.22	5.75	39.7	7.39	2.32	0.17
60c	60	4.10	6.06	59.6	19.2	3.25	0.41
13d	13	3.66	4.88	13.0	1.30	0.88	0.86
15d	15	3.66	5.06	15.0	1.45	0.98	1.08
20d	20	3.66	5.26	19.8	1.86	1.25	1.36
25d	25	3.66	5.46	24.6	2.89	1.50	1.71
30d	30	4.07	5.51	30.0	4.16	1.78	0.26
40d	40	4.34	5.75	40.0	8.61	2.28	0.10
60d	60	4.29	6.04	59.9	22.0	3.18	0.25
80d	80	4.25	6.22	79.9	36.4	4.17	0.25

Table 3.2: Masses of some zones of the star

Model Id.	Initial Mass	M	M_{He}	M_{CO}	M_{Fe}	H	He
	(M$_\odot$)	(M$_\odot$)	(M$_\odot$)	(M$_\odot$)	(M$_\odot$)	(M$_\odot$)	(M$_\odot$)
13a	13	11.9	4.08	2.03	1.36	5.37	4.31
15a	15	13.3	4.95	2.78	1.43	5.67	4.63
20a	20	7.54	7.29	3.86	1.10	0.06	3.39
25a	25	8.54	0.00	6.21	1.38	0.00	2.26
30a	30	10.8	0.00	7.91	1.57	0.00	2.74
40a	40	14.1	0.00	10.6	1.53	0.00	2.49
60a	60	17.0	0.00	13.0	1.52	0.00	0.93
13b	13	12.5	4.26	2.13	1.19	5.83	4.44
15b	15	14.2	5.22	3.01	1.40	6.34	4.54
20b	20	18.4	7.52	4.21	1.43	7.47	6.50
25b	25	20.6	10.2	6.82	1.59	6.96	6.62
30b	30	28.3	11.9	7.22	1.57	10.2	10.5
40b	40	28.7	16.7	10.9	1.55	6.00	11.3
60b	60	42.0	26.8	19.6	1.68	0.06	14.8
13c	13	13.0	4.34	2.14	1.40	6.23	4.44
15c	15	14.8	5.21	2.72	1.08	6.86	5.09
20c	20	19.7	7.49	4.23	1.43	8.60	6.71
25c	25	24.7	9.87	5.93	1.53	10.2	8.26
30c	30	29.9	17.7	6.98	1.55	11.6	10.8
40c	40	39.7	16.7	11.2	1.54	14.4	13.8
60c	60	59.6	27.2	20.0	1.69	18.6	20.5
13d	13	13.0	4.22	2.15	1.15	6.22	4.44
15d	15	15.0	5.22	3.09	1.46	6.95	4.62
20d	20	19.8	7.42	4.35	1.44	8.64	6.63
25d	25	24.6	9.84	6.29	1.53	10.1	8.00
30d	30	30.0	12.3	8.08	1.57	11.9	9.70
40d	40	40.0	17.5	12.2	1.72	14.6	12.8
60d	60	59.9	28.5	21.7	1.75	19.8	17.9
80d	80	79.9	38.9	29.6	1.81	24.2	25.2

the explosion E_{net} as $E_{net} = E_{expl} - |E_{grav} + E_{int}|$ in which E_{expl} is the total energy of the explosion and E_{grav} is the gravitational energy defined as a negative quantity. The values appearing in the tables (3.3,3.4,3.5,3.6) are (starting from the column in the left to the one in the right): model label, E_{net}, the time of the shock breakout, the time at the end of the fallback, the quantity of ^{56}Ni ejected, the final mass of the remnant, the mass of the ejecta, the final kinetic energy of the ejecta and the bolometric luminosity of the light curve 50 days after the onset of the explosion.

Table 3.3: Main results for set a ([Fe/H]=0, v=0)

Model Id.	E_{net} (10^{51} erg)	$t_{breakout}$ (s)	$t_{fallback}$ (s)	$^{56}Ni_{ejected}$ ($M_\odot$)	M_{rem} ($M_\odot$)	M_{ejecta} ($M_\odot$)	$E_{kin_{ejecta}}$ (erg)	$Log(L_{50})$ (ergs^{-1})
13a	0.01	2.35E+05	1.86E+07	9.78E-40	2.10	9.76	2.03E+50	41.66
13a	0.05	2.25E+05	1.01E+07	9.80E-40	2.07	9.80	2.25E+50	41.70
13a	0.10	2.11E+05	5.51E+06	9.84E-40	2.03	9.83	2.56E+50	41.75
13a	0.50	1.49E+05	9.24E+05	7.48E-05	1.60	10.26	5.25E+50	42.02
13a	1.00	1.12E+05	1.21E+02	1.46E-01	1.36	11.00	1.02E+51	42.24
13a	1.50	9.16E+04	7.79E+01	1.62E-01	1.36	11.02	1.51E+51	42.36
13a	2.00	8.02E+04	0.00E+00	1.72E-01	1.36	11.05	2.01E+51	42.46
15a	0.01	2.92E+05	8.67E+06	1.03E-39	2.93	10.31	2.20E+50	41.78
15a	0.05	2.78E+05	4.31E+05	1.04E-39	2.86	10.37	2.46E+50	41.83
15a	0.10	2.61E+05	6.42E+06	1.05E-39	2.80	10.44	2.79E+50	41.88
15a	0.50	1.87E+05	8.90E+06	6.33E-17	2.15	11.09	5.72E+50	42.14
15a	1.00	1.45E+05	1.07E+04	1.26E-01	1.43	11.82	1.01E+51	42.34
15a	1.50	1.21E+05	2.22E+02	1.51E-01	1.43	12.35	1.50E+51	42.47
15a	2.00	1.06E+05	1.51E+02	1.74E-01	1.43	12.38	2.00E+51	42.55
20a	0.01	4.74E+03	1.22E+05	2.81E-40	4.75	2.29	X	X
20a	0.05	5.88E+03	4.25E+05	2.93E-40	4.66	2.88	X	X
20a	0.10	4.64E+03	2.21E+05	3.08E-40	4.50	3.04	2.60E+50	X
20a	0.50	1.40E+04	1.05E+06	3.92E-40	3.67	3.88	5.82E+50	X
20a	1.00	2.58E+03	1.81E+06	5.97E-17	2.23	5.31	1.03E+51	X
20a	1.50	2.66E+03	3.61E+05	9.97E-04	1.66	5.88	1.51E+51	38.88
20a	2.00	2.37E+03	9.84E+04	3.92E-01	1.10	6.61	2.04E+51	42.42
25a	0.01	1.30E+02	1.22E+05	1.96E-40	6.61	1.93	X	X
25a	0.05	1.29E+02	7.22E+04	2.07E-40	6.50	2.05	X	X
25a	0.10	1.23E+02	6.52E+04	2.18E-40	6.38	2.16	2.90E+50	X
25a	0.50	1.04E+02	1.61E+05	4.49E-18	5.04	3.50	5.76E+50	34.55
25a	1.00	8.74E+01	2.18E+05	2.11E-17	3.13	5.41	1.03E+51	X
25a	1.50	7.67E+01	1.48E+05	2.81E-17	2.39	6.15	1.53E+51	X

25a	2.00	6.85E+01	1.26E+05	8.36E-13	2.12	6.24	2.02E+51	X
30a	0.01	9.38E+01	3.36E+05	2.30E-40	8.56	2.27	X	X
30a	0.05	9.34E+01	7.00E+04	2.38E-40	8.47	2.36	X	X
30a	0.10	9.02E+01	7.81E+04	2.47E-40	8.39	2.45	X	X
30a	0.50	8.06E+01	6.09E+04	3.03E-40	7.83	3.00	7.58E+50	X
30a	1.00	7.13E+01	1.93E+05	9.51E-19	6.58	4.25	1.13E+51	38.27
30a	1.50	6.50E+01	2.08E+05	6.91E-18	4.99	5.84	1.57E+51	X
30a	2.00	6.10E+01	9.64E+05	1.89E-17	3.93	6.90	2.04E+51	X
40a	0.01	6.89E+01	5.20E+04	2.17E-40	11.98	2.17	X	X
40a	0.05	6.89E+01	9.15E+04	2.27E-40	11.92	2.22	X	X
40a	0.10	6.70E+01	9.08E+04	2.33E-40	11.81	2.33	X	X
40a	0.50	6.15E+01	9.53E+04	3.09E-40	11.12	3.01	X	X
40a	1.00	5.59E+01	1.25E+05	2.36E-39	10.35	3.79	1.09E+51	X
40a	1.50	5.16E+01	1.08E+05	1.02E-18	8.87	5.27	1.48E+51	37.90
40a	2.00	4.79E+01	2.61E+05	3.73E-18	7.39	6.78	1.92E+51	X
60a	0.01	4.78E+01	9.73E+04	2.23E-40	14.73	2.23	5.61E+50	X
60a	0.05	4.74E+01	8.05E+04	2.30E-40	14.66	2.30	5.83E+50	X
60a	0.10	4.71E+01	8.87E+04	2.37E-40	14.59	2.37	6.12E+50	X
60a	0.50	4.44E+01	1.49E+05	3.04E-40	14.00	2.95	8.54E+50	X
60a	1.00	4.07E+01	1.05E+05	3.70E-40	13.27	3.69	1.19E+51	X
60a	1.50	3.84E+01	1.11E+07	4.72E-40	12.65	4.31	1.54E+51	X
60a	2.00	3.62E+01	8.30E+04	9.32E-37	11.61	5.35	1.92E+51	38.45

Table 3.4: Main results for set b ([Fe/H]=-1, v=0)

Model Id.	E_{net} $(10^{51}$ erg$)$	$t_{breakout}$ (s)	$t_{fallback}$ (s)	$^{56}Ni_{ejected}$ $(M_\odot)$	M_{rem} $(M_\odot)$	M_{ejecta} $(M_\odot)$	$E_{kin_{ejecta}}$ (erg)	$Log(L_{50})$ $(ergs^{-1})$
13b	0.01	2.11E+05	1.78E+06	1.02E-39	2.27	10.22	1.92E+50	41.59
13b	0.05	2.00E+05	9.99E+05	1.03E-39	2.22	10.26	2.15E+50	41.63
13b	0.10	1.87E+05	9.04E+05	1.03E-39	2.18	10.31	2.45E+50	41.68
13b	0.50	1.31E+05	1.21E+06	3.91E-13	1.76	10.73	5.17E+50	41.96
13b	1.00	9.79E+04	3.17E+02	3.34E-01	1.19	11.63	1.03E+51	42.19
13b	1.50	8.04E+04	5.93E+01	3.53E-01	1.19	11.66	1.53E+51	42.32
13b	2.00	6.98E+04	0.00E+00	3.64E-01	1.19	11.68	2.03E+51	42.42
15b	0.01	2.63E+05	1.27E+07	1.08E-39	3.40	10.78	2.24E+50	41.75
15b	0.05	2.50E+05	8.63E+06	1.09E-39	3.33	10.85	2.49E+50	41.79
15b	0.10	2.33E+05	7.81E+06	1.09E-39	3.25	10.93	2.87E+50	41.84

15b	0.50	1.68E+05	1.93E+05	1.36E-23	2.47	11.71	5.79E+50	42.11
15b	1.00	1.31E+05	2.80E+04	2.59E-02	1.60	12.58	1.02E+51	42.31
15b	1.50	1.10E+05	8.74E+03	2.00E-01	1.40	12.86	1.51E+51	42.43
15b	2.00	9.71E+04	5.30E+02	2.32E-01	1.40	13.29	2.00E+51	42.52
20b	0.01	3.62E+05	1.18E+05	1.34E-39	4.97	13.39	2.34E+50	41.80
20b	0.05	3.46E+05	4.17E+05	1.35E-39	4.87	13.48	2.59E+50	41.84
20b	0.10	3.27E+05	1.28E+05	1.36E-39	4.75	13.60	2.91E+50	41.90
20b	0.50	2.36E+05	3.73E+05	1.44E-39	3.98	14.38	5.98E+50	42.16
20b	1.00	1.83E+05	2.13E+05	2.67E-17	2.53	15.83	1.04E+51	42.35
20b	1.50	1.54E+05	2.21E+05	5.69E-09	1.95	16.41	1.50E+51	42.48
20b	2.00	1.37E+05	3.83E+04	1.68E-01	1.57	16.79	2.00E+51	42.57
25b	0.10	3.59E+05	1.99E+05	1.31E-39	7.54	13.04	4.26E+50	42.18
25b	0.50	2.87E+05	6.11E+04	1.37E-39	6.86	13.72	7.04E+50	42.37
25b	1.00	2.36E+05	1.60E+06	4.32E-19	5.67	14.91	1.09E+51	42.52
25b	1.50	2.05E+05	1.36E+05	2.99E-18	4.04	16.54	1.52E+51	42.62
25b	2.00	1.85E+05	9.57E+06	5.71E-12	3.24	17.34	1.99E+51	42.71
30b	0.01	1.33E+05	1.18E+07	1.90E-39	11.78	16.50	3.74E+50	41.01
30b	0.05	1.26E+05	9.19E+06	1.93E-39	11.45	16.82	4.00E+50	41.11
30b	0.10	1.21E+05	8.31E+06	1.95E-39	10.84	17.44	4.33E+50	41.13
30b	0.50	9.77E+04	9.33E+06	2.06E-39	7.85	20.42	7.27E+50	41.27
30b	1.00	7.95E+04	1.41E+05	2.14E-39	6.91	21.37	1.13E+51	41.36
30b	1.50	6.93E+04	3.02E+05	1.00E-18	5.38	22.90	1.56E+51	41.42
30b	2.00	6.14E+04	4.05E+05	2.97E-18	1.57	24.32	2.02E+51	41.47
40b	0.01	2.76E+05	1.08E+05	1.51E-39	13.66	15.05	X	X
40b	0.05	2.68E+05	8.60E+04	1.52E-39	13.55	15.17	4.40E+50	41.67
40b	0.10	2.61E+05	3.51E+05	1.54E-39	13.43	15.28	4.71E+50	41.65
40b	0.50	2.16E+05	1.62E+05	1.64E-39	12.43	16.29	7.38E+50	41.64
40b	1.00	1.80E+05	1.17E+05	1.74E-39	11.42	17.29	1.11E+51	41.66
40b	1.50	1.58E+05	1.40E+05	1.81E-39	10.67	18.04	1.50E+51	41.69
40b	2.00	1.43E+05	6.54E+04	1.96E-01	9.29	19.42	1.91E+51	41.79
60b	0.01	3.15E+05	3.15E+05	1.89E-39	23.12	18.84	9.06E+50	42.40
60b	0.05	3.14E+05	2.22E+05	1.90E-39	23.05	18.91	9.28E+50	42.41
60b	0.10	3.11E+05	3.11E+05	1.90E-39	22.98	18.98	9.56E+50	42.41
60b	0.50	2.86E+05	2.24E+04	1.94E-39	22.61	19.35	X	X
60b	1.00	2.58E+05	2.98E+04	2.01E-39	21.94	20.02	X	X
60b	1.50	2.37E+05	4.20E+05	2.08E-09	21.26	20.70	X	X
60b	2.00	2.19E+05	2.85E+04	2.32E-01	20.45	21.52	X	X

Table 3.5: Main results for set c ([Fe/H]=-2, v=0)

Model Id.	E_{net} $(10^{51}$ erg$)$	$t_{breakout}$ (s)	$t_{fallback}$ (s)	$^{56}Ni_{ejected}$ $(M_\odot)$	M_{rem} $(M_\odot)$	M_{ejecta} $(M_\odot)$	$E_{kin_{ejecta}}$ (erg)	$\text{Log}(L_{50})$ $(erg\,s^{-1})$
13c	0.01	1.69E+05	1.03E+05	7.68E-40	3.84	7.67	3.32E+50	41.97
13c	0.05	1.63E+05	2.43E+05	7.73E-40	3.79	7.72	3.57E+50	41.99
13c	0.10	1.57E+05	1.47E+05	7.80E-40	3.73	7.78	3.89E+50	42.02
13c	0.50	1.23E+05	6.32E+05	3.96E-25	3.12	8.39	6.70E+50	42.18
13c	1.00	9.98E+04	4.30E+04	2.58E-04	2.15	9.37	1.08E+51	42.29
13c	1.50	8.58E+04	1.01E+04	1.05E-01	1.92	9.59	1.54E+51	42.37
13c	2.00	7.64E+04	5.54E+04	3.05E-01	1.51	10.00	2.01E+51	42.51
15c	0.01	2.12E+05	2.44E+05	1.17E-39	3.11	11.68	2.04E+50	41.58
15c	0.05	1.99E+05	3.18E+05	1.18E-39	3.02	11.76	2.30E+50	41.62
15c	0.10	1.87E+05	5.88E+05	1.19E-39	2.93	11.86	2.66E+50	41.68
15c	0.50	1.32E+05	5.38E+05	9.05E-25	2.50	12.29	5.61E+50	41.96
15c	1.00	1.01E+05	2.71E+07	4.09E-01	1.08	13.75	1.04E+51	42.15
15c	1.50	8.47E+04	1.60E+02	4.42E-01	1.08	13.92	1.54E+51	42.29
15c	2.00	7.37E+04	2.39E+01	4.69E-01	1.08	13.95	2.04E+51	42.38
20c	0.01	3.01E+05	9.11E+06	1.47E-39	5.03	14.69	2.36E+50	41.70
20c	0.05	2.87E+05	9.64E+04	1.48E-39	4.91	14.81	2.61E+50	41.74
20c	0.50	1.96E+05	1.12E+05	1.57E-39	4.02	15.71	6.01E+50	42.05
20c	1.00	1.53E+05	5.12E+05	3.67E-16	2.58	17.14	1.04E+51	42.25
20c	1.50	1.28E+05	3.00E+05	1.14E-11	1.99	17.74	1.51E+51	42.38
20c	2.00	1.13E+05	2.67E+04	1.76E-01	1.58	18.14	2.00E+51	42.47
25c	0.01	2.48E+05	2.23E+05	1.74E-39	7.37	17.28	2.47E+50	41.59
25c	0.05	2.35E+05	2.15E+05	1.75E-39	7.22	17.44	2.73E+50	41.63
25c	0.10	2.21E+05	5.30E+05	1.77E-39	7.03	17.62	3.07E+50	41.67
25c	0.50	1.64E+05	9.43E+04	1.88E-39	5.93	18.72	6.13E+50	41.89
25c	1.00	1.29E+05	9.02E+04	1.73E-16	4.17	20.48	1.04E+51	42.05
25c	1.50	1.09E+05	3.97E+05	3.96E-16	2.86	21.80	1.52E+51	42.14
25c	2.00	9.60E+04	1.96E+05	1.68E-11	2.38	22.28	2.01E+51	42.21
30c	0.01	1.66E+04	1.27E+05	1.76E-39	12.34	17.52	3.19E+50	40.63
30c	0.05	1.34E+04	1.34E+05	1.80E-39	11.84	18.02	3.47E+50	40.66
30c	0.10	4.10E+04	4.10E+04	1.80E-39	11.87	17.99	3.82E+50	40.69
30c	0.50	1.02E+04	5.23E+06	2.06E-39	11.38	18.48	6.85E+50	40.85
30c	1.00	9.30E+03	5.86E+06	2.30E-39	7.89	21.97	1.10E+51	40.98

Model Id.	E_{net} (10^{51} erg)	$t_{breakout}$ (s)	$t_{fallback}$ (s)	$^{56}Ni_{ejected}$ ($M_\odot$)	M_{rem} ($M_\odot$)	M_{ejecta} ($M_\odot$)	E_{kin_ejecta} (erg)	Log(L_{50}) (erg s^{-1})
30c	1.50	8.23E+03	2.20E+07	3.18E-16	4.67	25.20	1.55E+51	41.60
30c	2.00	7.15E+03	6.85E+05	5.94E-16	3.45	26.42	2.03E+51	41.12
40c	0.01	2.35E+04	8.13E+06	2.21E-39	18.98	20.77	4.51E+50	40.86
40c	0.05	2.10E+04	1.96E+07	2.22E-39	18.80	20.95	4.76E+50	40.88
40c	0.10	1.95E+04	1.04E+07	2.24E-39	18.61	21.14	5.07E+50	40.90
40c	0.50	1.68E+04	5.81E+06	2.34E-39	17.29	22.46	7.79E+50	41.02
40c	1.00	1.49E+04	6.63E+06	2.64E-39	15.99	23.76	X	41.14
40c	1.50	1.38E+04	2.02E+07	2.83E-39	13.10	26.65	1.54E+51	41.22
40c	2.00	1.65E+04	2.71E+06	3.27E-39	10.57	29.18	1.95E+51	41.29
60c	0.05	3.64E+04	3.51E+06	3.15E-39	29.68	29.93	X	41.24
60c	0.10	4.57E+04	7.25E+06	3.14E-39	29.68	29.93	9.95E+50	41.25
60c	0.50	3.98E+04	1.83E+07	3.16E-39	28.98	30.63	1.20E+51	41.30
60c	1.00	3.11E+04	7.50E+06	3.24E-39	28.00	31.62	1.53E+51	41.38
60c	1.50	3.94E+04	4.77E+06	3.38E-39	27.50	32.12	1.88E+51	41.26
60c	2.00	2.56E+04	9.53E+06	3.59E-39	26.86	32.76	2.22E+51	41.46

Table 3.6: Main results for set d ([Fe/H]=-3, v=0)

Model Id.	E_{net} (10^{51} erg)	$t_{breakout}$ (s)	$t_{fallback}$ (s)	$^{56}Ni_{ejected}$ ($M_\odot$)	M_{rem} ($M_\odot$)	M_{ejecta} ($M_\odot$)	E_{kin_ejecta} (erg)	Log(L_{50}) (erg s^{-1})
13d	0.01	1.60E+05	5.56E+05	1.06E-39	2.42	10.55	1.98E+50	41.49
13d	0.05	1.52E+05	5.97E+05	1.06E-39	2.37	10.61	2.21E+50	41.54
13d	0.10	1.42E+05	9.73E+06	1.07E-39	2.32	10.66	2.53E+50	41.59
13d	0.50	9.99E+04	2.10E+06	5.64E-14	1.90	11.07	5.29E+50	41.86
13d	1.00	7.64E+04	1.63E+02	3.77E-01	1.15	12.12	1.04E+51	42.08
13d	1.50	6.28E+04	4.07E+01	4.04E-01	1.15	12.15	1.54E+51	42.22
13d	2.00	5.44E+04	0.00E+00	4.12E-01	1.15	12.16	2.05E+51	42.33
15d	0.05	1.83E+05	1.14E+07	1.15E-39	3.44	11.51	2.66E+50	41.68
15d	0.10	1.73E+05	5.93E+06	1.16E-39	3.36	11.59	3.02E+50	41.73
15d	0.50	1.25E+05	1.07E+05	6.52E-17	2.70	12.25	5.95E+50	41.99
15d	1.00	9.81E+04	3.10E+04	2.61E-02	1.70	13.25	1.03E+51	42.19
15d	1.50	8.31E+04	1.32E+04	2.41E-01	1.46	13.67	1.51E+51	42.30
15d	2.00	7.31E+04	9.60E+02	2.73E-01	1.46	14.08	2.02E+51	42.40
20d	0.50	1.80E+05	2.25E+05	1.58E-39	4.03	15.76	6.03E+50	42.02
20d	1.00	1.40E+05	2.61E+05	2.36E-16	2.57	17.22	1.04E+51	42.21

20d	1.50	1.19E+05	2.36E+07	9.96E-10	2.04	17.75	1.51E+51	42.34
20d	2.00	1.04E+05	2.89E+04	2.14E-01	1.56	18.23	2.01E+51	42.43
25d	0.50	2.40E+05	5.44E+04	1.84E-39	6.30	18.33	6.29E+50	42.09
25d	1.00	1.90E+05	1.83E+07	1.90E-16	4.65	19.98	1.05E+51	42.27
25d	1.50	1.62E+05	7.22E+04	5.16E-16	3.13	21.50	1.52E+51	42.40
25d	2.00	1.44E+05	2.19E+05	6.72E-12	2.55	22.08	2.00E+51	42.50
30d	0.01	4.67E+04	1.39E+07	1.88E-39	13.21	16.77	3.24E+50	40.88
30d	0.05	3.50E+04	2.03E+07	1.94E-39	13.14	16.84	3.50E+50	40.90
30d	0.10	4.40E+04	1.96E+07	1.99E-39	13.00	16.98	3.82E+50	40.93
30d	0.50	2.57E+04	6.28E+06	2.14E-39	9.31	20.67	6.71E+50	41.12
30d	1.00	2.07E+04	8.32E+05	2.24E-39	7.72	22.26	1.07E+51	41.26
30d	1.50	2.04E+04	1.07E+05	2.52E-16	5.71	24.27	1.51E+51	41.36
30d	2.00	1.61E+04	1.52E+07	5.94E-16	4.14	25.84	1.99E+51	41.44
40d	0.01	1.18E+04	3.08E+06	2.11E-39	20.31	19.65	X	40.80
40d	0.50	1.18E+04	2.49E+04	2.24E-39	17.54	22.43	8.55E+50	40.93
40d	1.00	9.79E+03	9.04E+06	2.39E-39	17.64	22.33	1.21E+51	41.03
40d	1.50	7.37E+03	1.59E+07	2.61E-39	16.09	23.87	1.59E+51	41.11
40d	2.00	6.94E+03	7.63E+06	2.81E-39	13.41	26.55	1.98E+51	41.16
60d	0.05	1.73E+04	1.64E+07	3.02E-39	31.02	28.92	1.09E+51	41.17
60d	0.50	1.66E+04	1.66E+06	3.08E-39	29.16	30.79	1.35E+51	41.23
60d	1.00	1.52E+04	9.12E+06	3.10E-39	29.63	30.31	1.66E+51	41.28
60d	1.50	1.92E+04	3.27E+06	3.18E-39	29.39	30.55	X	41.33
60d	2.00	1.57E+04	5.22E+06	3.38E-39	28.87	31.07	2.32E+51	41.37
80d	0.01	2.15E+04	9.46E+06	3.92E-39	43.33	36.57	X	41.35
80d	0.05	2.11E+04	1.74E+07	3.89E-39	43.61	36.29	1.55E+51	41.36
80d	0.10	2.09E+04	8.88E+06	3.88E-39	43.68	36.23	X	41.36
80d	0.50	2.04E+04	6.53E+06	3.92E-39	42.85	37.05	1.80E+51	41.40
80d	1.00	1.87E+04	2.71E+07	3.96E-39	42.13	37.77	2.08E+51	41.45
80d	1.50	1.82E+04	5.83E+06	4.01E-39	41.34	38.57	2.40E+51	41.49
80d	2.00	1.73E+04	6.77E+06	4.07E-39	40.51	39.39	X	41.54

We used the same settings for all the simulations: if a quantity resulted not available as outcome, we labeled it in the tables 3.3,3.4,3.5,3.6 with an X.

3.2   The analysis of the results

The value of metallicity has a fundamental role in determining the physical features of the stellar progenitors: a low presence of metals in stars makes the structures more compact and hotter with respect to other metal-rich stars. Metallicity, indeed, is strictly bond to opacity and a low presence of metals limits the interactions between radiation and matter: with low opacity the radiation can get through the stellar structure easily. A consequence of the high presence of metals in stars is the removal of a huge part of the most external layers (mostly Hydrogen-rich) from the stellar structure: the mass-loss rate is increased because the star shows a faint envelope. Once the role of metallicity in stars in cleared we can proceed with the presentation of the results.

The time taken from the shock wave to breakout from the photosphere grows with the mass of the progenitor and decreases with the increasing of the explosion energy: this comes naturally because massive stars tend to be more extended and the shock wave will need a larger time to run across all the structure. Furthermore, more energetic shock waves gets higher velocities: in this way the shock waves will take less time to reach the surface of the star. This amount of time also decreases with the decreasing metallicity: this because the star results more compact and less expanded. The behaviour explained is shown in figures 3.1 and 3.2.

The time required for the fallback, as mentioned in Chapter 1, is one of the most debated feature in a CCSN event and it strongly depends on the energy of the explosion and on the binding energy of the star. More specifically very energetic explosion tend to decrease the time of the fallback (or even completely avoid the fallback, in these cases the time of the fallback has been reported as zero in our tables). Furthermore we found that massive progenitors tend to have a fallback extended in time compared to the less massive counterparts. The metallicity has an influence on this parameter: as the metallicity decreases, the typical timescales of the fallback increases, this because the progenitor star results more compact and more energy will be used to win the binding energy.

Similar results can be found in the analysis of the amount of ^{56}Ni ejected in the explosion: since ^{56}Ni is mostly forged just outside the edge of the Iron core, this quantity is strictly related to the amount of matter involved in the fallback. In general, an high energetic explosion allows the ^{56}Ni to be spread in the ejecta. The opposite result is found as the mass stellar progenitor grows. The amount of ^{56}Ni
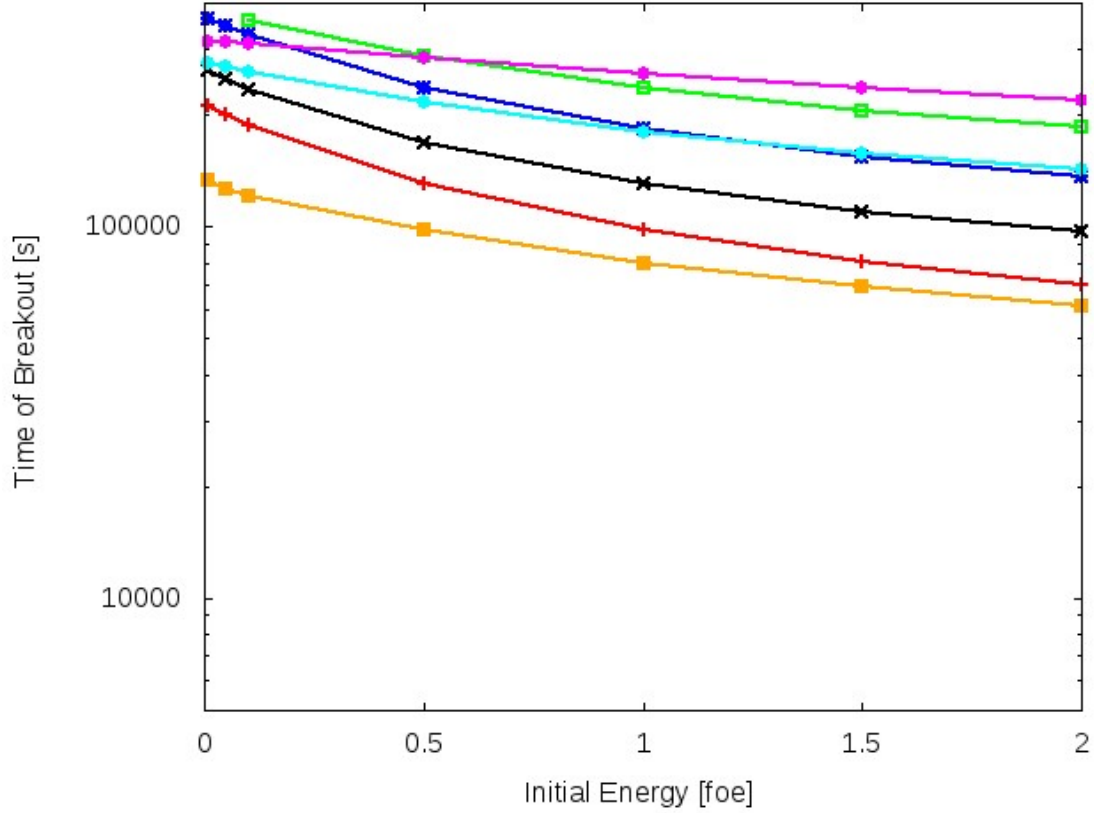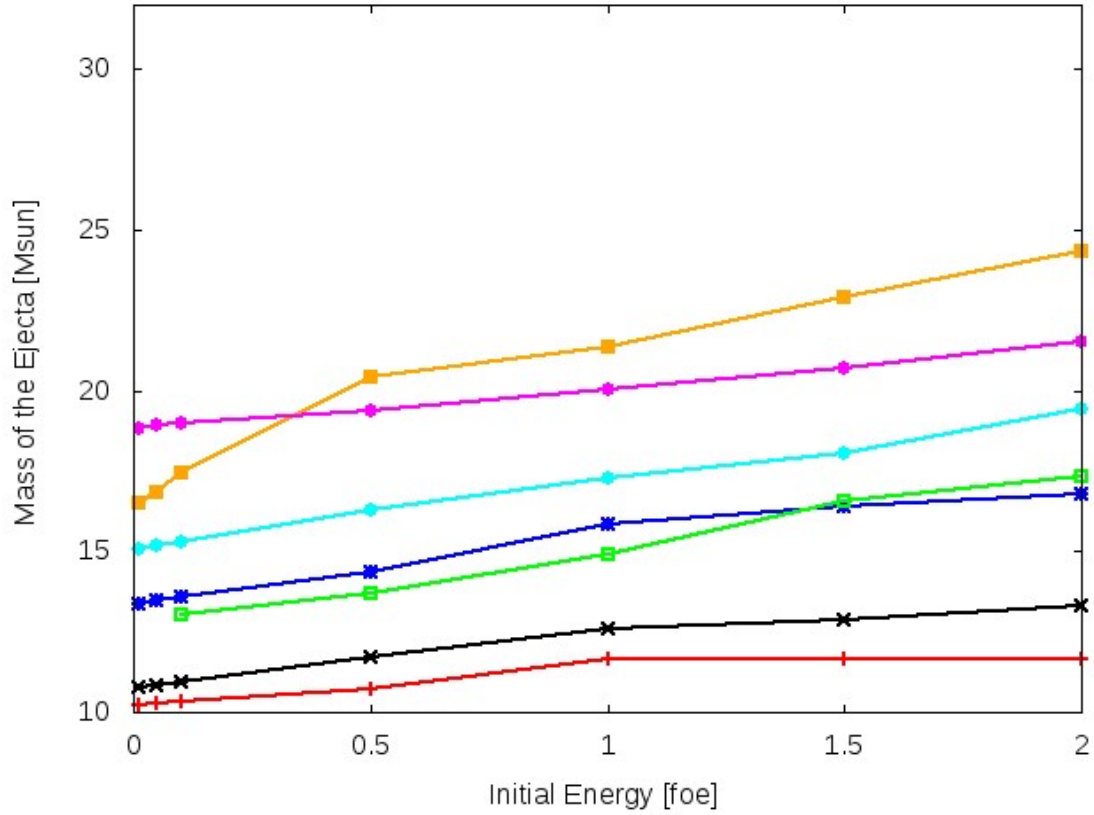
Figure 3.1: The time of the breakout as a function of the explosion energy for different stellar progenitors with initial metallicity of [Fe/H]=-1. The lines refer to 13 $M_\odot$ (red), 15 $M_\odot$ (black), 20 $M_\odot$ (blue), 25 $M_\odot$ (green), 30 $M_\odot$ (orange), 40 $M_\odot$ (cyan) and 60 $M_\odot$ (magenta).

ejected in the explosion is also influenced by metallicity: the amount on ^{56}Ni in the ejecta decreases as metallicity decreases and this behaviour is particularly evident in massive progenitors. The trend of this quantity is reported in figures 3.3 and 3.4.

The mass of the ejecta i.e. the quantity of matter actually ejected after the explosion, obviously shows an opposite behaviour with respect to the mass of the remnant. The mass of the ejecta is maximized when the explosion energies are high, and it decreases when the initial mass of the progenitor grows. We report two figures (3.5 and 3.6) describing the trend of the mass of the ejecta for two different metallicities.
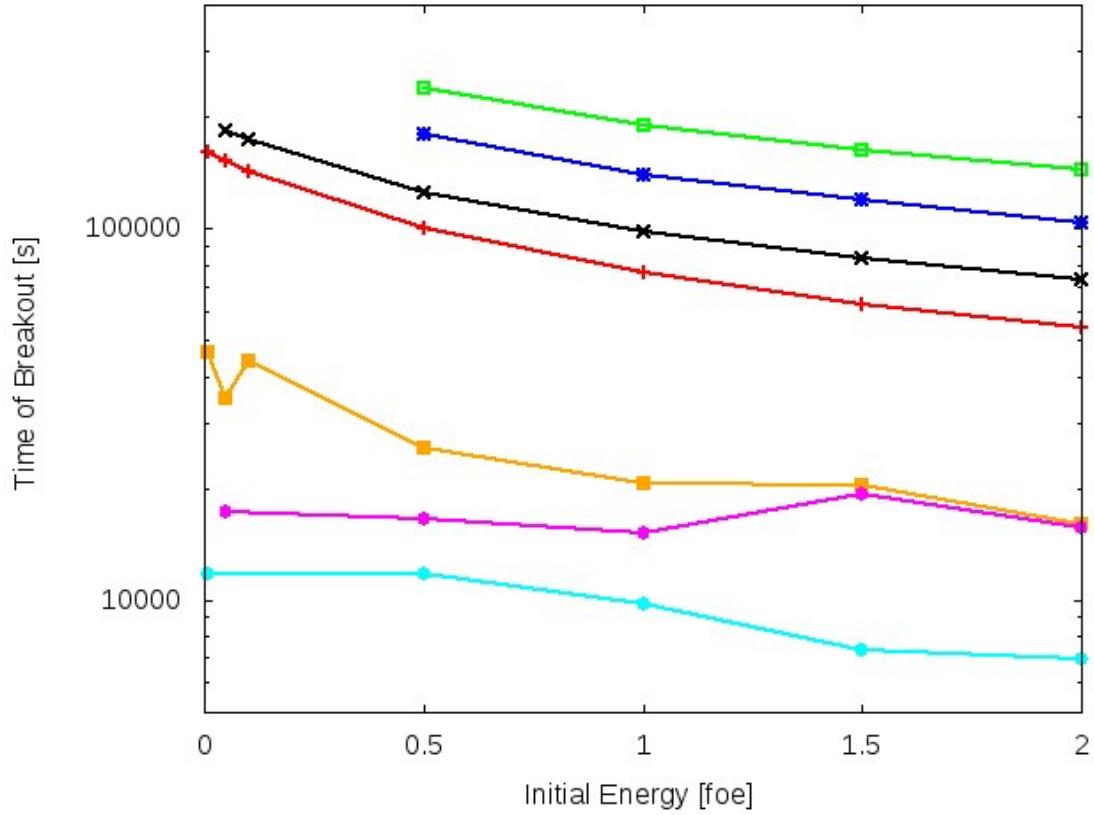
Figure 3.2: Similar to figure 3.1, but for a metallicity of [Fe/H]=-3

In the simulations we also calculated the kinetic energy of the ejecta which slightly grows with the mass of the progenitor and with the energy of the explosion, while it slightly decreases when the metallicity is increased. This is the expected trend since the ejecta are directly linked to the energy of the explosion itself: a greater quantity of energy injected in the model means an high kinetic energy of the ejecta.

Considering the obtained values, we can note how the mass of the remnant is increased with the increasing of the mass of the progenitor and decreases when the energy of the explosion grows: the physical reasons behind this behaviour are the same as in the case of the fallback time analyzed before.
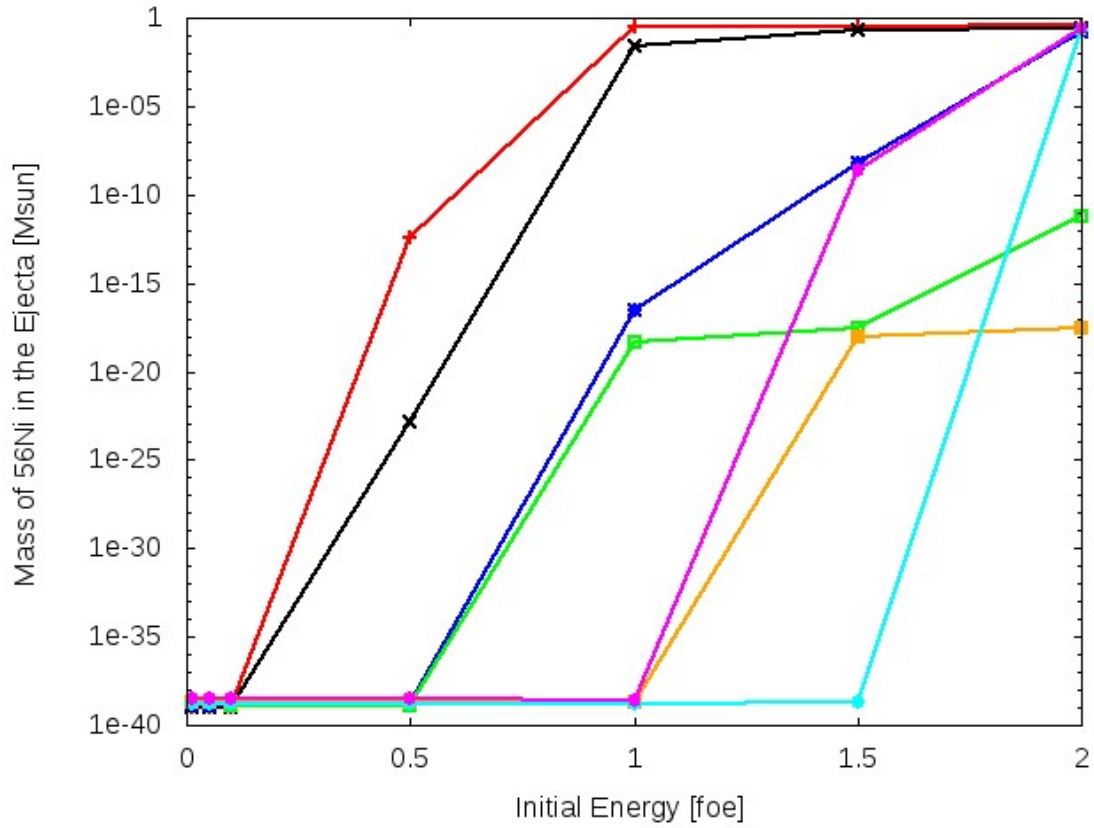
Figure 3.3: Amount of ^{56}Ni in the ejecta as a function of the explosion energy for different stellar progenitors with initial metallicity of [Fe/H]=-1. The lines refer to 13 $M_\odot$ (red), 15 $M_\odot$ (black), 20 $M_\odot$ (blue), 25 $M_\odot$ (green), 30 $M_\odot$ (orange), 40 $M_\odot$ (cyan) and 60 $M_\odot$ (magenta). Low values of ^{56}Ni are the ones obtained during the hydrostatic nucleosynthesis, this means all the ^{56}Ni synthesized during the CCSN event is kept in the remnant.

Another feature studied is the value of the bolometric luminosity at 50 days. This value will be important in our fitting strategy presented in Chapter 4, and can give information about the physical features of the progenitor. In general the luminosity grows with the energy of the explosion. The luminosity, indeed, is linked to the radius of the structure (L is proportional to R and T, where L is the luminosity, R is the radius of the structure, T is the temperature, as also found in analytic models for the plateau [55]) and a more energetic explosion will cause the ejecta to expand
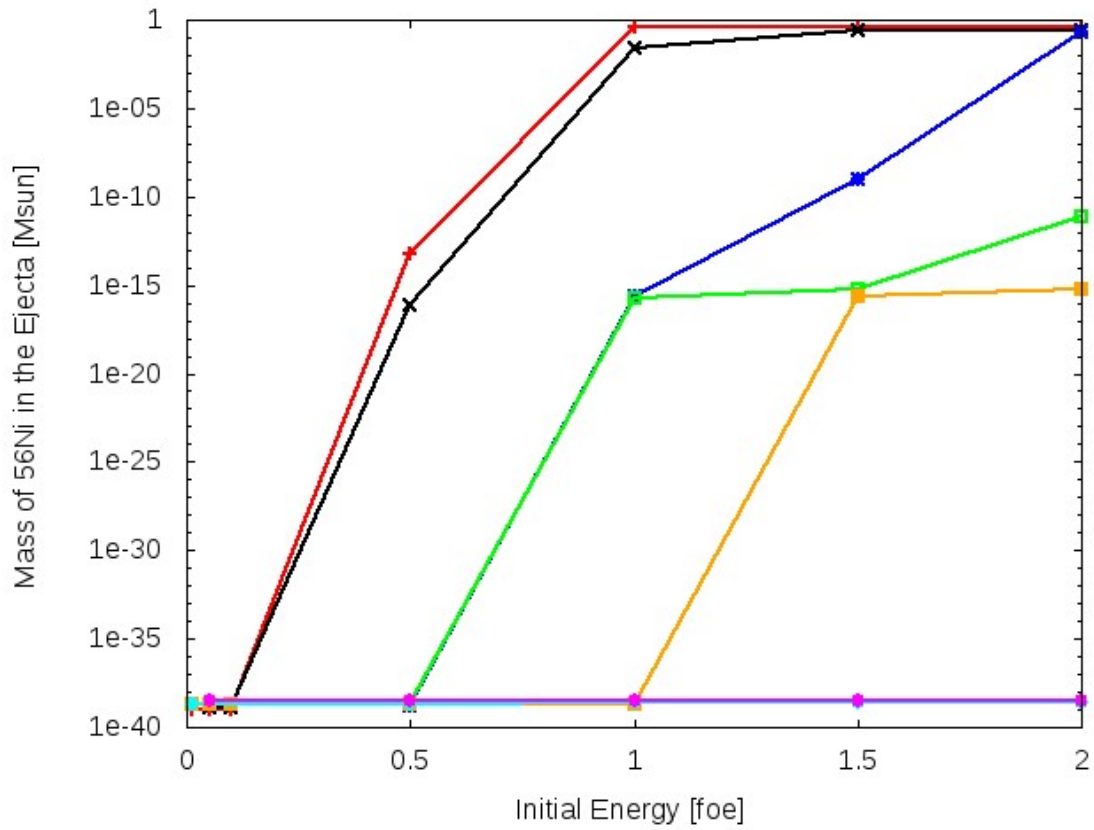
Figure 3.4: Similar to figure 3.3, but for a metallicity of [Fe/H]=-3

faster. In the same amount of time, the ejecta will cover a more extended portion of space and, due to the relation between L and R, a higher value for luminosity will be obtained. The luminosity at 50 day also grows when the mass of the progenitor does. We will talk more in depth about the bolometric luminosity in Chapter 4 concerning light curves.

3.3 Remnant Masses

After the description of some interesting values obtained in our simulations, we are going to focus our attention on the remnant masses: at first we will talk about of the dependence of these objects from the features of the progenitor and from the

Figure 3.5: The masses of the ejecta as a function of the explosion energy for different stellar progenitors with initial metallicity of [Fe/H]=-1. The lines refer to 13 $M_\odot$ (red), 15 $M_\odot$ (black), 20 $M_\odot$ (blue), 25 $M_\odot$ (green), 30 $M_\odot$ (orange), 40 $M_\odot$ (cyan) and 60 $M_\odot$ (magenta)

energy of the explosion, and then we will focus on the determination of the progenitor limiting mass between BH- or NS- forming CCSNe.

3.3.1 The dependence on the physical parameters

We found the values of the remnant masses to be in a huge range of values, including typical values for BHs and NSs.
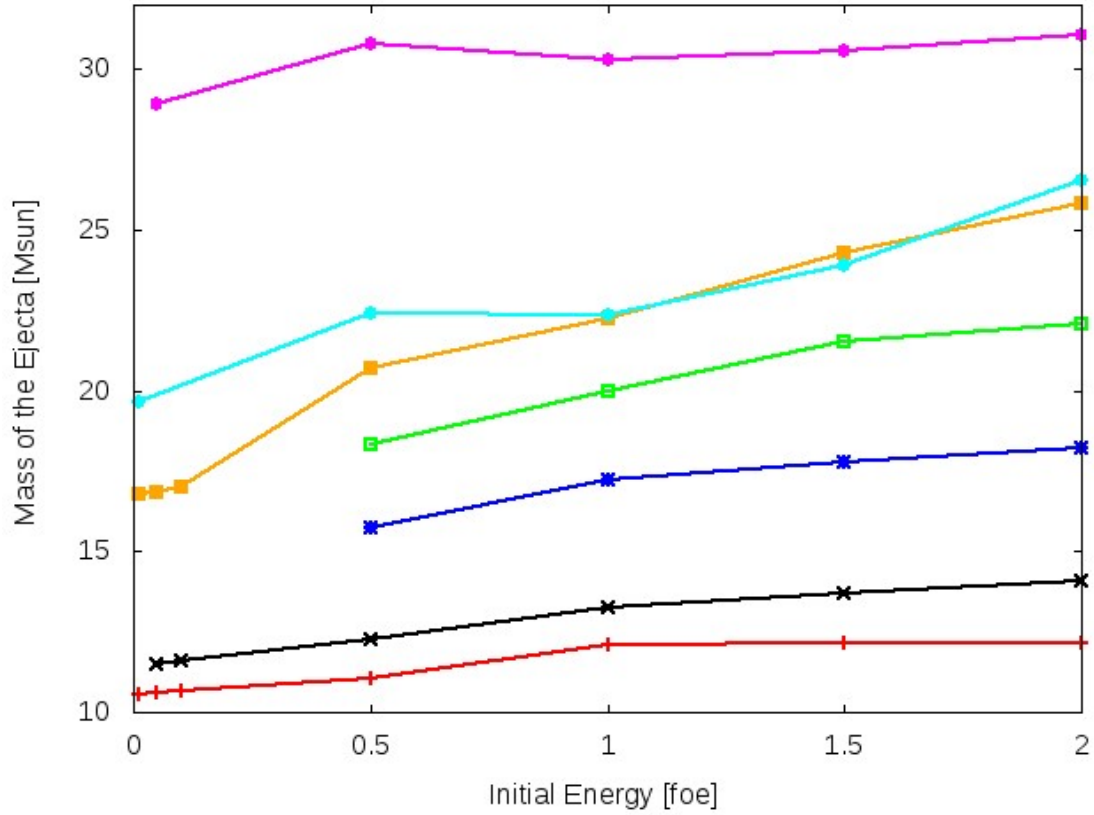
Figure 3.6: The same quantity reported in figure 3.5, but for an initial metallicity of [Fe/H]=-3.

Before starting the analysis of the outcomes obtained in the simulations, it could be useful to study the determination of the mass of the remnant in a single case to have a better understanding of the fallback phenomenon. In the figures 3.7 and 3.8 we show the time evolution of the radius of some zones of the progenitor star during the explosion: the model is the same in both the figures but, in 3.7, the energy of the explosion is 1 foe while in 3.8 the energy of the explosion is 2 foes.

Figures 3.7 and 3.8 clearly shown the fundamental role of the explosion energy in determining the ejecta and remnant masses. First of all we can note the differences in the radius of the two stellar remnants (the red lines in the figures): in the case illustrated by figure 3.7 the remnant results considerably larger than in case presented in figure 3.7. We can conclude that, as the energy of the explosion grows, the mass
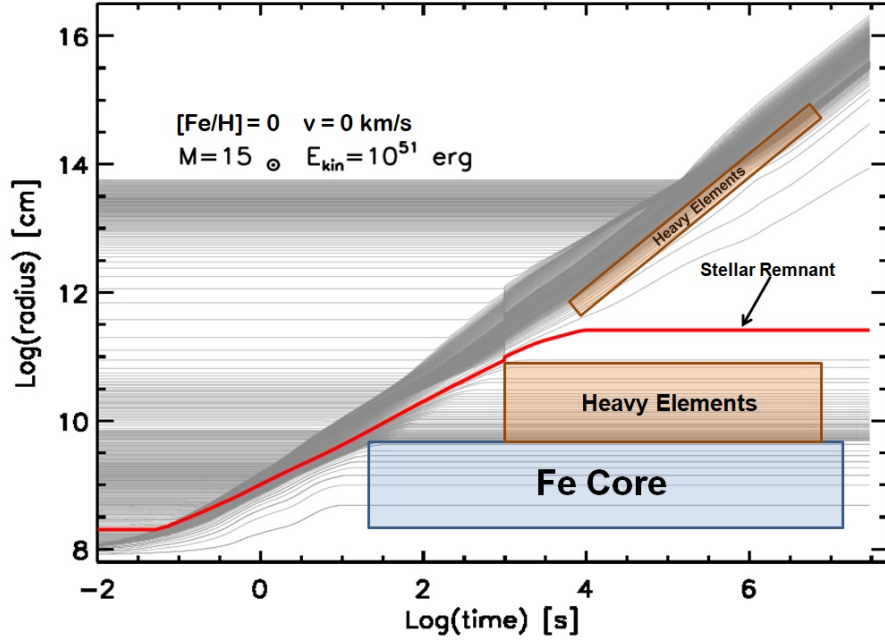
60

Figure 3.7: Time evolution of the radii of some zone of the stellar progenitor. The model is a 15 $M_\odot$ star with solar metallicity with 1 foe as energy of the explosion. The red line indicates the borders of the stellar remnant, while the colored boxes (not in scale) are there to point the different fate of the matter involved in the explosion. Once the envelope zone starts its way back towards the proto star remnant, we remove it from the calculation due to a lesser Courant time condition and therefore a shorter timestep which would have a huge computational weight: this is why the matter seems not to fall onto the proto star remnant. We investigated the possible influence of removing the in-falling zones from the calculation finding no relevant differences between this case and the same simulation with no zone removal. The condition whether a zone is infilling or not is found by calculating the escape velocity from the proto-remnant: under this value the zone is called back, otherwise is considered thrown away

.

of the remnant will be lower.

Furthermore, from these two figures, it is possible to estimate the duration of the fallback: in figure 3.7 in less than $10\,s$ the most internal zones begins to accumulate
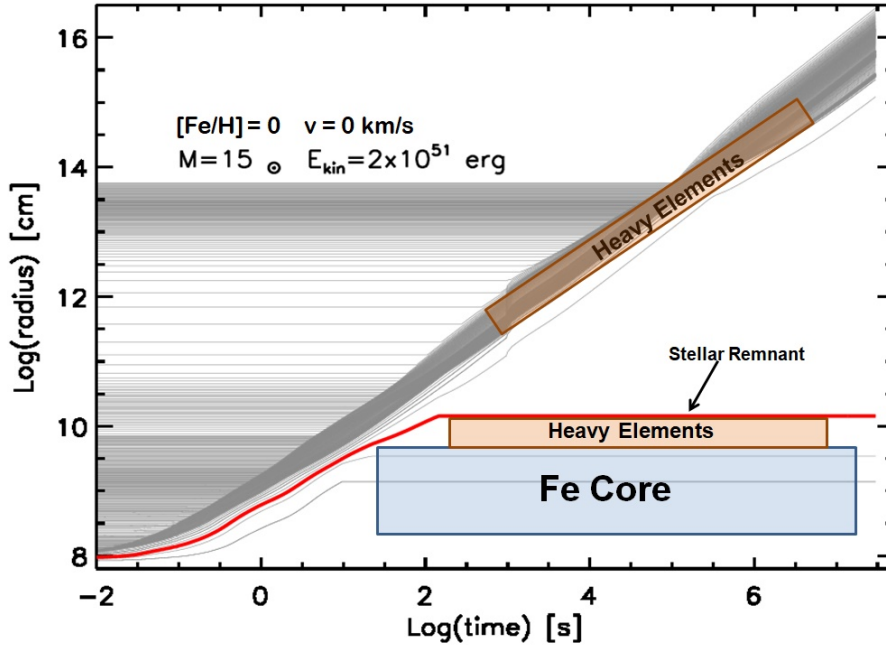
Figure 3.8: Similar to figure 3.7. Time evolution of the radii of some zone of the stellar progenitor. The model is a 15 $M_\odot$ star with solar metallicity with 2 foes of energy given. The red line indicates the borders of the stellar remnant, while the boxes (not in scale) are present to point the different fate of the matter involved in the explosion.

on the proto-remnant, and this process goes on up to (roughly) $10^4 s$ which means that the fallback ends in about 3 hours. In the other figure 3.8, instead, the times are sensibly lower: even if the fallback starts after $10\ s$ after the explosion the phenomenon is completed already $2.5 \cdot 10^2 s$ after the beginning of the explosion. This means that, in about 5 minutes, no further zones would be involved by the fallback. We have a confirmation of one trend explained in the previous paragraph: the time of the fallback decreases as the explosion energy grows.

From these figures (3.7 and 3.8) we can obtain information about the chemical composition of both the ejecta and the stellar remnants. In figure 3.7 the stellar remnant is composed by the Iron core and by a significant portion of heavy elements coming from both explosive or hydrostatic nucleosynthesis. In the same figure it is possible to note as the quantity of heavy metals in ejecta is extremely low: this

because those elements are completely swallowed by the fallback and only a tiny fraction is thrown away as ejecta. In the case of figure 3.8, instead, the greatest part of the heavy elements are found in the ejecta, and only a little fraction of them undergoes the action of the fallback. In this scenario the star remnant is practically only formed by Iron nuclei, while the ejecta, full of heavy elements, can pollute the nearby Space.

Leaving the single case, we will now consider the general results obtained for stellar remnants. In figure 3.9 we report the relation between the remnant mass and the initial mass of the progenitor obtained with an explosion energy of 1 foe in the set a. It is possible to note how the mass of the remnant grows with the mass of the progenitor: this naturally comes due to an increase of the binding energy of the progenitor. The layers of the envelope, indeed, are efficiently held by the Iron core and a great amount of matter will fall back on the proto-star remnant. It is possible to note how the steepness of the curve in figure changes drastically from 25 to $30\,M_\odot$: this happens due to the increasing of the Carbon-Oxygen core (table 3.2) in massive star which rises properly the binding energy of the structure.

Figure 3.10 shows how the remnant mass depends on the explosion energy: it is possible to note as if the energy of the explosion for the same stellar model grows, the outcome of the explosion would be a less massive stellar remnant and, thus, there will be an increasing quantity of matter ejected. It is possible to note as, for massive progenitor stars (higher than $40\,M_\odot$), the mass of the remnant seems to be less affected by the explosion energy and quite independent from this value: this is not a visual effect due to the logarithmic scale, but happens because, for such high masses, the binding energies of the progenitors are particularly hard to win with the span of energy used in this work. In these cases very low masses of ejecta are found.

We extended this analysis considering all the different metallicities treated: figures 3.11, 3.12, 3.13 represent the same results obtained respectively for set b, set c and set d. We also suggest to keep in mind 3.10 as further comparison.

In these figures (3.10,3.11, 3.12, 3.13) it is possible to note how the remnant masses tend to grow at the decreasing of the metallicty, which has fundamental role. This link is due to the fact that low metallicity stars are more compact object respect to metal-rich counterparts, increasing their binding energy. Due to this fact, the remnants from low metallicity stars with masses higher than $40\,M_\odot$ seem to be even less affected by the energy of the explosion. In figure 3.14 is reported a more direct
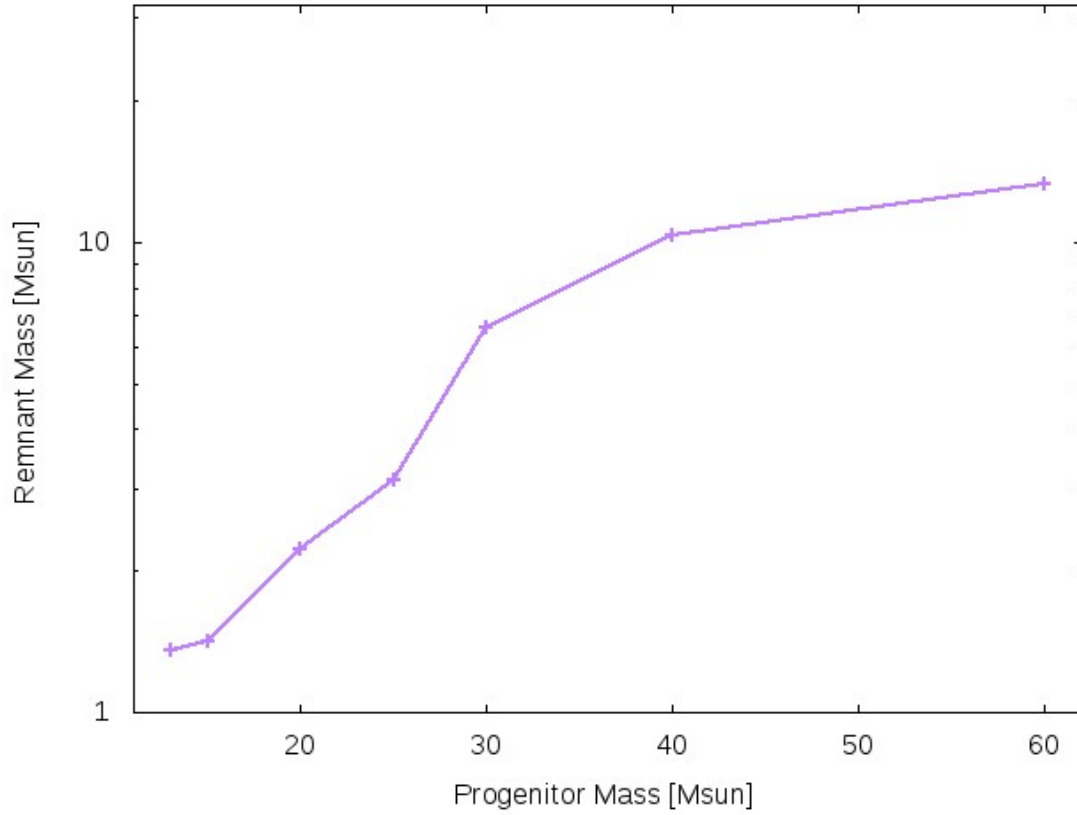
Figure 3.9: Remnant mass as function of the progenitor initial mass. This quantity is calculated for an explosion energy of 1 foe on [Fe/H]=0 models

visual comparison of the role played by metallicity in determining the remnant mass for a single explosion energy, and it is clearly shown the behaviour described.

In the analysis led so far we did not include the outcomes obtained for the simulations of 80 $M_\odot$ in set d. Those values have been excluded because they do not have a counterpart at higher metallicity. The values obtained, however, have been reported in table 3.6 and will be analyzed in the next paragraph.
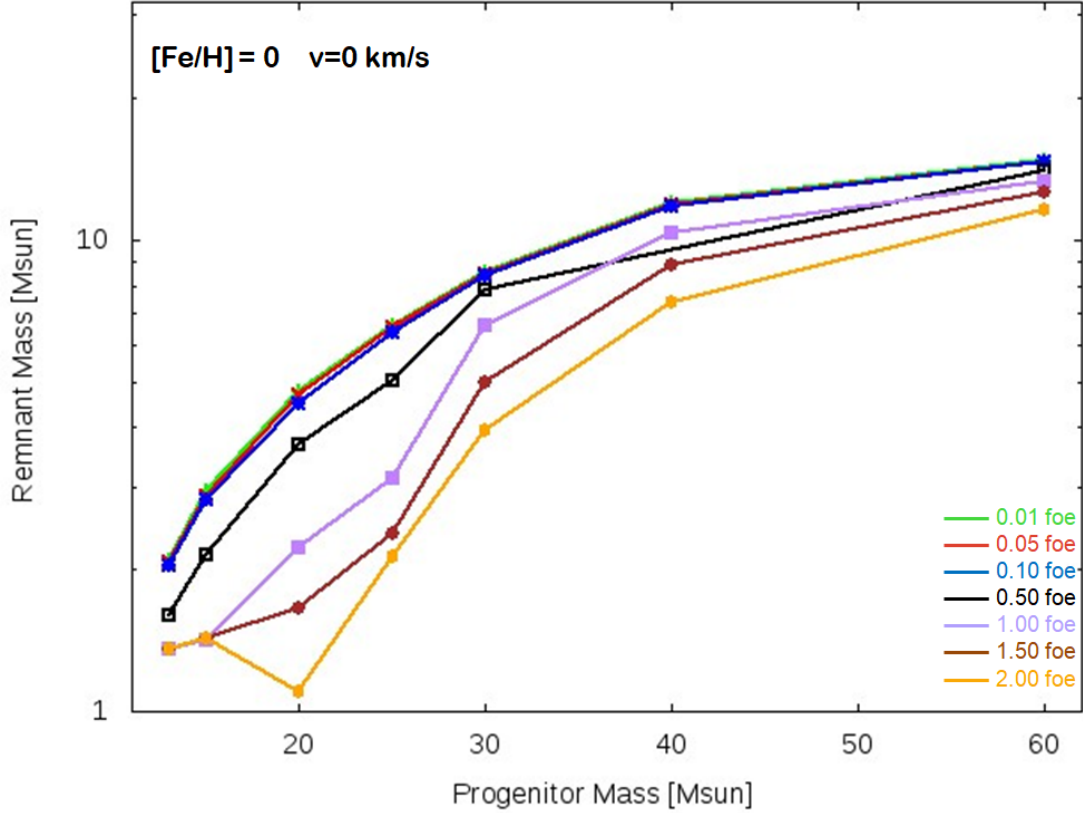
Figure 3.10: Remnant mass in function of the progenitor initial mass. In this case all the results are obtained for a metallicity of [Fe/H]=0 calculated at different explosion energies.

3.3.2 The limiting progenitor mass between NS and BH

In such a work with a huge number of simulations carried out, it is a natural consequence to reach some predictions. In this section we will investigate the limiting mass of the progenitor which, starting from certain physical features and explosion energy, could form a NS or a BH after the explosion. We defined the observational ranges in mass for NS and galactic BH in the introduction. In this case we will use, as comparison, a more strict limit in mass considering NS a remnant which mass is inferior to 2.5 $M_\odot$, otherwise, all those objects exceeding this mass limit will be considered BHs. For the same value of metallicity and explosion energy, the calculation
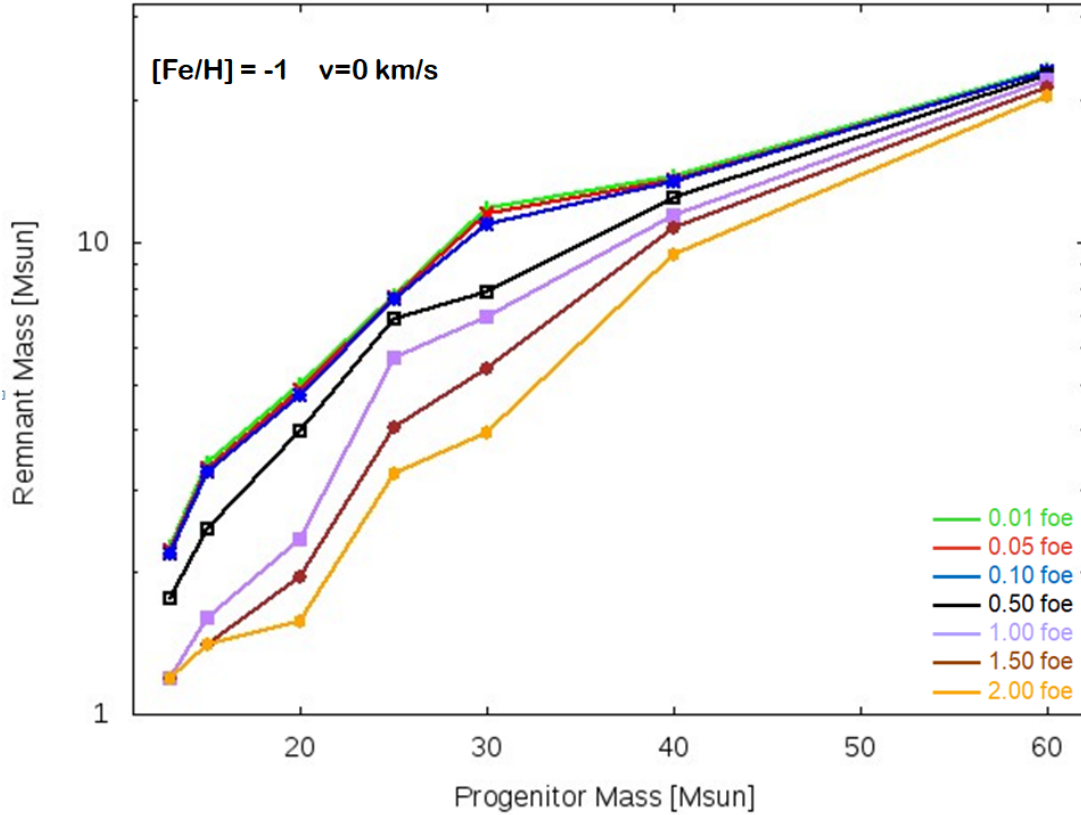
Figure 3.11: Remnant mass in function of the progenitor initial mass. In this case all the results are obtained for a metallicity of [Fe/H]=-1 calculated at different explosion energies.

of the limiting masses are obtained by doing an arithmetic average over the greatest mass of the progenitor which forms a NS and the lower mass of the progenitors which forms a BH.

In table 3.7 we reported the data obtained for the limiting progenitor mass between NS and BH for different energies and for all the metallicty considered. The data could also be shown in a visual way by the figure 3.15.

Both from table 3.7 and from figure 3.15 it is possible to notice the general trend about the limiting NS-BH mass: at low values of metallicity the limiting mass decreases because the progenitor is more compact than high metallicity counterparts
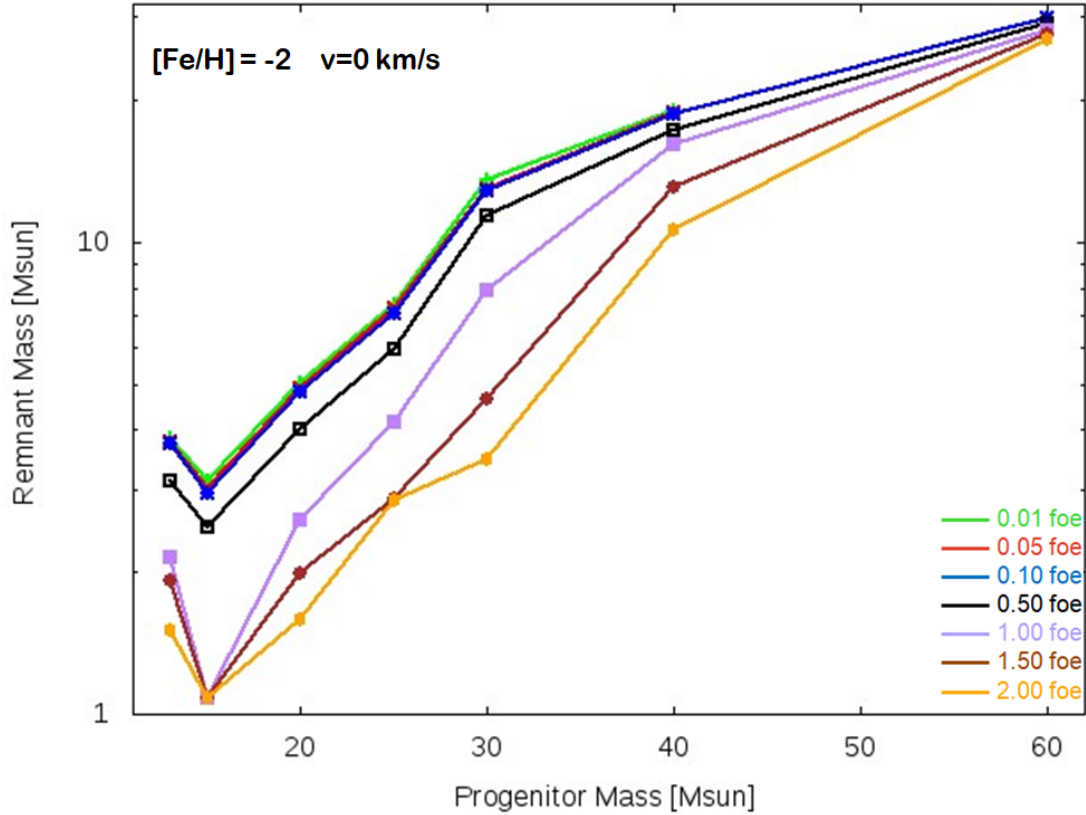
Figure 3.12: Remnant mass in function of the progenitor initial mass. In this case all the results are obtained for a metallicity of [Fe/H]=-2 calculated at different explosion energies.

and the remnant would be more massive considering the same value of the explosion energy. Consequently BHs are formed at relatively low progenitor masses. As expected, we found that the minimum mass between a NS- and BH-forming progenitor star grows as the explosion energy grows.

We should always consider the theoretical upper limiting mass for SBH, which is (how described in the introduction) about $80 M_{\odot}$. From the results of our simulations, we found that none of the examined models, at the span of energy used, could form such a massive remnant even if it seems more likely to happen in low metallicty high massive stars with low values of explosion energies.
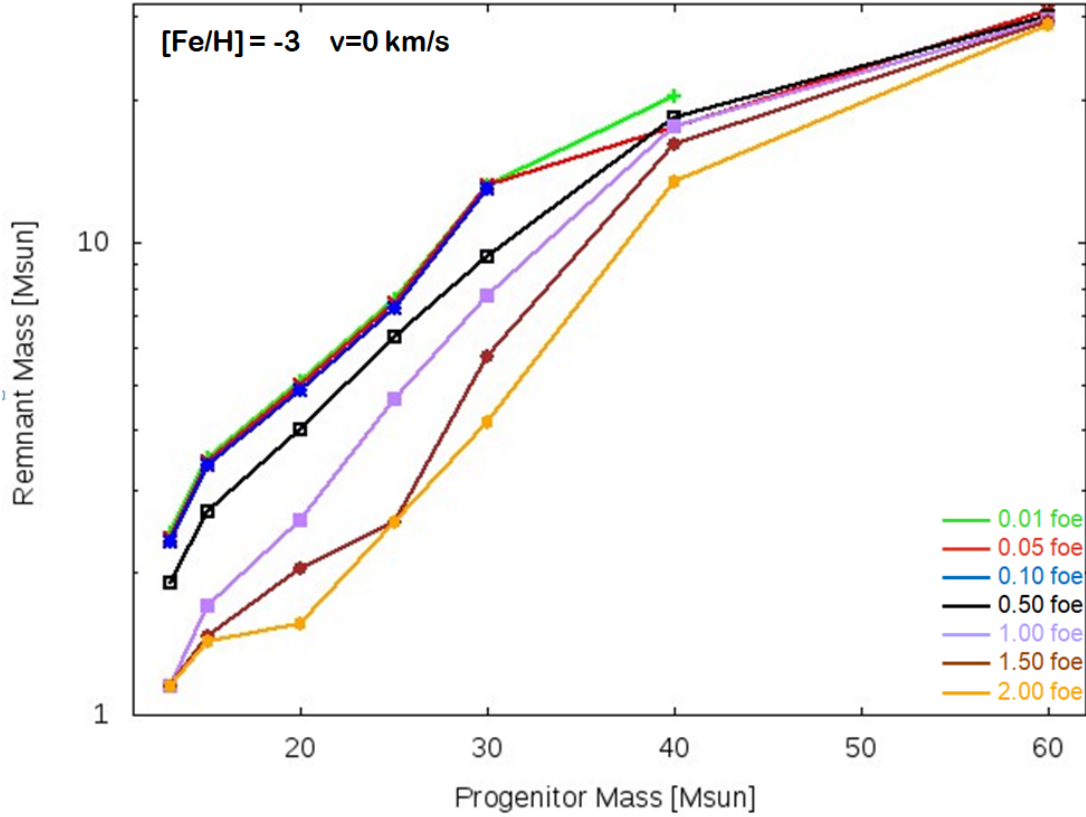
Figure 3.13: Remnant mass in function of the progenitor initial mass. In this case all the results are obtained for a metallicity of [Fe/H]=-3 calculated at different explosion energies.

3.3.3 Comparison with other theoretical Remnant Masses

In this paragraph we compared the remnant masses obtained using HYPERION with the ones obtained, theoretically, by other authors. As comparison we chose two works: the first one is by Sukhbold and Ertl [66], the second one is by Frye and Andrews [27]. Both the works are devoted to calculate the remnant mass on a set of presupernova models by injecting a certain amount of energy simulating a CCSN explosion. In [66] the energy is given by a certain rate calibrated to reproduce the explosion observed in SN 1987A. In [27] the energy is given to mimic different kind of engines. Since this is a comparison we want to have data in the most similar
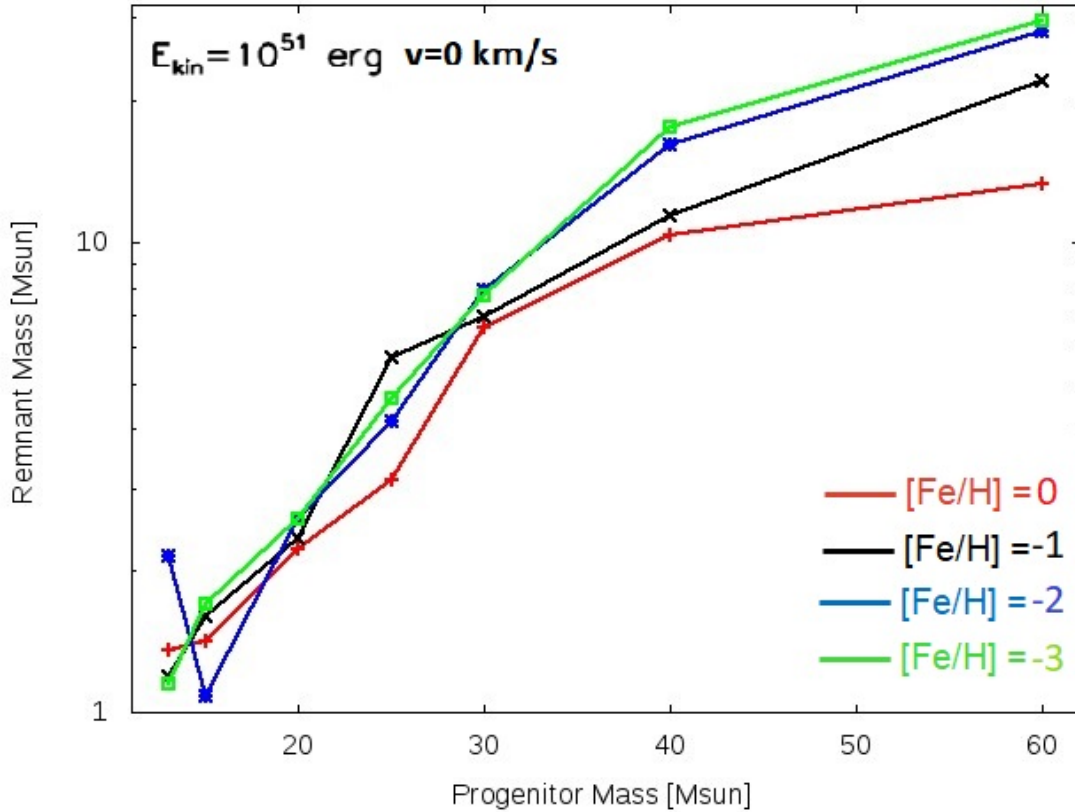
Figure 3.14: Remnant mass in function of the progenitor initial mass. This figure shows the behaviour of the remnant mass at four different metallicity ([Fe/H]=0 red, [Fe/H]=-1 black, [Fe/H]=-2 blue, [Fe/H]=-3 green) obtained with an explosion energy of 1 foe.

conditions possible: at solar metallicity we considered the remnant masses coming from four different progenitors, in particular 13, 15, 20 and 25 $M_\odot$ (even if [27] does not treat the 13 $M_\odot$ case, and [66] uses masses close to these values) using explosion energies close to 1.00 foe. If the precise values for progenitor mass and explosion energy are not available in the works we examined, we chose the closer values. In table 3.8 we report the values of the remnant masses obtained by all these works, together with the values of progenitor mass and explosion energies used to obtain the SR. Figure 3.16 shows a clearer comparison between the four cases examined.

Table 3.7: Limiting progenitor NS-BH mass for the model examined at different metallicity and energy of the explosion. LM stands for Limiting Mass.

Initial Energy $(10^{51}erg)$	LM ([Fe/H]=0) $(M_\odot)$	LM ([Fe/H]=-1) $(M_\odot)$	LM ([Fe/H]=-2) $(M_\odot)$	LM ([Fe/H]=-3) $(M_\odot)$
0.01	14.00	14.00	13.00	14.00
0.05	14.00	14.00	13.00	14.00
0.10	14.00	14.00	13.00	14.00
0.50	17.50	17.50	17.50	14.00
1.00	22.50	17.50	22.50	17.50
1.50	27.50	22.50	22.50	22.50
2.00	27.50	27.50	27.50	22.50

Table 3.8: Remnant masses in $M_\odot$ found by three different works (first column HYPERION, second column [66] and third column [27]) together with the values for the progenitor masses in $M_\odot$ and the explosion energies in foe. The four sections of the table represent the four compared values for the remnant masses at similar progenitor mass and explosion energy: the first refers to the 13 $M_\odot$ case, the second to the $15M_\odot$ case, the third to the $20M_\odot$ case and the fourth to the $25M_\odot$ case.

	HYPERION	Sukhbold et al.	Fryer et al.
Progenitor Mass ($M_\odot$)	13.0	13.1	X
Explosion Energy (foe)	1.00	1.11	X
Remnant Mass ($M_\odot$)	1.36	1.60	X
Progenitor Mass ($M_\odot$)	15.0	14.9	15.0
Explosion Energy (foe)	1.00	1.04	0.98
Remnant Mass ($M_\odot$)	1.43	1.78	1.89
Progenitor Mass ($M_\odot$)	20.0	20.1	20.0
Explosion Energy (foe)	1.00	0.82	1.00
Remnant Mass ($M_\odot$)	2.23	1.82	2.35
Progenitor Mass ($M_\odot$)	25.0	25.4	25.0
Explosion Energy (foe)	1.00	0.86	0.99
Remnant Mass ($M_\odot$)	3.13	1.88	4.89
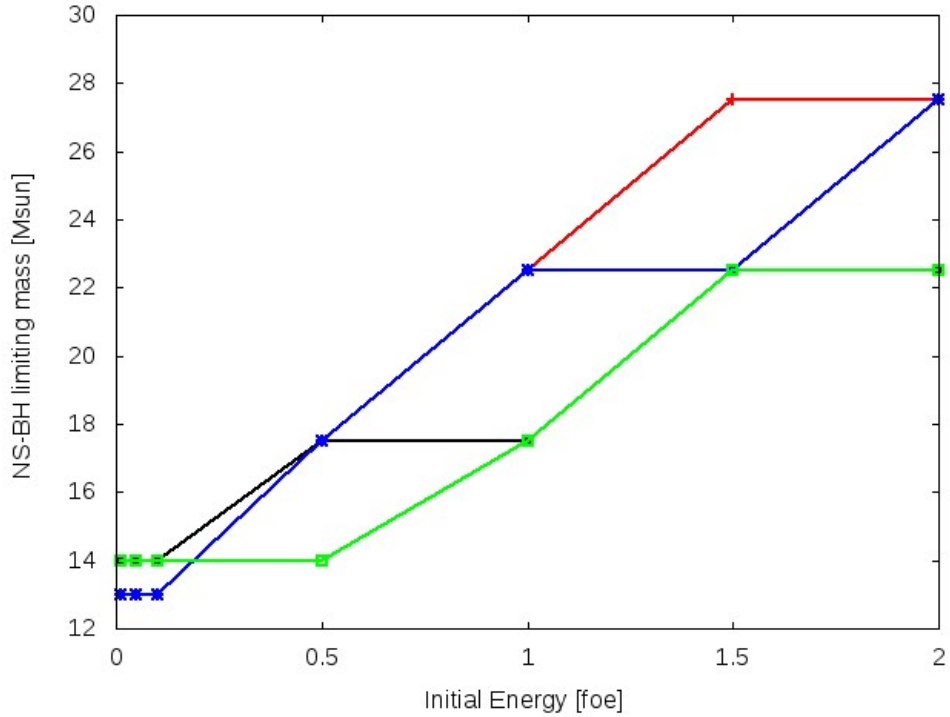
Figure 3.15: Limiting NS-BH mass in function of the energies of the explosion at different metallicities: red [Fe/H]=0, black [Fe/H]=-1, blue [Fe/H]=-2 and green [Fe/H]=-3.

By the analysis of both table 3.8 and figure 3.16, we can state that all the examined values of the remnant masses show some differences, in particular at high progenitor masses. Those differences may come both from the presupernova models or from the manner in which the energy is injected (the form, the position or even the duration of the injection) into the model. Even the general trend of the results seems to be different: linear in our case, exponential in the values found by [27] and quite constant in the values found by [27]. A more accurate analysis could be led by using exactly the same initial values for energies and progenitor mass with exactly the same method of injecting the energy into the model.
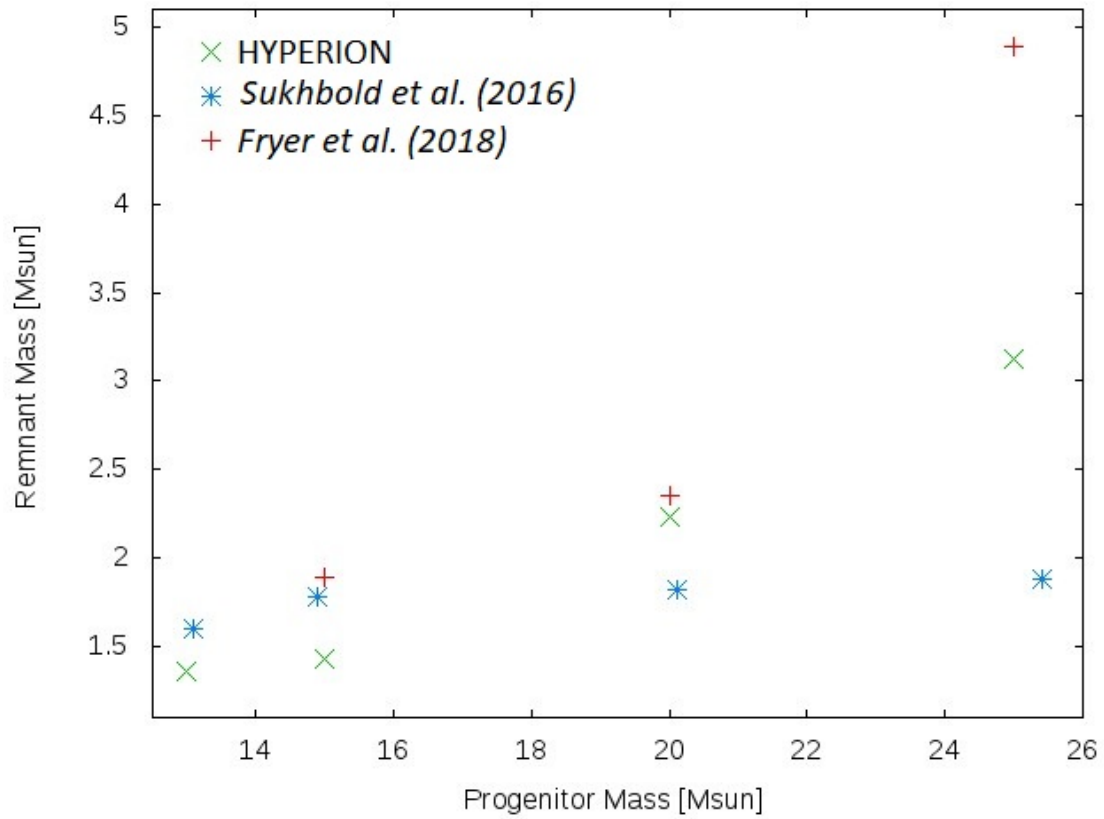
Figure 3.16: Remnant mass in function of the progenitor mass obtained with the values described in table 3.8. The light blue X signs stands for the values obtained with HYPERION, the blue asterisks are the values obtained by Sukhbold et al. [66], while the black crosses represent the values found by Frye et al. [27].

Chapter 4

Light curves

4.1 SN II-P light curves, a description

By means of the code presented in the Chapter 2 we computed the light curves obtained during the explosion. In this pharagraph we will present a typical II-P LC obtained from our simulations, then the link between the features of the progenitor star and the LCs are analyzed, then we will show some comparisons of the LCs obtained with our code and the observed data.

4.1.1 From the explosion to the shock breakout

The LC is obtained starting from a presupernova model of $15.0\,M_\odot$, solar metallicity, without rotation [45], and with an explosion energy of 1 foe (model 15A). This setting leads to a Type II-P explosion from a RSG progenitor star: some information about the progenitor star have been already given in tables 3.1 and 3.2, moreover in figures 4.1 and 4.2 we reported, respectively, the profiles in mass of temperature and density and the internal chemical composition of the model.

To start the explosion, the amount of chosen energy is injected, in a shell of $0.1\,M_\odot$ starting at a mass coordinate of $0.8\,M_\odot$ from the center of the progenitor, thus inside the Iron core.

This energy accelerates and compresses the matter over the local sound speed giving birth to a shock wave: this shock wave begins to move outward from the Iron core of the star. During its passage, the matter encountered is heated up and pulled outward. As a result, the shock wave loses energy as a spherical wave. In this way
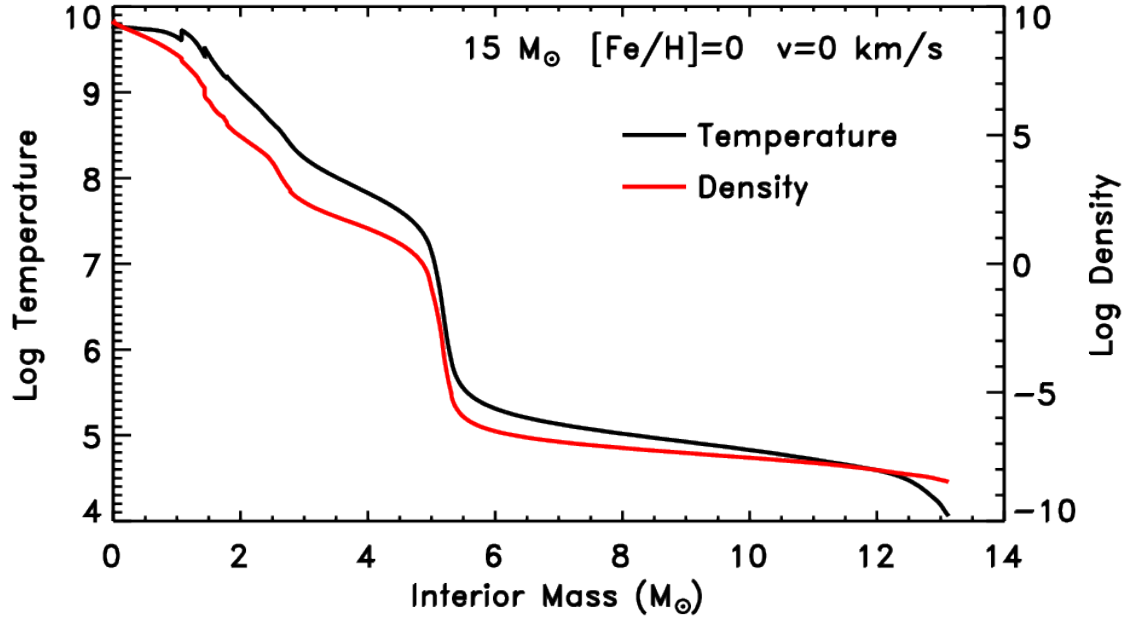
Figure 4.1: Behaviour of the density (red line) and the temperature (black line) in function of the mass of model 15A before the explosion.

the total amount of gravitational and internal energy is progressively converted into kinetic energy. It is important to note how the temperature behind the shock wave remains constant due to the fact that the energy is dominated by the radiation. In figure 4.3 we report the evolution of temperature, density and velocity at different times before the shock breakout.

During the first stages of the explosion the temperature reaches values of about $7 \cdot 10^9 K$: at similar conditions explosive nucleosynthesis may occurs. The explosive nucleosynthesis acts in a very short time because already after $0.7 s$ since the moment of the explosion (when the shock wave reaches the presupernova C-convective shell at $2.1 M_\odot$), it can be considered over because the temperature behind the shock wave decreased to $2 \cdot 10^9 K$ making these chemical reactions inefficient. The zone between the edge of the Iron core and ~ 1.55 M$_\odot$ undergoes explosive Si burning with complete Si exhaustion and is dominated by ^{56}Ni (^{56}Fe), which is by far the most abundant nuclear species (the total ^{56}Ni ejected in this model is 0.126 M$_\odot$). Other abundant isotopes in this zone are ^{58}Ni, ^{57}Ni (^{57}Fe), ^{60}Zn (^{60}Ni), ^{62}Zn (^{62}Ni)
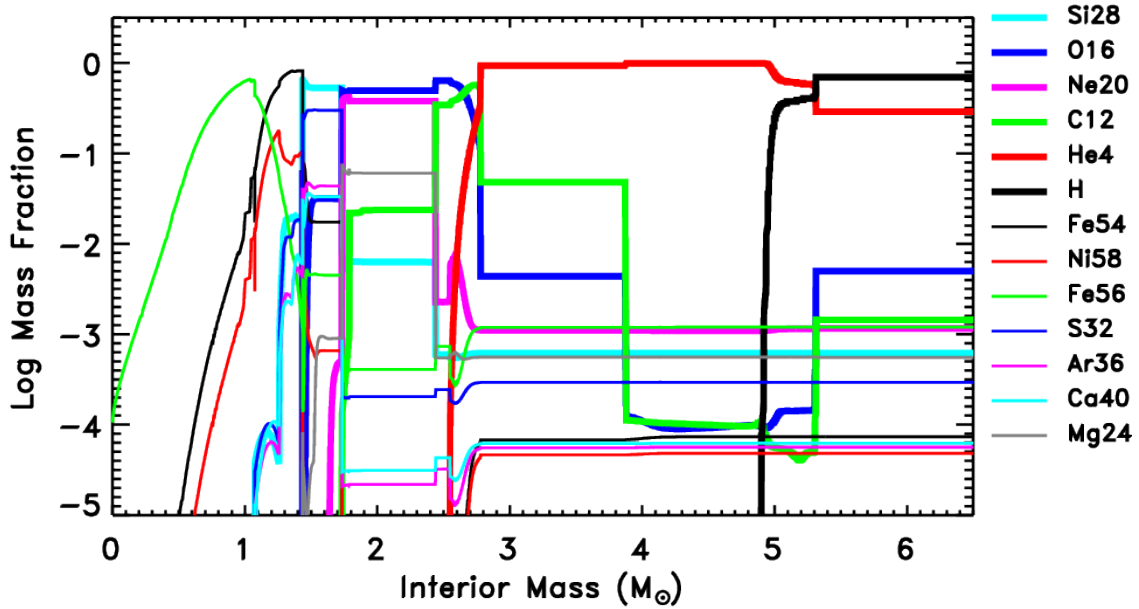
Figure 4.2: Internal chemical composition of 15A in the first $6.5 M_\odot$ (thereon a flat abundance of H and He is set, and we chose to represent more in detail the inner part) in function of the mass

and ^{4}He (the unstable nuclei will decay at late times into their parent stable isotopes reported in parenthesis). The outcomes of the explosive Si burning can be found in figure 4.4.

The layers between ~ 1.55 M$_\odot$ and ~ 1.69 M$_\odot$ undergoes explosive Si burning with incomplete Si exhaustion and are mainly loaded with the iron peak elements ^{56}Ni, ^{58}Ni, ^{57}Ni (^{57}Fe), ^{54}Fe, ^{55}Co (^{55}Mn), ^{52}Fe (^{52}Cr), and the alpha nuclei ^{32}S, ^{40}Ca, ^{36}Ar and ^{28}Si (the one that remains partially not burnt). The outcome of this stage are found in figure 4.5.

Explosive O burning occurs in the region between ~ 1.70 M$_\odot$ and ~ 1.77 M$_\odot$ and produces mainly the alpha elements ^{28}Si, ^{32,34}S, ^{36,38}Ar and ^{40}Ca. The outcomes of explosive O burning can be found in the figure 4.6
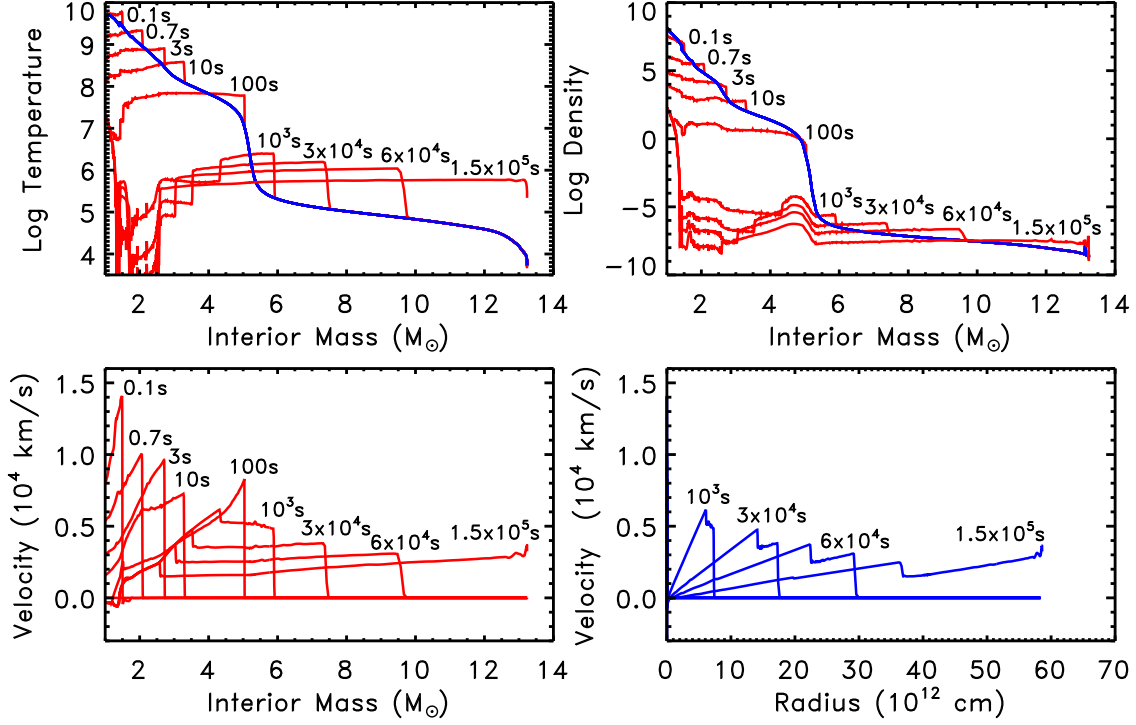
Figure 4.3: Main physical and chemical properties of model 15A at various times during the explosion. Top left: temperature in function of the interior mass. Top right: density in function of the interior mass. Bottom left: velocity in function of the interior mass. Bottom right: velocity in function of the radius.

Explosive Ne burning occurs in the zones between ~ 1.77 M$_\odot$ and ~ 2.10 M$_\odot$ and produces or partially modify (destroy or produce) the presupernova abundances of ^{16}O, ^{20}Ne, ^{23}Na, ^{24,25,26}Mg, ^{27}Al, ^{28,29,30}Si and ^{31}P. The results of the explosive Ne burning are shown in figure 4.7.

Explosive C burning is almost negligible because of the very low ^{12}C mass fraction present inside ~ 2.1 M$_\odot$. Even if the effective timescale for explosive nucleosynthesis is shorter than a second, in our simulations we considered also the decays of some unstable isotopes: to grant a reliable quantity of decays to happen we considered the chemical composition able to evolve up to $2.5 \cdot 10^4 s$.
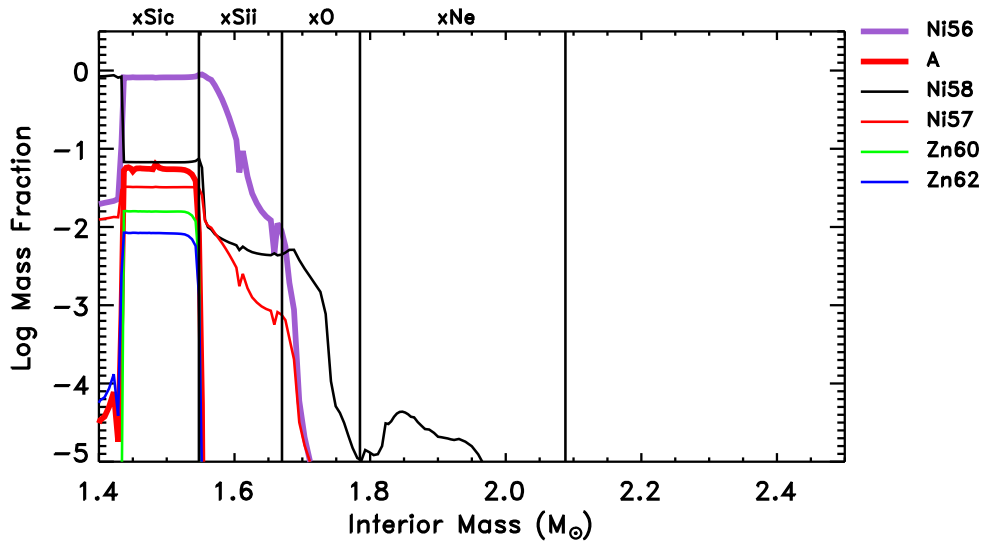
Figure 4.4: Profile of the most abundant isotopes produced by the explosive Si burning with complete Si exhaustion in the zone between the edge of the iron core and ~ 1.55 M$_\odot$.

When the shock wave reaches the border of the CO core at 2.1 $M_\odot$ in about 3 s, the quantity of kinetic energy in the layers interested by the shock wave, due to their velocities $(3.0 \cdot 10^4 - 9.5 \cdot 10^4 km/s)$, becomes comparable with the internal energy. After 10 s from the onset of the explosion, the fallback starts: this phenomenon will continue up to some hours as it is illustrated in figures 3.7 and 3.8. In about 10^2 s the shock wave encounters a steep density gradient corresponding to the transition from the Helium-rich to the Hydrogen-rich envelopes (figure 4.1). As a consequence the shock wave slows down and a reverse shock wave which propagates inward in mass forms. In this way we have the simultaneous presence of both an outward shock wave and an inward reverse wave which decelerates the matter previously accelerated by the outgoing shock wave. This reverse shock wave has an important role in determining the amount of matter involved in the fallback. The analysis of the component of the energy reveals that the layers under (in position) the reverse shock wave are dominated by kinetic energy, while the internal energy grows in the most external layers, as is shown in figure 4.8.

After 10^4 seconds from the onset of the explosion, the fallback has ceased and we found a remnant with a total mass of about 1.42 $M_\odot$ (the mass has grown after the
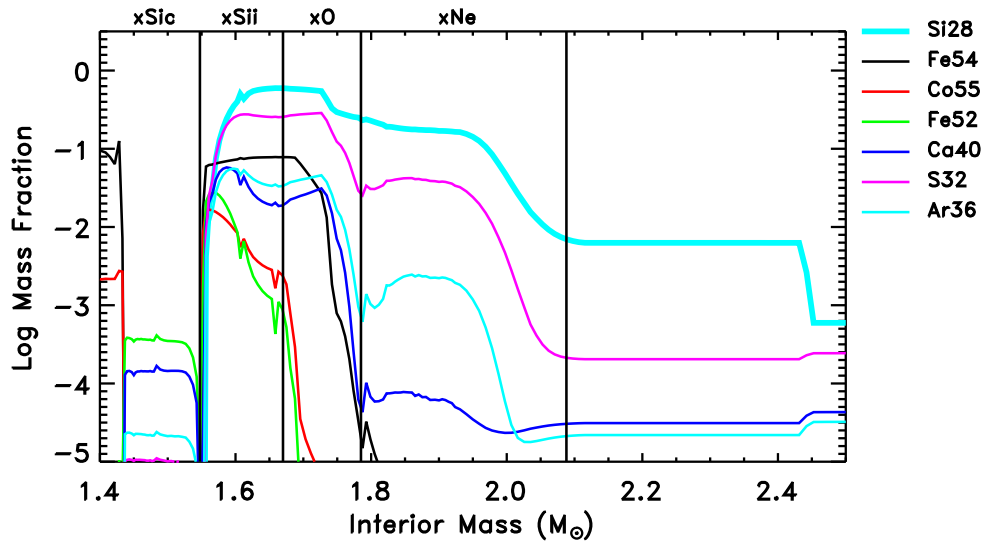
Figure 4.5: Profile of the most abundant isotopes produced by the explosive Si burning with incomplete Si exhaustion in the zone between ~ 1.55 M$_\odot$ and ~ 1.69 M$_\odot$.
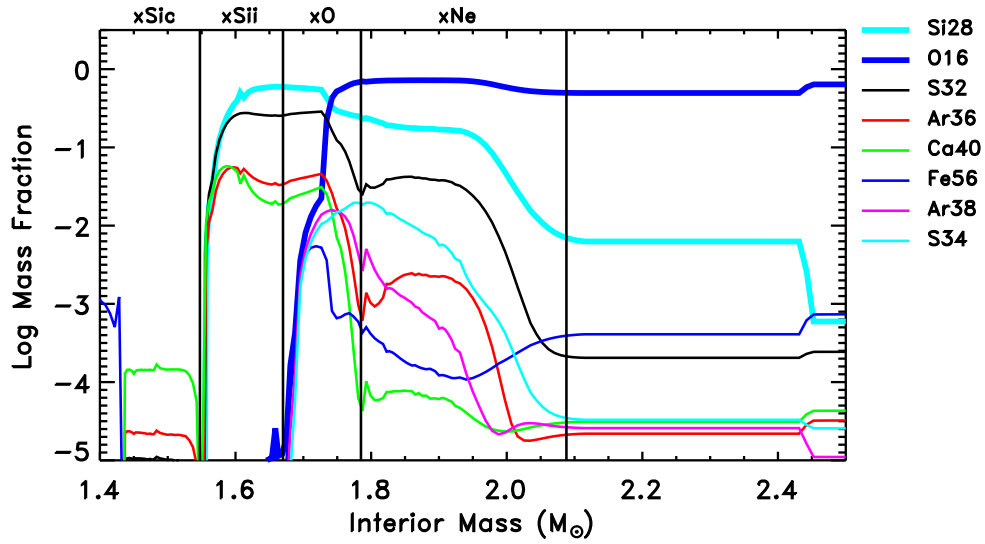
Figure 4.6: Profile of the most abundant isotopes produced by the explosive O burning in the zone between ~ 1.70 M$_\odot$ and ~ 1.77 M$_\odot$.
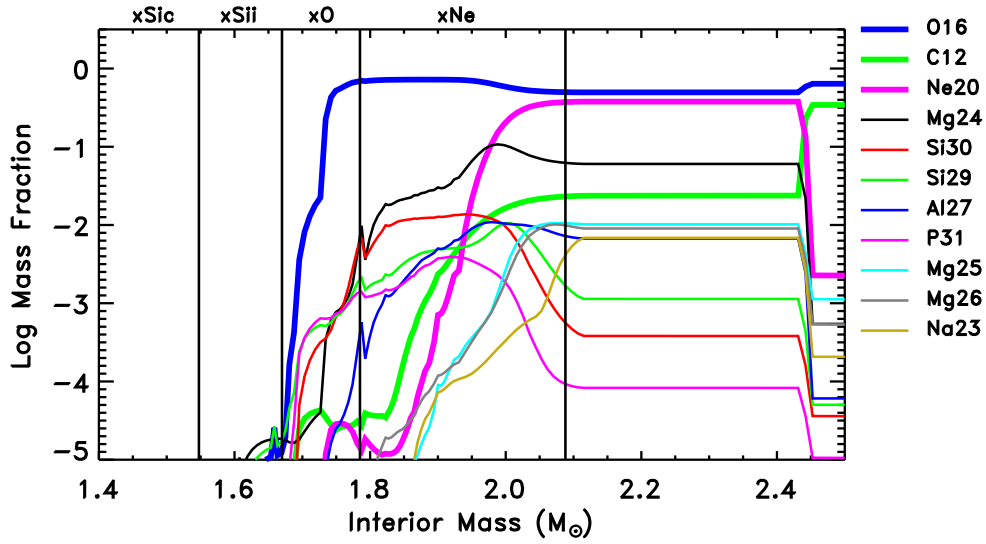
Figure 4.7: Profile of the most abundant isotopes produced by the explosive Ne burning in the zone between ~ 1.77 M$_\odot$ and ~ 2.10 M$_\odot$.

fallback, since the Iron core had a mass of $1.24\,M_\odot$) and this means that a part of the matter which undergoes the explosive nucleosysnthesis has not been ejected (lesser pollution of heavy elements).

At $1.5 \cdot 10^5 s$ the outward shock wave reaches the surface of the star: as a consequence of the hydrodinamical accumulation, both the temperature and the bolometric luminosity increase respectively to $2 \cdot 10^5 K$ and $2 \cdot 10^{45}\ erg/s$ as it is shown in figure 4.10 and, more in detail, in figure 4.9. This is the shock breakout i.e. the first observational data we can collect from a CCSN (neglecting the neutrino emission): in this moment, the bolometric luminosity reaches its maximum and, due to the high temperature, the peak of emission for this radiation is in the UV band. When the outward shock wave reaches the surface, the mantle of the exploding star is completely ionized. We must specify that in this moment the inner part of the progenitor star (the one internal to the Helium and the Hydrogen layers) is dominated by the kinetic energy, while the most external part shows a balancing between internal and kinetic energy (figure 4.8). After the shock breakout, a great amount of radiative energy is lost from the surface and this causes a reduction of the photometric radius, which lowers the luminosity. The high value of the bolometric luminosity at its peak is kept only for a short time because the expansion brings to a rapid cooling of the
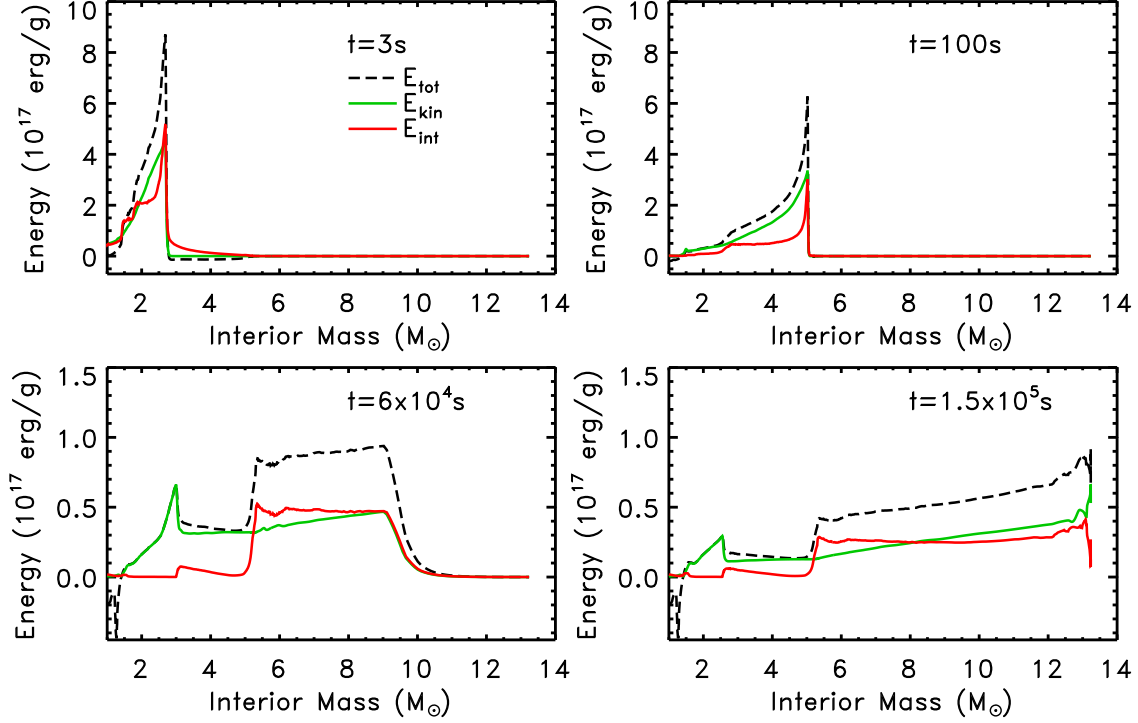
Figure 4.8: Inner profiles of the total energy (black dashed line), kinetic energy (green line) and internal energy (red line) at various times during the explosion

external layers which lowers the temperature and therefore the luminosity. In general [73], the shock breakout stage ends when the bolometric luminosity decreases by about one dex from its maximum. Then the adiabatic cooling phase begins. Figure 4.10 shows the LC obtained for the model 15A.

4.1.2 The adiabatic cooling phase and homologus expansion

Because of the ionization, the gas tends to became less transparent: the radiation is scattered due to the great number of free electrons released by the ionization, and the layers of the star become optically thick. After the passage of the shock wave the layers of matter near the photosphere are subject to an outward acceleration and consequently a cooling phase due to the adiabatic expansion is set, causing a loss of internal energy. The adiabaticity of the losses is demonstrated in figure 4.12 where it is shown the dominant role played by the mechanical expansion respect to the
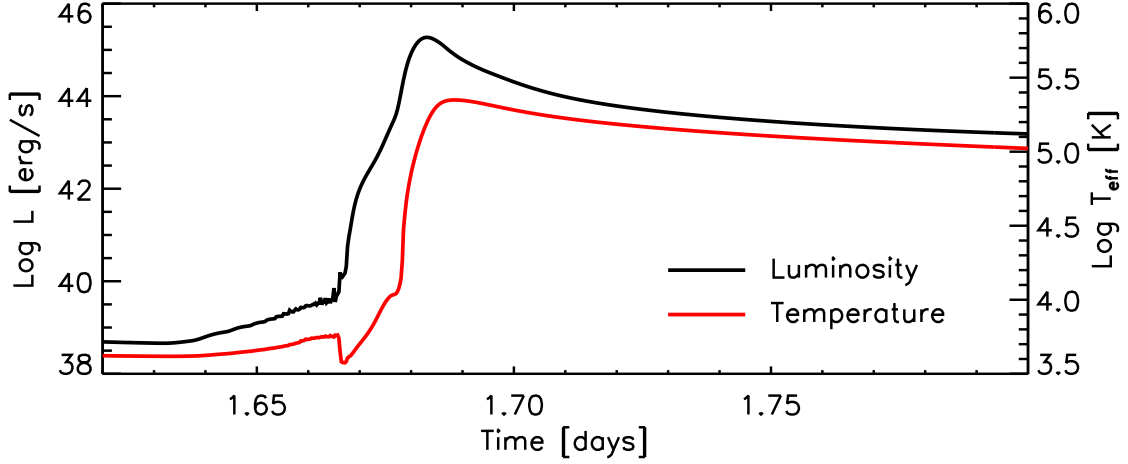
Figure 4.9: Evolution of the bolometric luminosity and effective temperature of 15A with 1 foe of energy during the breakout

the radiative losses. This adiabatic expansion lasts until all the layers reach their terminal velocity (in the examined case in about 18 days as seen in figure 4.11).

We can talk about terminal velocity because, after 18 days, the contributions given by the gradient of pressure and by the gravitational attraction of the stellar remnant have a negligible influence on the ejecta: in this way they reach an homologous expansion regime where the velocity of each layer is almost constant, and this value of the velocity only depends by the initial radius of each layer. This regime, indeed, is first reached by the most external layers and then it is reached by the internal ones due to the effects of the reverse shock wave which reaches the bottom of the expanding envelope in about 10 days and also because the most internal layers, due to their initial position, require more time to ignore the contributions of gravitational attraction. In this phase all the internal energy is almost converted to kinetic energy. During the adiabatic cooling phase the luminosity decreases because in a radiation dominated gas expanding adiabatically $\dot{E} \simeq -P\dot{V}$ implies that $T \propto 1/r$, therefore $L \propto 1/r^2$ (remembering the link between luminosity, temperature and radius $L = 4\pi\sigma R^2 T^4$ where σ is the Stefan-Boltzmann constant).

This cooling phase, corresponding to a decrease of the bolometric luminosity, lasts until the temperature decreases in such a way that it allows the partial recombination
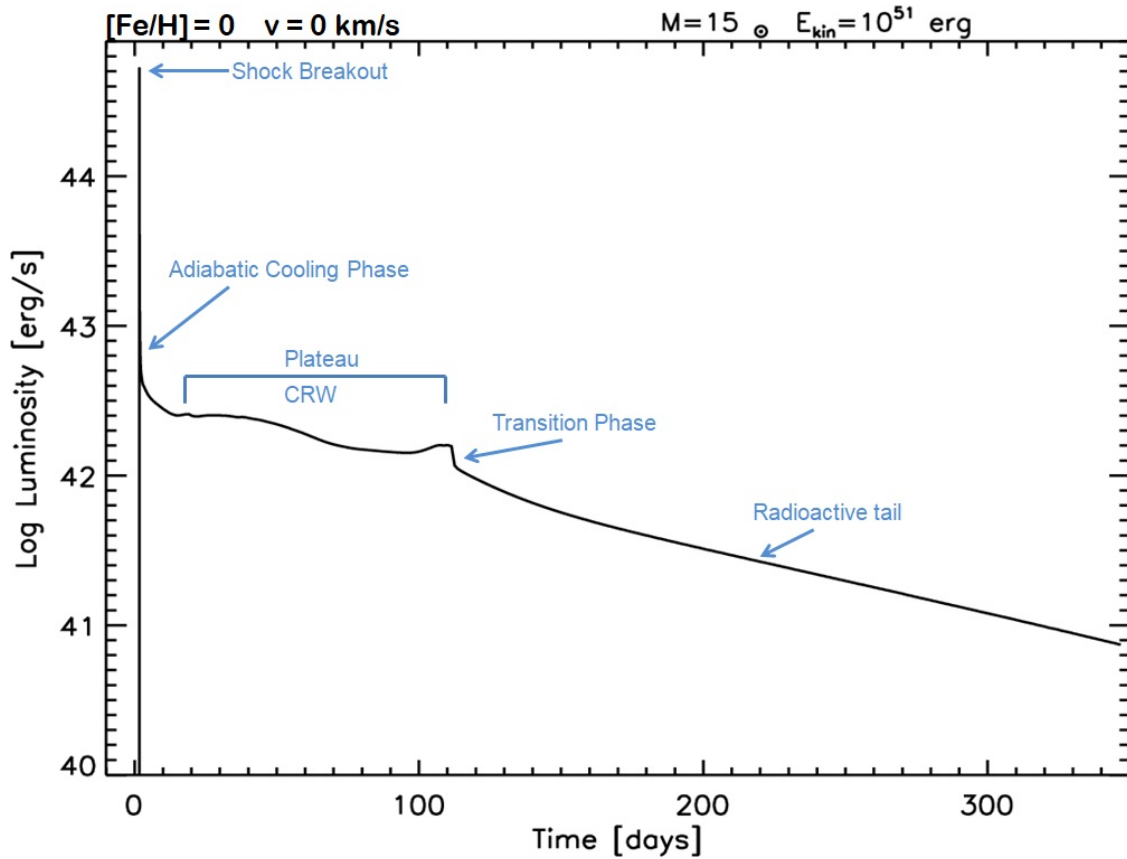
Figure 4.10: LC obtained from 15A with 1 foe of energy given, followed for 350 days

of the ionized gas.

4.1.3 Recombination wave, plateau and exhausion of radiative energy

After the adiabatic cooling phase, the bolometric luminosity remains almost constant for 100 days: this forms a sort of plateau in the LC (figure 4.10) which is only found in type II-P CCSNe. The onset of this phase is due to the fact that, after about 18 days, the temperature of the envelope decreases below $10^4 K$, hence the recombination of the ionized Hydrogen gas is allowed. This phenomenon can be seen as a sort of recombination wave, which is originated in the most external parts of the ejecta and proceeds toward the inner ones. This recombination wave has a deep impact on
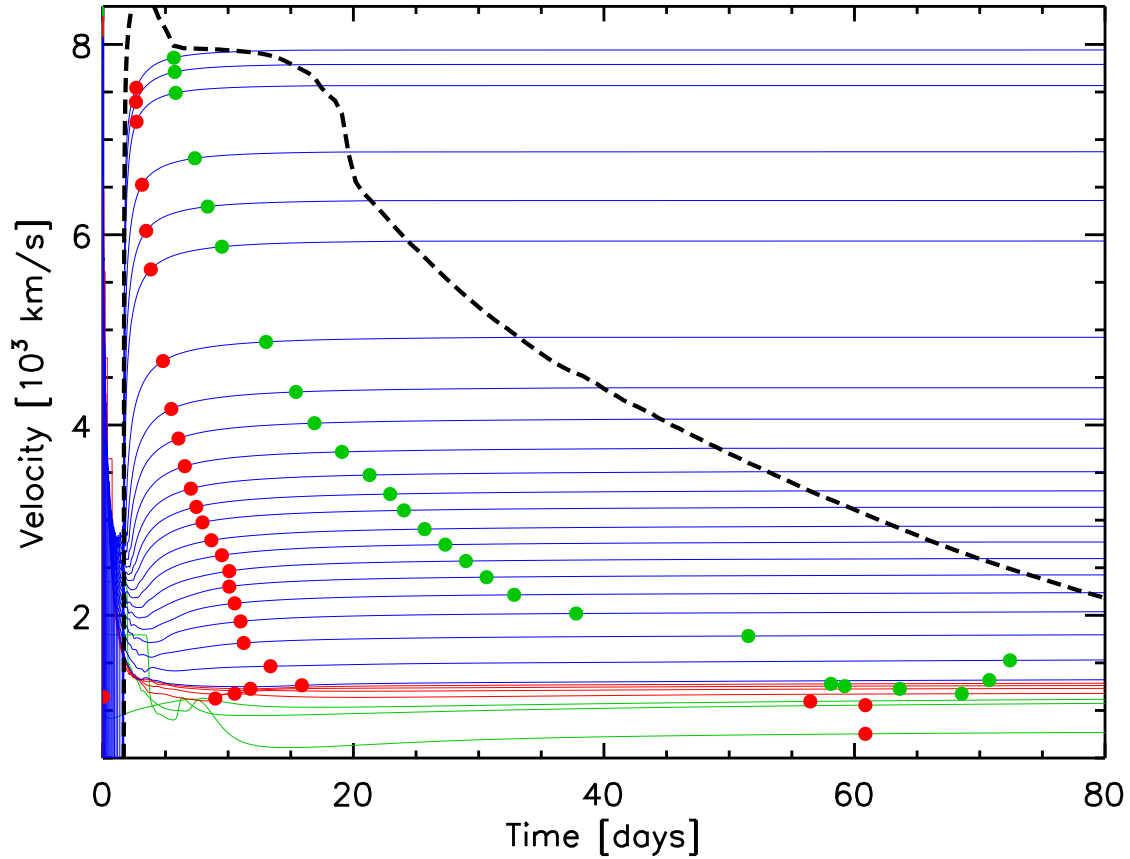
Figure 4.11: Evolution of the velocity of selected layers with time. The red and green filled dots mark the times when the layer reaches 95% and 99% of its terminal velocity, respectively. The blue, red and green lines mark the H-rich, He-rich and Carbon-Oxygen-rich layers, respectively. The black dashed line is to the velocity of the photosphere.

determining the features of the LC because the major contribution to the radiative processes is given by electron scattering 4.13: the progressive recombination reduces the total number of free electrons while the transparency of the gas rises. In this way the radiation will be more hardly scattered due to lesser number of free electrons, and this implies that the internal energy could be radiated away easily, being no longer efficiently trapped in the external envelopes.
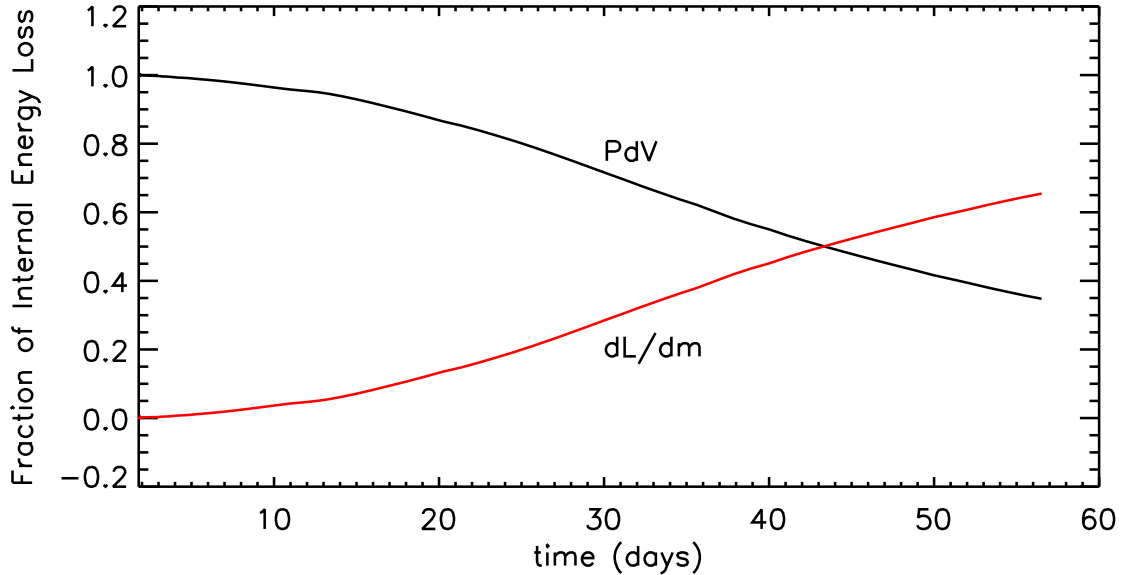
Figure 4.12: Fraction of internal energy loss due to adiabatic cooling ($P\dot{V}/\dot{E}$), black line, and radiative losses ($\partial L/\partial m/\dot{E}$), red line.

The layers are progressively cooled by their expansion, and, as the temperature drops below $5500K$, the Hydrogen tends to recombine and opacity drops (figure 4.14).

As a consequence of the decrease of opacity, also the optical depth τ decreases: if we define the position of the photosphere as the first layer where $\tau = 2/3$, we assist to a recession of the photosphere inward in mass. In first approximation, we can consider the position of photosphere and recombination wave to be coincident in mass. Due to the recombination of the atoms, the quantity of energy trapped in the ionized layers below is exposed and thus free to radiate compensating the whole loss of energy due to radiation and cooling; in this way the temperature for both gas and radiation are nearly constant in the proximity of the photospheric position. This gives the typical plateau shape to the LC, which is one of the most peculiar feature for SN II-P as it is shown in figures 4.10 and 4.15.

It is important to note how in the Hydrogen-rich envelope, the opacity is always very high: below the recombination wave, where the Hydrogen is fully ionized, it
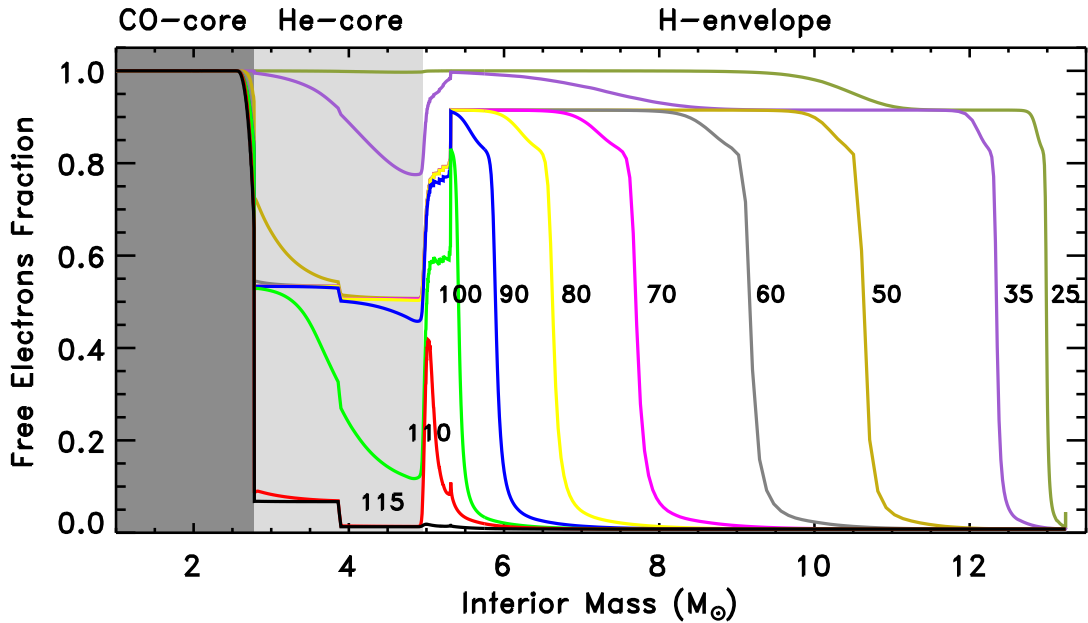
Figure 4.13: Free electrons fraction as a function of the interior mass at various times (shown in days close to the various lines). The dark and light grey areas mark the Carbon-Oxygen core and Helium core respectively. The numbers stand for the days passed since the start of the explosion

forms an opacity wall against the radiation from the layers behind. This occurs because the fraction of free electrons remains high (0.9 as shown in 4.13) even at low temperatures i.e. at the recombination of the Helium. In this way the opacity of these zones results high (see the difference between the lines at 90 and 110 days in figure 4.13) until the complete ionization of the Hydrogen. In the Helium-rich layers, the recombination begins after about 35 days from the explosion and is completed within 100 days (figure 4.13). The energy coming from the Helium-rich layers reaches the edge between Helium and Hydrogen envelopes where it encounters the free electron wall from the Hydrogen above and can not freely radiate. As a consequence a sort of accumulation, as a tank of internal energy, is set in the zone between these two layer. This extra energy is responsible for the knee found at the end of the plateau phase which is not present in the observations of CCSNe II-P (figure 4.10 and, more in detail, figure 4.18). At about 112 days the photosphere reaches the border between Hydrogen and Helium and then, due to the very low values of the opacity, it reaches
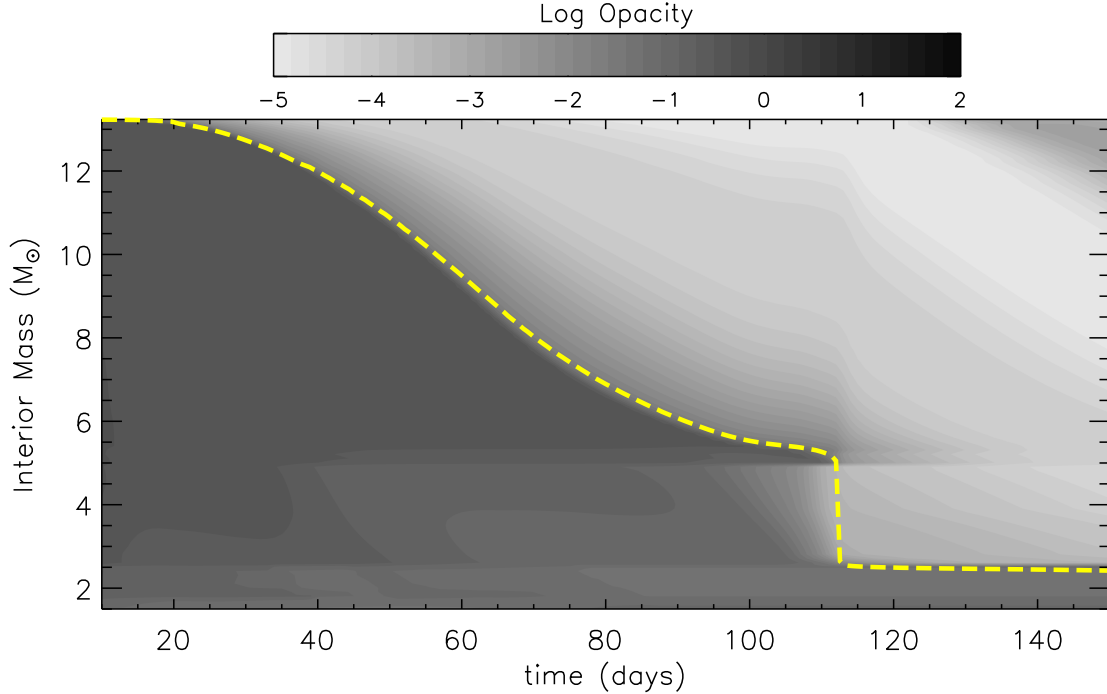
Figure 4.14: Opacity as a function of the time (x-axis) and the interior mass (y-axis) according to the color coding reported in the color bar on top the plot. The yellow dashed line marks the location of the photosphere

the Carbon-Oxygen core in about 1 day. Reaching the Carbon-Oxygen core means that the heavy elements generated during the explosive nucleosynthesis are exposed. In the Carbon-Oxygen core the fraction of free electrons is equal to 1 (metals are considered fully ionized).

At about 70 days from the onset of the explosion the contribution from the nuclear decays begins to be not negligible respect to the energy carried by the shock wave: this is shown in figure 4.16. From this moment on the shape of the LC is heavily influenced by the nuclear decay energy.

4.1.4 The tail of the LC

After about 100 days the energy coming from the recombination process ceases. As already mentioned at about 70 days the energy from nuclear decays becomes non
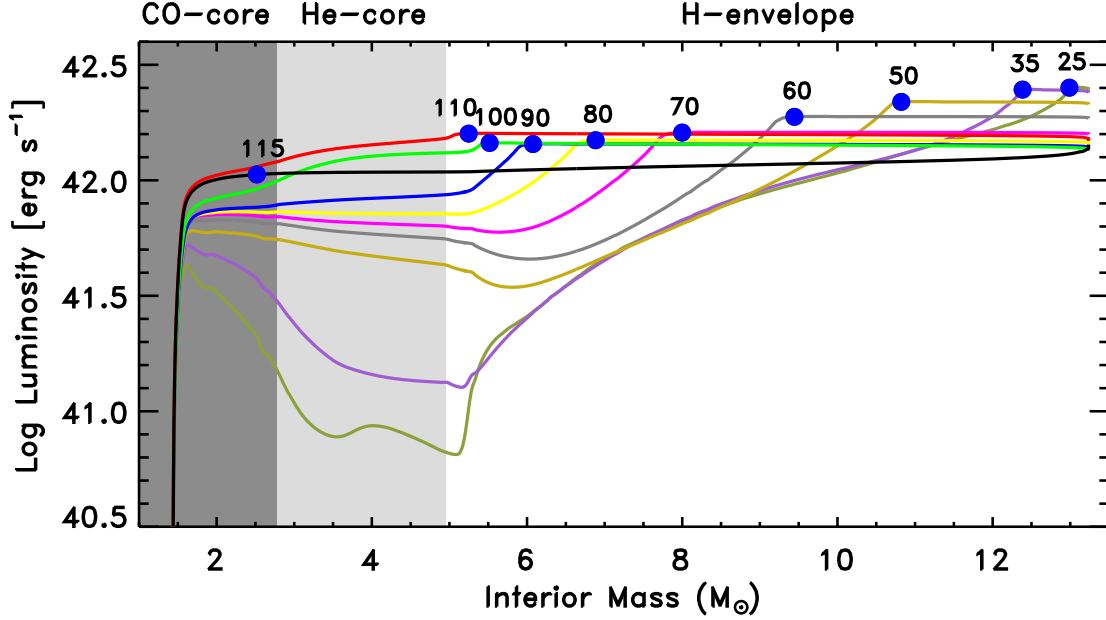
Figure 4.15: Luminosity as a function of the interior mass at various times (shown in days close to the various lines). The blue filled dots mark the mass location of the atmosphere. The dark and light grey areas mark the Carbon-Oxygen core and Helium core respectively

negligible: this is show in figure 4.16. As explained in the introduction, the major contributions from the nuclear decay energy comes from ^{56}Ni nuclear decay: this isotope has a chain reactions of electron capture decays $^{56}Ni \rightarrow^{56} Co + \gamma + \nu$ (decay time about 6 days) and then $^{56}Co \rightarrow^{56} Fe + \gamma + \nu$ (decay time about 77 days), even if the decay of ^{56}Co could be due to positron decay (β^+) as $^{56}Co \rightarrow^{56} Fe + e^+ + \gamma + \nu$, but it this decay is less likely (in 100 decays 81 are electron captures, 19 are β^+ [50]). These reactions release a huge quantity of γ-rays diffused into the the envelope which is not completely transparent to this radiation: in this way the energy from γ-rays is released not only where it is generated but also in the rest of the ejecta. It is trivial to note how the greatest part of energy released in this phase comes from the decay from ^{56}Co to ^{56}Fe due to the major lifetime; the energy from ^{56}Ni to ^{56}Co decay is released during the plateau phase and it is exhausted long before the LC could show its radioactive tail. This is the last stage of the LC and there are no new further processes able to sustain the bolometric luminosity. In this way, after several months
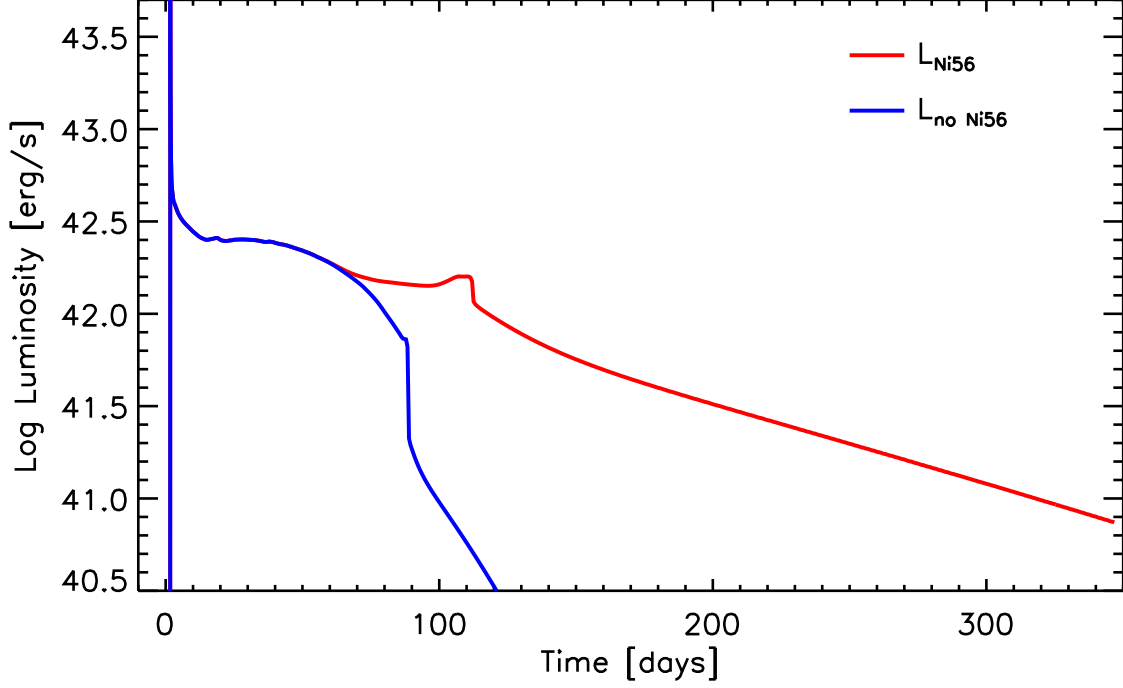
Figure 4.16: Comparison between the reference light curve (red line) and the one obtained by setting artificially to zero the abundance of ^{56}Ni (blue line) both from the same model 15A.

since the initial onset of the explosion the bolometric LC slowly fades to low values and then disappears. What is left behind from the explosion is a huge amount of processed inter stellar matter thrown away from the explosion and a cooling compact object.

4.2 Parameters and LCs

The shape of the LC is related to the features of the progenitor star (which we will investigate in the next paragraph) and to the efficiency of the mixing in some quantity in particular density, chemical composition and ^{56}Ni distribution. As a general rule the more we extend the mixing in density and chemical composition into the stellar structure, the more the LC would be smooth in particular in the transition phase between the plateau and the part of the LC heated by the radioactive decay. This

difference is show in the figure 4.17 where is reported a comparison between a LC with and without mixing.

A more complex and intriguing problem is the mixing of the ^{56}Ni: since it is also a source of energy for the LC, its mixing has an important and direct impact not only on the shape of the radioactive tail, but also the plateau itself. In general it can modify the timescales of the LC. Since ^{56}Ni is synthesized in the very first moments since the explosion and it resides in the most inner layers near the Carbon-Oxygen core, usually some phenomena (as the Raylegh-Taylor instabilities or even the action of the shock wave itself) may cause the trespassing of ^{56}Ni to more external layers. The presence of decaying ^{56}Ni in the layers where Hydrogen or Helium are dominating causes the release of decay energy in a previous moment, increasing the quantity of energy typically available during the plateau phase. A progressive pollution of ^{56}Ni in the external layer causes (as shown in figure 4.16) the plateau to modify its shape (which is linked with the energy from nuclear decays), and an homogeneous distribution of ^{56}Ni produces a flat plateau (figure 4.17) and reduces its duration. The mixing of ^{56}Ni also modify the steepness of the transition phase and it reduces the general length of the LC because the energy from decay is already released.

4.2.1   Investigating the bump

As we said before and shown in the figure 4.18, in our simulations we found a particular knee at the end of the plateau phase. As a reminder we must say that all our models came from a stellar evolutionary code, so no *ad hoc* features have been put in our models. To investigate this feature, at first, we searched in the observational data some confirmation but a similar object has not been found so far.

Because of the absence of this feature in typical observational data, it appears to be as something coming from the numerical simulation or from the numerical method. We therefore searched a way to remove this feature keeping on using our models of presupernova progenitors. This structure is formed due to the accumulation of internal energy in the border between Helium-rich and Hydrogen rich layers due to the barrier of opacity built by free electrons from Hydrogen. This accumulation exists both for physical reasons (the properties of the elements, their reflection on the values for the opacities) and for the model itself (it is a 1D evolutionary model, thus the mixing due to 2D or 3D events are not taken in account).
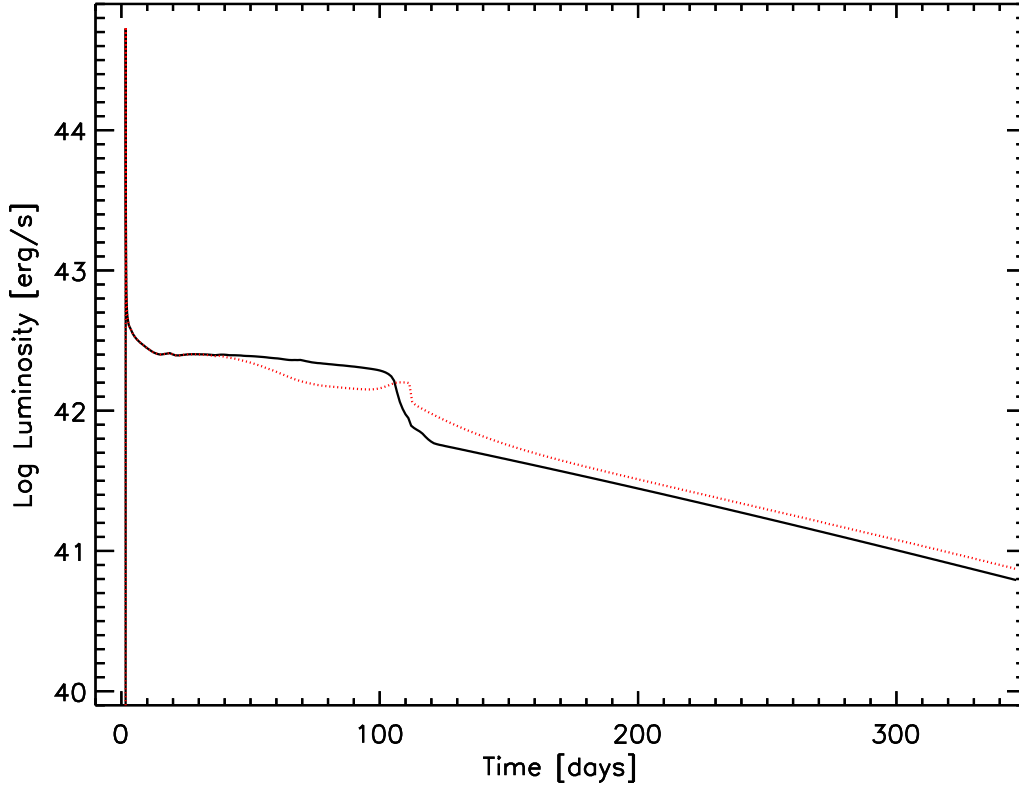
89

Figure 4.17: In black continuous line: light curve of 15A obtained using a mixing in density between the Carbon-Oxygen core and half of the Hydrogen rich-envelope, a mixing in composition from the edge of the Iron core up to the most external layer of the star and a quantity of ^{56}Ni set to $1.26 \cdot 10^{-1} M_\odot$ assumed homogeneous between the edge of the Iron core and half of the Hydrogen-rich envelope. In red dotted line: light curve of 15A without any kind of mixing and ^{56}Ni coming from the actual explosive nucleosynthesis (as in figure 4.10)

We understood that the problem could be in the distribution of some quantities, in particular the density and the chemical composition: we have observational data for 3D structures while we are using numerical models in 1D. Such a difference could neglect some important features we cannot encounter using this kind of code as, for example, Rayleigh-Taylor instability or MHD evolution. We are not able to reproduce similar features in this computational environment, so we though a
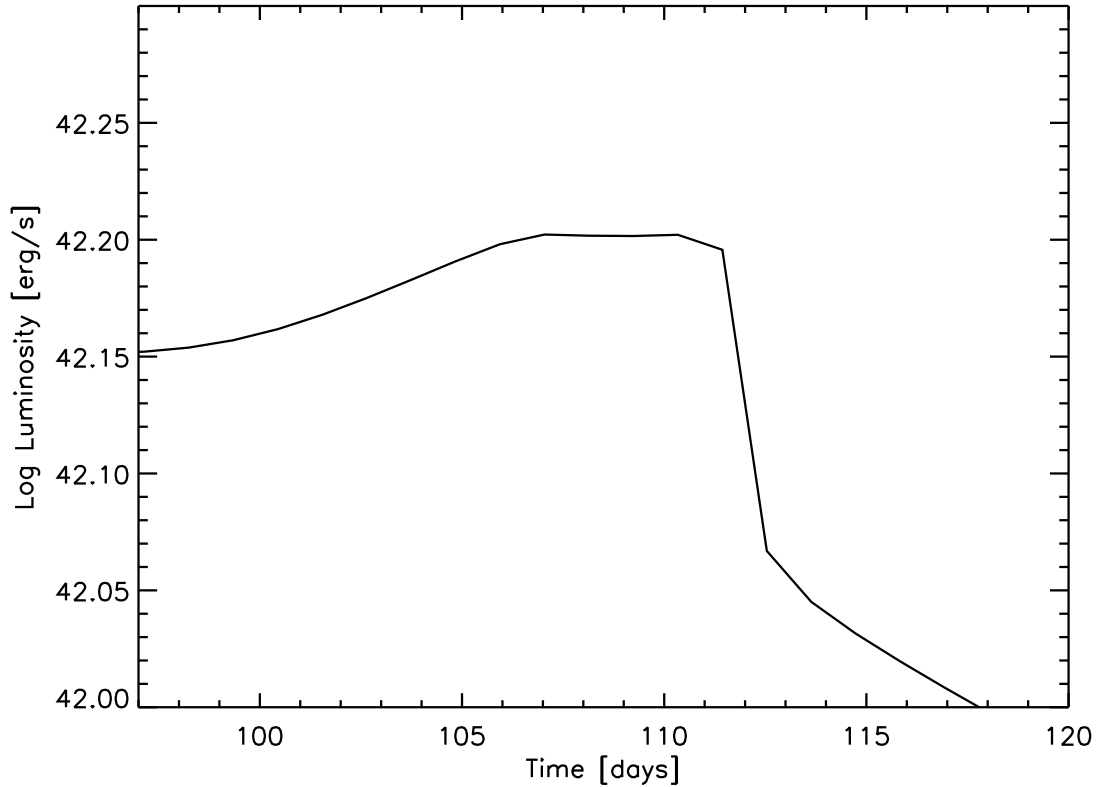
Figure 4.18: A zoom of the bump in the light curve for 15A found after about 110 days.

good way to deal with it would be giving a mixing degree (we made an average on adjacent stellar zones) to density and chemical composition to reproduce some of these multidimensional phenomena. The result (figure 4.17) is the absence of the bump and a more reliability of our results with the observations.

4.3 Dependence of LC from the stellar progenitor

The physical properties of the stellar progenitor and the explosion energy given to the model have a crucial role on shaping the LC. We studied these effects through the LCs coming from our simulations: we only considered all those star exploding as

II-P CCSNe i.e Super Giant stars with extended Hydrogen-rich envelopes.

The first parameter studied is the progenitor mass: we considered the same values for the explosion energy and the metallicity and only varied the masses of the star. In figure 4.19 we show the results of this analysis.
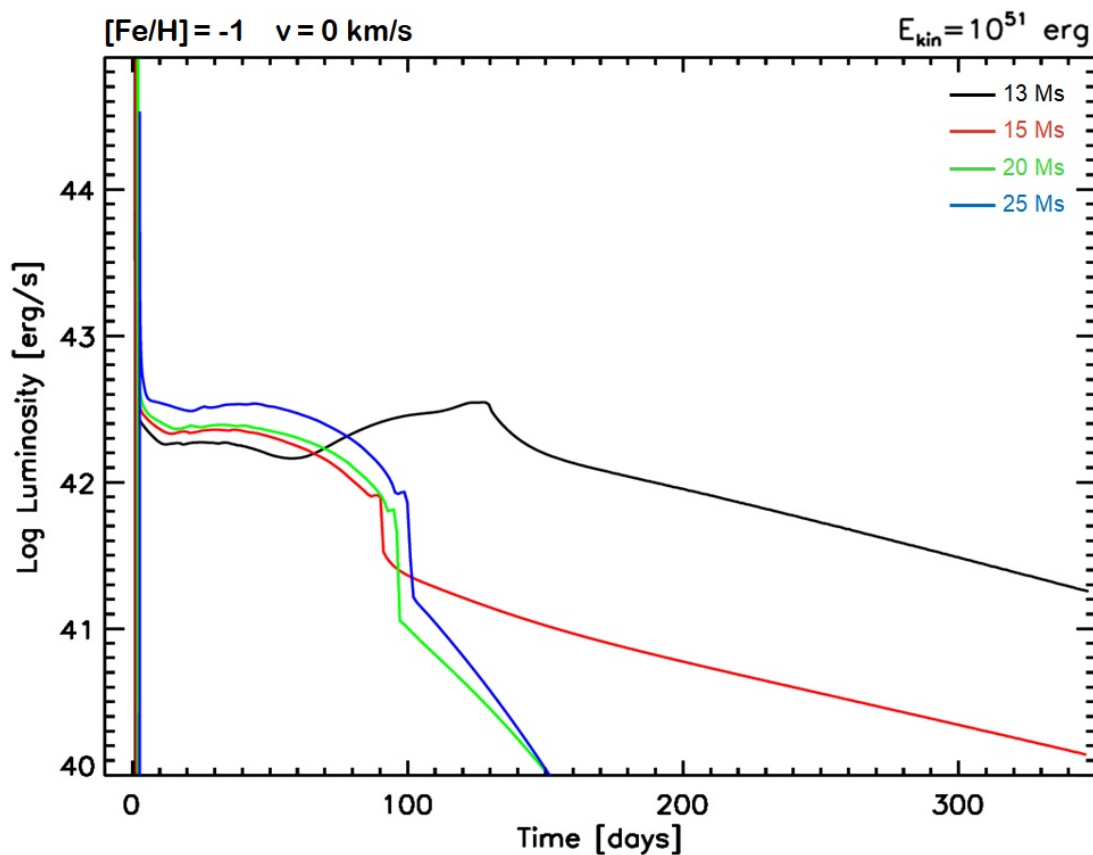

Figure 4.19: Light curves of 13, 15, 20 and 25 $M_\odot$ at the same values of initial rotation velocity (0 km/s), metallicity ([Fe/H]=-1) with an explosion energy of 1 foe. Such an high value of the explosion energy allows the 13 $M_\odot$ star to eject all the ^{56}Ni synthesized during the explosion: this is why the tail of the LC results over luminous and presenting a not realistic shape

The most immediate feature to note in 4.19 is the difference in the last parts of the LC: the radioactive tail is heavily influenced by the quantity of ^{56}Ni not involved in the fallback process. In the most massive progenitors (at the same amount of energy) an increasing fraction of ^{56}Ni is caught by the remnant, consequently ^{56}Ni cannot release its energy and it has a lower impact on the shape of tail. A second important feature concerns the luminosity and the time lasting of the plateau: for more massive progenitors the plateau seems to be more luminous and long lasting. The physical explanation of this feature is that massive progenitors usually show a larger radius: in this way the shock wave, traveling through the progenitor, finds an already puffier structure and loses less energy by PdV work to expanding an already expanded envelope. In this way a part of the energy could be used to heat and increase the temperature of the envelope (becoming more luminous) and it will take more time to become colder up to the recombination temperature (the plateau will last more). The other interesting feature (but not so easy to note) is the time of breakout: this is a direct consequence of what we explained some lines ago. For massive progenitors the photosphere will be more distant from the edge of the Iron core, thus, at the same explosion energy, the shock wave will take more time to reach that surface showing the peak at later times. Compatible results have been found in [77].

A similar analysis can be done considering models with the same mass and explosion energy and vary the metallicity. The results are reported in figure 4.20.

The metallicity has a relevant role both in the first and in the tail of a LC. In the first part of the LC the most evident differences reside, again, in the luminosity and duration of the plateau. The reasons behind this behaviour are similar to the previous point: an high value of metallicity reflects in a less compact object and therefore a more extended structure. We can apply the same consideration as before: more extended structures cause a saving in the total amount of energy used to expand the structure, and this saved amount of energy can be released as internal energy in the ejecta, increasing their temperature. The differences in the tail of the LC due to metallicity are related to the quantity of ^{56}Ni formed during the explosion and its quantity present in the ejecta. Even if low metallicity progenitors show larger ejecta respect to high metallicity progenitors, in these cases the quantity of ^{56}Ni in the ejecta is more abundant: usually reflects in higher tails of the plateau. In addition to this the quantity of ^{56}Ni formed during the explosive nucleosynthesis seems to be greater in high metallicity progenitors. We must also specify that the masses of the remnants do not scale directly with metallicity: our request for the ejecta to show an energy of 1 foe at the infinite does not allow the onset of a linear scale for the
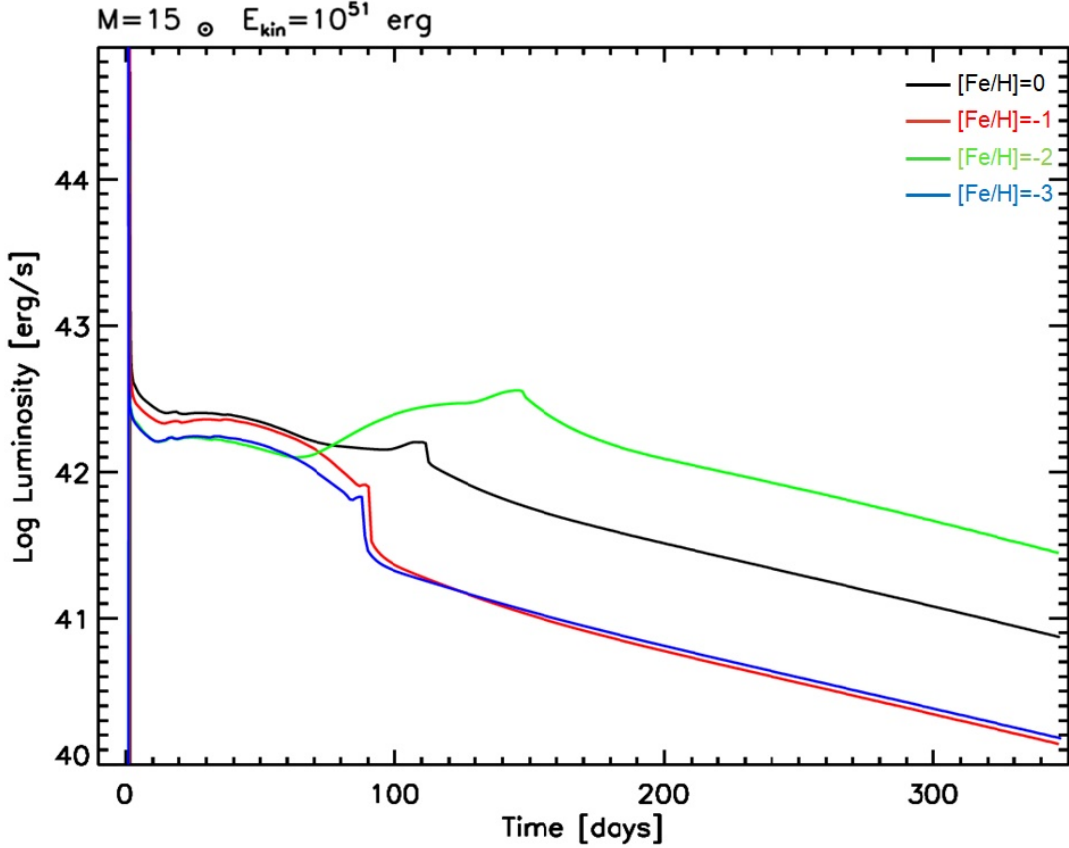
93

Figure 4.20: Light curves of a model with 15 $M_\odot$ with a initial rotation velocity of 0 km/s an explosion energy of 1 foe at 4 different metallicty (from [Fe/H]=0 to [Fe/H]=-3). The evolutionary model at [Fe/H]=-2 metallicity shows a peculiar behaviour due to the very low Iron core mass (table 3.2): the energy injected at a mass coordinate of 0.8 $M_\odot$ allows, in this case the formation of a huge quantity of ^{56}Ni (about 4 times more than in case of solar metallicity, table 3.2) which pollutes the ejecta and greatly contributes to the shape of the LC.

remnant masses due to the inner differences of the models.

After mass of the progenitor and metallicity we can study how the LC is connected to the explosion energy. To do so we kept the same values of mass and metallicity and gave to them different energies: we show these results in figure 4.21.

From this figure 4.21 we can learn how the energy has a crucial role also in the
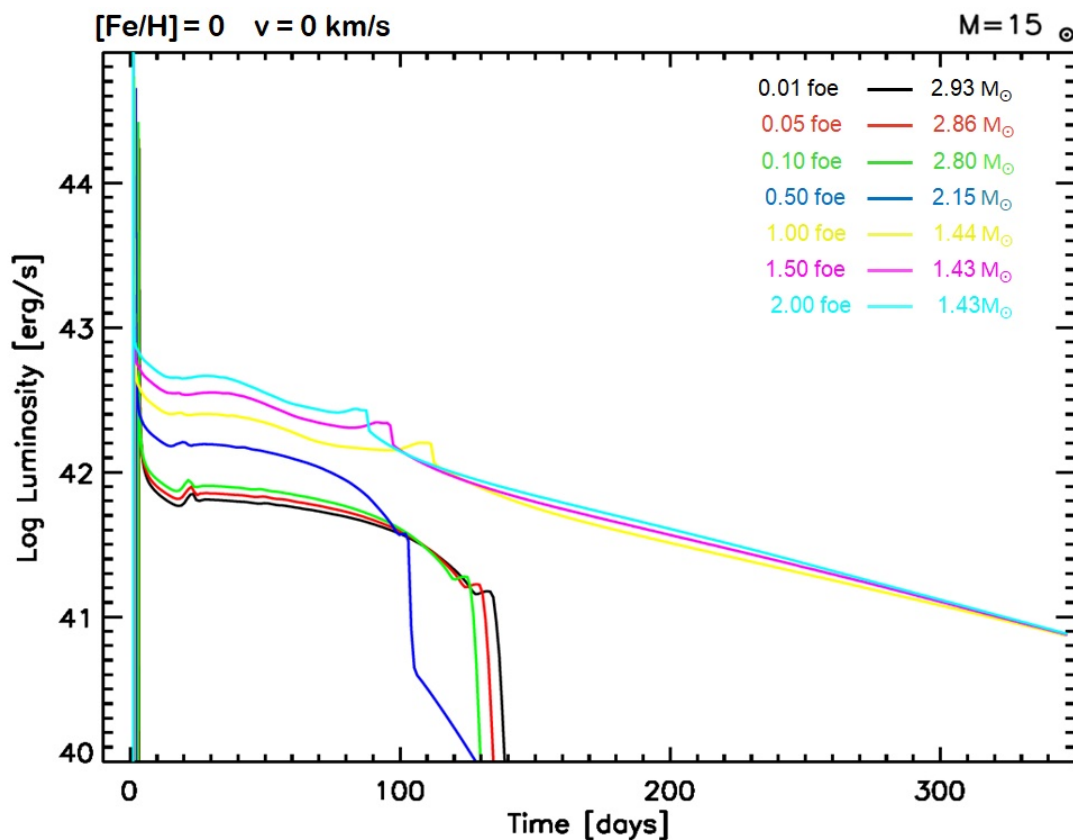
Figure 4.21: Light curves of a 15 $M_\odot$, [Fe/H]=0 model with an initial rotation velocity of 0 km/s at 7 different energies. The small differences in the plots are due to the saturation: small variations of the explosion energies cause only lesser changes in the kinetic energy of the ejecta. There is also a saturation for high explosion energies: all the mantle have been expelled and only small differences can be seen in the tail of the LC.

description of the LCs other than in the determination of SRs. First of all it has an heavy impact on the tail of the LC and this is a direct consequence of its link with the fallback: high explosion energies limit the action of the fallback, while low explosion energies tend to favour the fallback with all the associated consequences on the distribution of ^{56}Ni. This behaviour is clearly seen in the figure 4.21 where the LCs with a lower energy of the explosion show no radioactive tails at all. The other important change rely on the plateau: the higher the explosion energy, the brighter

and shorter the plateau. The greater luminosity derives from the major availability of the energy and thus could be released to increase the internal energy in the ejecta. About the effects on the duration of the plateau, a high explosion energy implies a high velocity of the ejecta and therefore a faster cooling. This would means that the recombination would be promoted and it would exercise its action in shorter times. Similar conclusion have also been found by [77].

Other information from 4.21 can be found by considering the masses of the remnants associated to the LCs: as the mass of the remnant grows, the quantity of ^{56}Ni in the envelope decreases and the tail of the LC loses the sustain of its luminosity. In this case (described in the figure 4.21) we can also define a threshold of 2.46 $M_\odot$ where, under this value, we do not find any trace of a radioactive tail.

4.4   Comparison with observed LCs

With the information obtained from such a great number of simulations, and by understanding how the LC is affected by the features of the stellar progenitor, a natural goal of this work could be the comparisons between the simulated and the observed LCs. The importance of a similar analysis resides in the possibility of obtaining information on the progenitor star associated to a CCSN event: such a chance would be a useful tool for further investigations or data analysis.

Since in this work we focused on II-P CCSNe, we analyzed two typical Type II-P CCSNe: the 1999em and the 2012A. We will describe our whole fitting strategy on the 1999em case then we will only present the results obtained for the 2012A case.

SN 1999em is a CCSN event happened in 1999 in the intermediate spiral galaxy NGC1637 located at $7.5Mpc$ [64]. This event have been studied very well in several articles. Some uncertainties have been rose on its distance and some different interpretations have been given ([64] itself and [38]). For our purposes we adopted the data from [19] in which the UBVRI contributions are calculated for an object with distance of $7.8^{+0.1}_{-0.9}Mpc$.

The fitting strategy we used is allowed by the great number of simulation led in this work: it naturally comes from the great number of different LCs obtained starting from a huge set of presupernova models at different explosion energies. Our fitting strategy is articulated in three different steps. In the first step we read (or

interpolate) the value of the bolometric luminosity at 50 days since the onset of the explosion (L50) from observations: this value is important because can give us information about the physical properties of the progenitor and indications about the value of the energy of the explosion. Once obtained this value, we compare it with all the values of L50 obtained from our whole set of simulations 4.22.

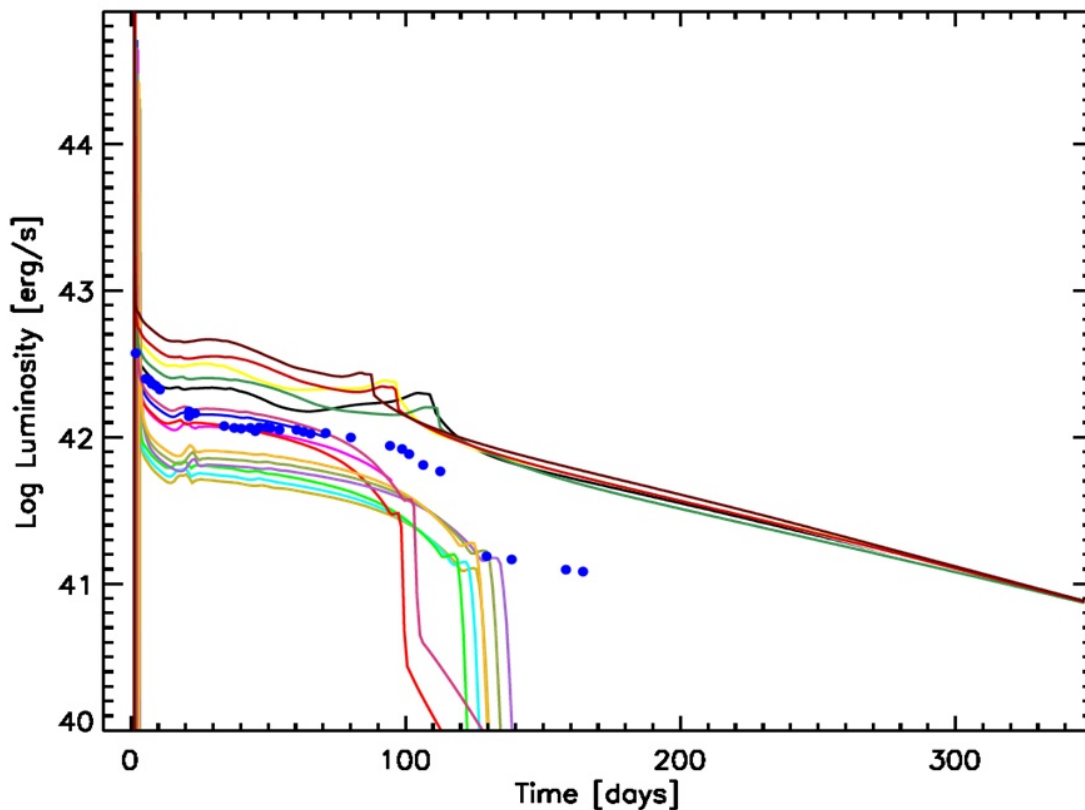Figure 4.22: Step 1 of our fitting strategy: we found the most similar LC from our simulations which matches the observed value of L50. This one will be our starting model. For clarity reasons we did not report in figure all the LCs obtained in our simulations, but are only reported the LCs of some sample models (the LCs obtained from 13 and 15 $M_\odot$ at all the usual explosion energies plus the LC obtained by $15M_\odot$ with an energy of 0.30 foe), just to give a more precise idea of the process. The dots are the data taken from [19]

97

The most similar model (at L50) will be the starting point for our fitting strategy: we can also modify the explosion energy in the model to reach a closer matching with the observational data. The second passage is to match the radioactive tail: we take the quantity of ^{56}Ni obtained naturally in the simulation and we mix this quantity (after the $2.5 \cdot 10^4 s$) in an homogeneous way in the system up to reach the same steepness of the radioactive tail obtained by data. This is shown in figure 4.23.
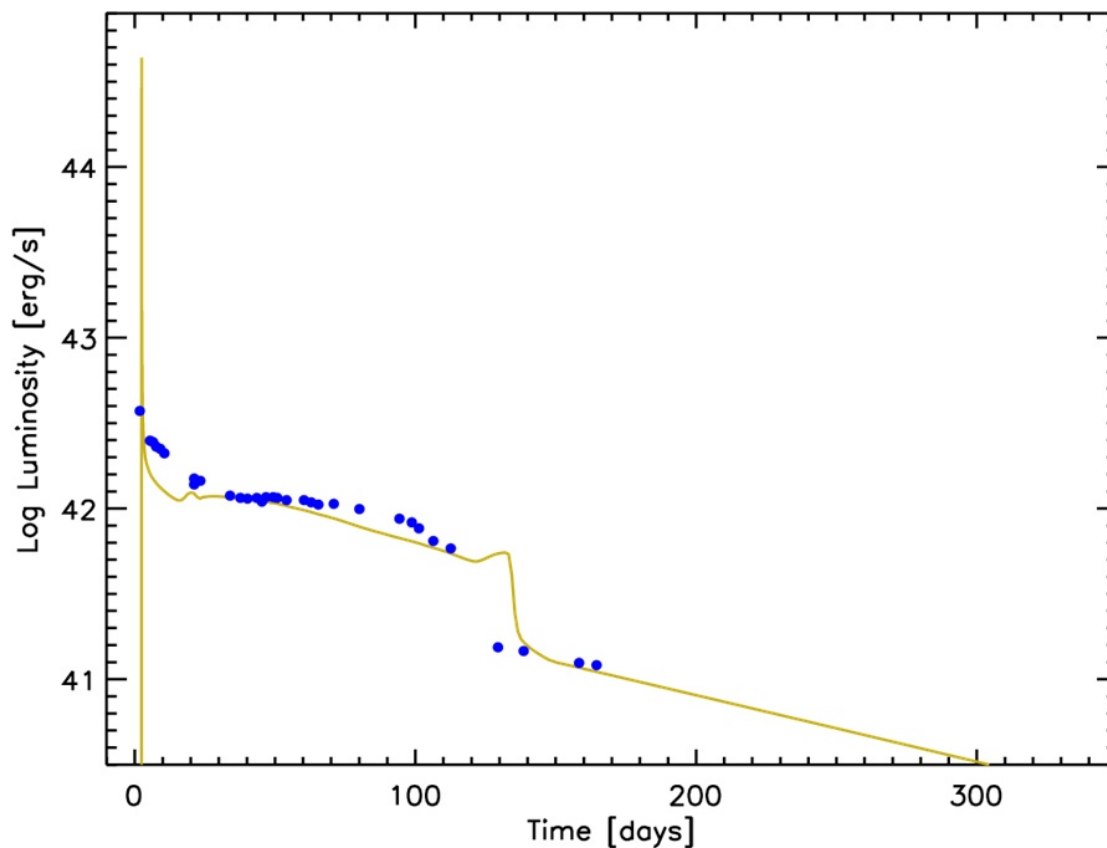

Figure 4.23: Step 2 of our fitting strategy: the quantity of ^{56}Ni is mixed in the ejecta up to obtain the same configuration of the data. The dots are the data taken from [19]

This should not be interpreted as an act of strength to force the matching: we must remember that we are simulating a 3D phenomenon with a 1D code, and some mixing features are unobtainable in a similar configuration, and this passage should mimic these phenomena. The last step consists in mixing the density of our model

both to smooth some computational features (as the bump) of the LC but also to mimic a 3D explosion and match the point of data in the transition phase between the plateau and the radioactive tail. We report the final result in figure 4.24.
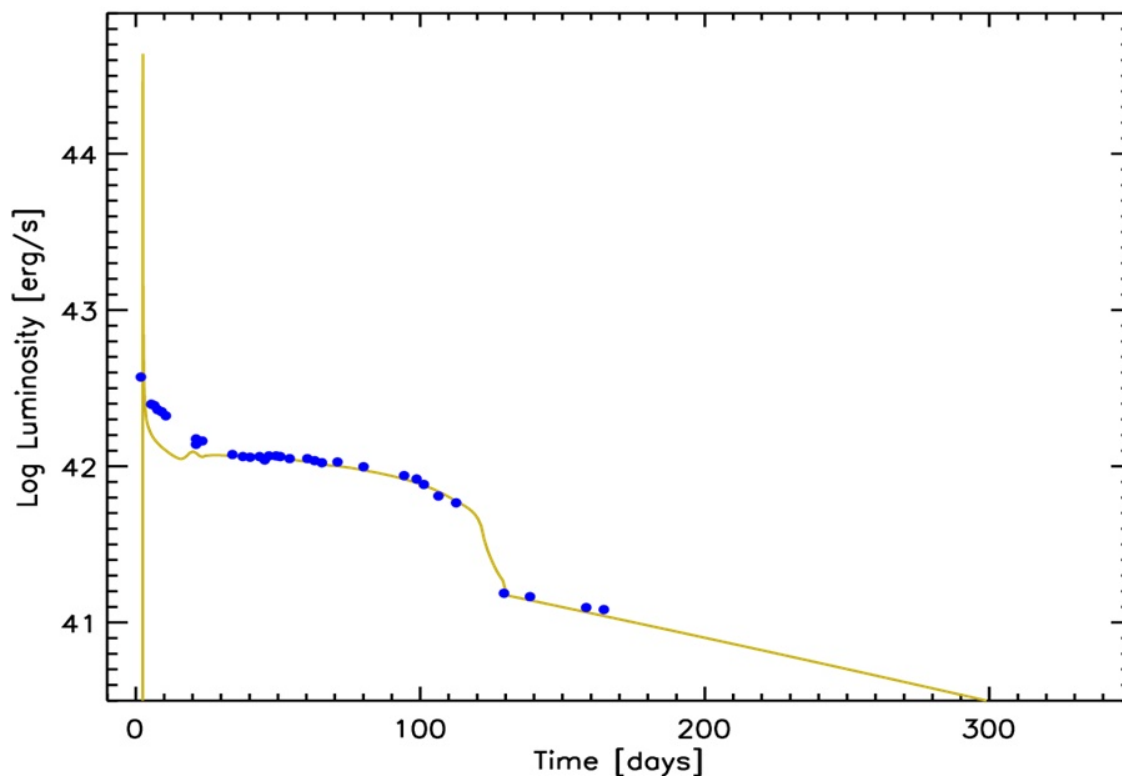

Figure 4.24: Step 3 of our fitting strategy: we smooth the transition phase by mixing the density of the model. This can be considered our final result. The dots are the data taken from [19]

With this fitting strategy we can make some predictions about the PSNP: we found that this LC could be reproduced by a progenitor with a mass, at the moment of the explosion, of $M_{expl} = 13.23 M_{\odot}$ (ZAMS mass $15 M_{\odot}$) with metallicity [Fe/H]=0 and velocity $v = 0 km/s$, a mass of the ejecta of $M_{Ej} = 10.64 M_{\odot}$, an explosion energy of $E = 0.30 foe$ and a mass of ^{56}Ni ejected of $M_{Ni} = 0.03 M_{\odot}$. We mixed ^{56}Ni and the density composition in ranges, respectively, of $2.59 - 10.00 M_{\odot}$ and $3.19 - 10.00 M_{\odot}$.

These results have been also compared with an independent method. This method is based on finding survey images of the zone around the CCSN before the

99

CCSN happened, if available. If these images are available, the stellar progenitor is searched and, assuming a distance module and the data for the apparent magnitude, it is possible to calculate the luminosity of the progenitor. This luminosity, which is assumed to be the one at the presupernova stage, is compared with the ones obtained using theoretical evolutionary tracks for stellar progenitors at different ZAMS. Then is taken, as the progenitor of that CCSN event, the star which shows the value of luminosity most similar to the one calculated from the surveys. This method has been used by Leonard and Kanbur (2003) [38] onto the 1999em founding results compatible with the ones obtained by our comparison: in particular they found an upper limit value for the progenitor mass of the 1999em as $15^{+5}_{-3}\,M_{\odot}$.

Another option to check the results obtained in this comparison, is to bypass the evolutionary tracks and to compare the values for luminosity obtained for the progenitor. Using this approach, Davies and Beasor (2018) [16] found an upper value for the luminosity of the progenitor of the 1999em as $L/L_{\odot} \leq 5.02^{+0.06}$: the presupernova model proposed by us has a luminosity of $L/L_{\odot} = 4.98$ which is compatible with the previous value.

SN 2012A has been a typical II-P CCSN located in NGC 3239, an irregular galaxy located at $9.8\,Mpc$. We used the data from [72], and with this starting point, we used our strategy explained above to reach a match between our simulations and observational data, as it is shown in figure 4.25.

Also in this case we can infer some information about the progenitor. The LC could be coming from a star with a mass, at the moment of the explosion, of $M_{expl} = 10.28M_{\odot}$ (ZAMS mass $13M_{\odot}$) with metallicity [Fe/H]=-1 and velocity $v = 0\,km/s$, a mass of the ejecta of $M_{Ej} = 8.02M_{\odot}$, an explosion energy of $E = 0.21\,foe$ and a mass of ^{56}Ni ejected of $M_{Ni} = 0.01M_{\odot}$. We mixed ^{56}Ni and the density composition in ranges, respectively, of $2.26-10.3M_{\odot}$ and $2.26-7.5M_{\odot}$. We have two comparison for this progenitor. The first is by Tomasella and Cappellaro (2013) [72], using the survey method: they found that the upper limiting mass for the stellar progenitor should be $10.5^{+4.5}_{-2}M_{\odot}$. Our value is compatible with this result. The second comparison is give by Davies and Beasor (2018) [16] which found the constraint on luminosity to be $L/L_{\odot} = 4.57\pm0.09$. In this case our value of $L/L_{\odot} = 4.85$ is slightly out of range, but this very narrow difference could be due the setting of the evolutionary code.

We must say that the first 25-30 days of observed data can not be accurately reproduced by our simulations: this is a well known problem also found by other
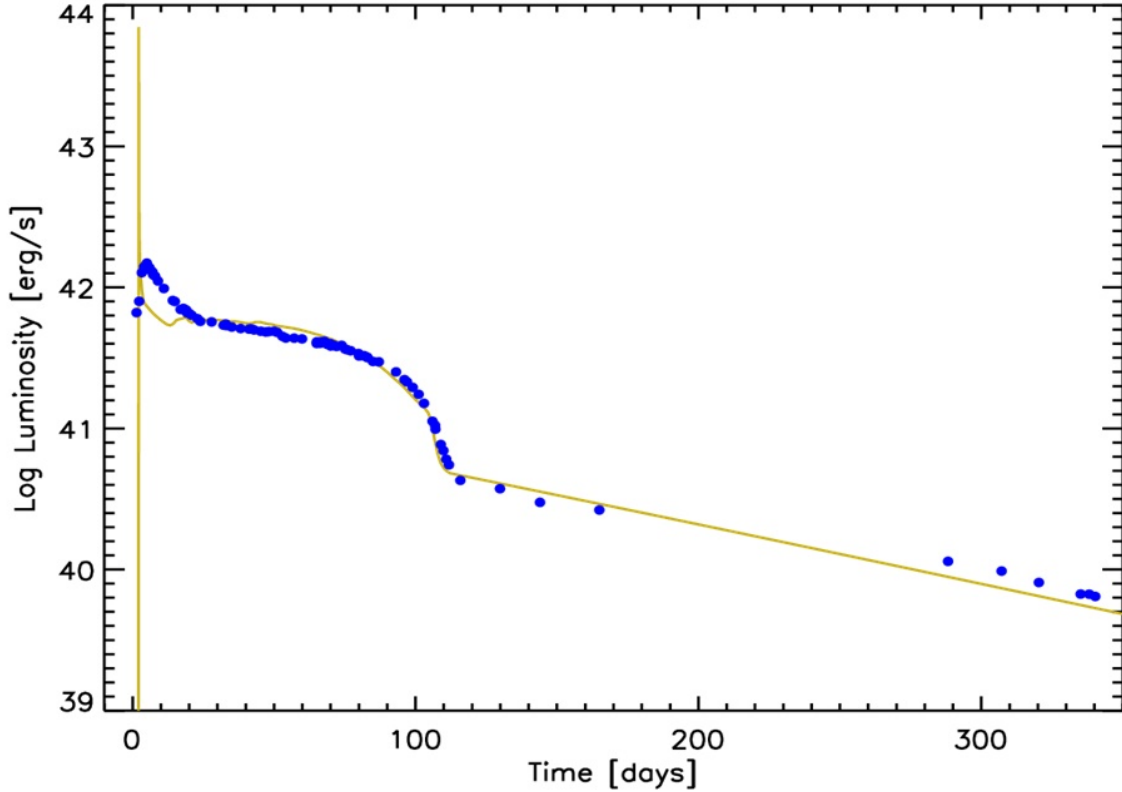
Figure 4.25: The fit obtained for SN 2012A. The dots are the data taken from [72].

authors, as [75] or [49]. The reason behind this problem [20] could be numeric and related to the resolution of the grid used around the photosphere for the times around the shock breakout, and could be related to the description of the outer layers of the presupernova model at later times [74]. In this sense we must point that the models used in this work [45] have not been specifically developed to obtain LCs but, instead, to calculate the remnant masses and explosive nucleosynthesis of massive stars.

4.5 Comparison with theoretical LCs

This paragraph is devoted to the comparison of the LC obtained with HYPERION and other theoretical LCs obtained by other authors. We used, as comparisons, the LCs obtained by Morozova and Piro [49] and by Bersten and Benvenuto [8]: we chose these two works because both the authors computed a LC using a 1D hydrodynamic

code in a flux-limiter diffusion approximation. The LCs used as comparison are both been digitized from [49], the comparison between all these results is presented in figure 4.26.
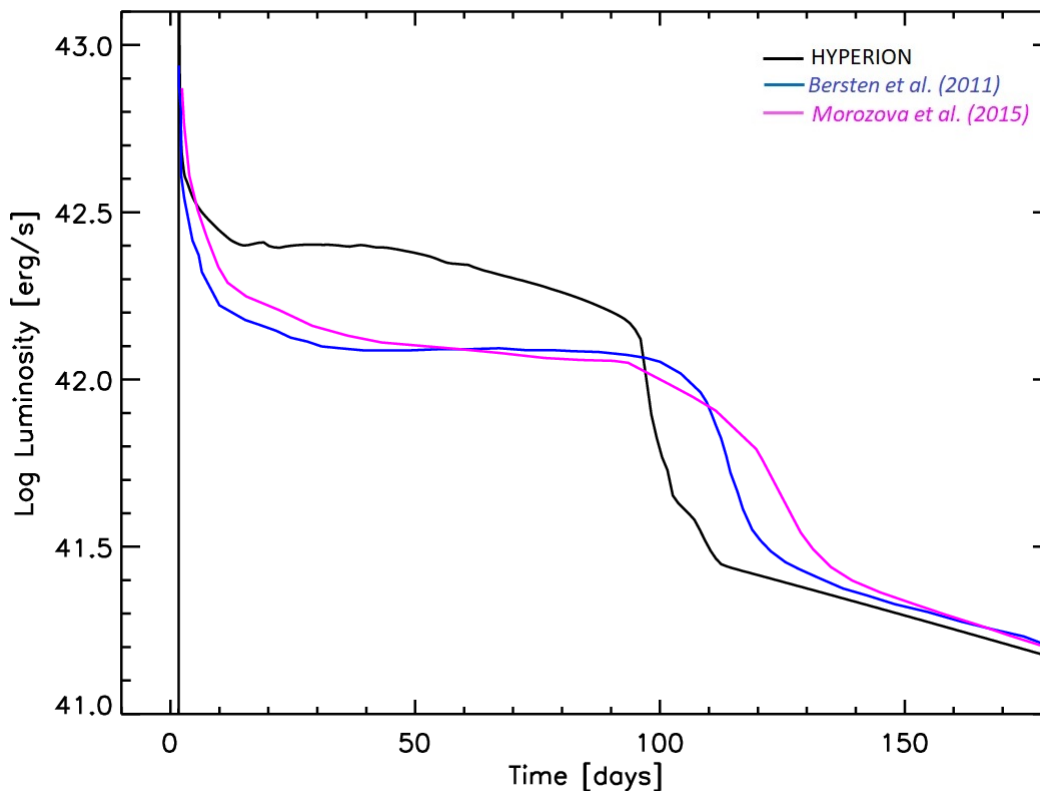

Figure 4.26: LCs obtained with three different 1D codes. The black one is obtained using HYPERION, the blue one is taken from Bersten et al. [8], while the magenta one comes from Morozova et al. [49].

The two LCs in [49] and [8], are not obtained from an evolutionary presupernova model, but they come from a double polytropic model in hydrostatic equilibrium reproducing a star with a ZAMS of $19 M_\odot$ at solar metallicity. Furthermore both [49] and [8] used a similar set of input parameters to obtain their LCs: an explosion energy of 1.25 foe, an amount of ^{56}Ni ejected of $0.056 M_\odot$ and a step function for the opacity floor. We wanted to use a similar model to reach a meaningful comparison: since our 20 $M_\odot$ at solar metallicty does not explode as a Type II-P CCSN, we used

a 15 $M_\odot$ evolutionary presupernova progenitor. As explosion energy we used 1 foe and we artificially put an amount of ^{56}Ni ejected of $0.056 M_\odot$ to match the value reached by the other two LCs.

Considering these intrinsic differences (even the two LCs obtained starting from the very same model show some odds), the LCs in exam show a similar behaviour and timescales, even if some discrepancies are found in particular in the plateau phase. We already mentioned how the radiative cooling phase can not be perfectly reproduced by our models probably due to the description of the outer layers of the presupernova model [74], but in this case our LC is more luminous respect to the other two LCs probably due to the differences in the description of these external layers. During the plateau phase our LCs results to be more luminous and shorter, these two factors can be the consequences of the explosion energy given to the model: in our case the explosion energy is lower but the progenitor is lighter (15 $M_\odot$ respect to 19 $M_\odot$) and this could bring to a little bit more luminous and shorter plateau phase. The tails of all the LCs show the same steepness at the same values of the luminosity: in the case treated with HYPERION we artificially put the same quantity of ^{56}Ni of the other two simulation to verify how the calculation of the decay nuclear energy is well treated by our code.

In general, even with some odds due to the presupernova models, the three LCs show a similar behaviour and compatible timescales, but the values of the luminosity ares slightly different in our case.

Chapter 5

Summary and Conclusions

Chapter 1 is devoted to the presentation of the objects studied in this work: the massive stars and the outcomes of their explosion as CCSNe. CCSNe are some of the most interesting events in the whole Universe and could be an important source of information and data in different branches of astrophysics and, more in general, of physics. These events represent the last moments of life of massive stars (more massive than $8 M_\odot$): in a relative short times (for the typical astrophysical timescales) a huge quantity of energy is released, thus the stellar structure is destroyed, the most external layers are thrown away in the neighborhood space while the Iron core (and some portions of the envelope) are left as stellar remnants. This explosion happens because, in its internal part, the star is no longer sustained by the pressure raised from chemical reactions and the structure collapse under its self-gravity. Due to a complex and still debated series of events, a shock wave, which heats and compresses the matter of the envelopes, is formed. During its travel, the shock wave provides the conditions for the explosive nucleosynthesis to happen. The shock wave transfers its energy to the stellar structure: in this way the envelope can gain enough speed to win the escape velocity and leave the structure, becoming ejected matter. Some of the most internal layers of the stellar structure may not reach such an high velocity value and in-fall onto the iron core increasing its mass, this is the fallback and it typically occurs in several hours. Depending on its mass, the remnant could be a neutron star or a black hole. The electromagnetic emission of a CCSN event (light curve) can be followed for several months after the explosion. Our aim is to investigate this phenomenon in a systematic way focusing on two outcomes of the explosion: the star remnants and the light curves.

In Chapter 2 we discussed the general problems behind CCSNe simulations and described the code and the numerical techniques used in this work. We explained that, to these days, there is no self consistent model which can reach an explosion in a natural and systematic way starting from evolutionary models: even the models which can reach an explosion show not realistic values of the energy able to reproduce the observed features. A complete CCSN simulation requires complex 3D simulations including MHD calculation: similar codes would take an enormous amount of time (talking about a month of computing work for a second of simulation), and, therefore, a systematic work can not be accomplished using similar codes. We opted to achieve the simulations in 1D injecting, just below the Iron core, a chosen amount of energy mimicking the insurgence of a shock wave. To this purpose, we developed, using as base a code by Limongi and Chieffi ([43]), a 1D hydrodynamic code called HYPERION which is able to follow a complete CCSN event starting from the injection of energy up to the exhaustion of the energy after several months. The initial version of the code was able to calculate the masses of the remnants and the explosive nucleosynthesis, but we added some further features to make the code also able to compute light curves: we (mainly) added a radiative transport calculation, improved the EOS, included a Saha equation for the contributions of ionization, computed a reliable calculation of the opacities, realized the tracking for the photosphere and developed a ^{56}Ni energy decay and deposition function. We used this tool on a set of diversified PSN models: these models are calculated from evolutionary simulations by Limongi and Chieffi ([45], a summary of their features in found in table 3.1 and 3.2) with different initial mass (13, 15, 20, 25, 30, 40, 60 and 80 $M_\odot$) and metallicity ([Fe/H]=0, -1, -2 and -3). Starting from these models, we simulated the CCSN events with different values of the injected energy (to reach an explosion energy of 0.01, 0.05, 0.10, 0.50, 1.00, 1.50 and 2.00 foe), and we obtained the associated light curve and remnant masses for each combination of mass, metallicity and energy injected in the model.

In Chapter 3 we studied the results obtained for the remnants. Due to the combinations of the models and the energy represent a large number of different CCSN events, we obtained a vast span of values: the least massive remnant we found is a NS of $1.08M_\odot$ corresponding to a $15M_\odot$ star with a metallicity of [Fe/H]=-2 at high explosion energies (over 1.00 foe). The most massive remnant found comes from an $80M_\odot$ star with a metallicity of [Fe/H]=-3 with a very low explosion energy (0.10 foe) and is a BH with a mass of $43.68M_\odot$. Other quantitative results of our calculations can be found in tables from 3.3 to 3.6. Using the results obtained in our simulations, we analyzed how the remnant mass is influenced by the features

of the progenitor star and by the explosion energy. We found that the mass of the remnant increases when the mass of the progenitor star grows because the binding energy is higher and thus would be harder for the layers of the progenitor star to escape from the attraction of the proto-remnant (figure 3.9). We also found that the mass of the remnant is increased when the energies injected are low (figure 3.10): this because the energy available to free the envelopes from the binding energy of the progenitor would be lower and, therefore, an a grater quantity of matter will fall onto the proto-remnant. Another feature able to modify the mass of the remnant is the metallicity (from figure 3.10 to 3.13): at low values of metallicity, the progenitor results more compact, therefore the mass of the Carbon-Oxygen core grows and the same would do the binding energy. After obtaining all the masses of the remnants from the simulations, we searched for the limiting mass of the progenitor (at each energy and metallicity) for which the remnant could not be considered a neutron star anymore and should be seen as a black hole. These results can be found in the table 3.7 and in figure 3.15. We also compared our results with the theoretical upper limit for BH (considered $80 M_\odot$), finding that no simulation gave such massive remnant. A further comparison have been done by comparing some values of remnant masses obtained using HYPERION with the ones obtained by other authors for similar progenitor masses and explosion energies. We found that the values of the remnant mass are too heavily influenced by the properties of the progenitor star and by the way of injecting the energy into the model to obtain a trustful comparison.

Chapter 4 has been devoted to the study of light curves: in this Chapter we focused only on the progenitor star exploding as Type II-P CCSNe (i.e. super giant stars with huge hydrogen-rich envelopes), the other progenitors have not been considered in the analysis. We reported some interesting values of our simulations in tables from 3.3 to 3.6. In the first part of this Chapter we used a typical II-P light curve (obtained from a $15 M_\odot$ star with solar metallicity with an explosion energy of 1.00 foe) to explain, in depth, the evolution of a CCSN event. We also investigate on the insurgence of some features as a bump at the end of the plateau phase of the LC (figure 4.10 and 4.18), which is not present in the observations. We found how this feature is related to the difference in the opacity between the Hydrogen-rich and the Helium-rich part of the envelope: at the same moment, during the plateau phase the Hydrogen-rich part show a greater number of free electrons respect to Helium-rich part (figure 4.13). In this way, the energy radiating form the Helium-rich part below the Hydrogen-rich part is trapped by this barrier of free electrons: when the photosphere reaches this border this amount of extra energy is free to radiate. We studied how the shape of the LC is influenced by the mixing in mass of density, composition and ^{56}Ni:

in general if we tend to smooth these features to huge portions of the stars, the LC will appear less edgy. With the mixing of density and chemical composition it is possible to eliminate the bump (figure 4.17). We also studied how the features of the progenitor star could influence the shape of the light curves: we found as a more expanded structure (due both to higher metallicity or mass, figures 4.20 and 4.19 respectively) tends to present a more luminous and long lasting plateau, while we found as a more energetic explosion provides a more luminous plateau but shorter in time duration (figure 4.21). With the knowledge obtained in this work, we managed to use the code and the simulations to compare some observed LCs with our outcomes and predict some information about the stellar progenitors: we decided to investigate two typical II-P LCs as the 1999em and the 2012A. Using a three parts strategy, we reached some information about the progenitors which have been also confirmed by other studies with different investigation methods. We found that 1999em can be reproduced by a progenitor with a mass, at the moment of the explosion, of $M_{expl} = 13.23M_\odot$ (ZAMS mass $15M_\odot$) with metallicity [Fe/H]=0 and velocity $v = 0km/s$, a mass of the ejecta of $M_{Ej} = 10.64M_\odot$, an explosion energy of $E = 0.30 foe$ and a mass of ^{56}Ni ejected of $M_{Ni} = 0.03M_\odot$. This result can be found in figure 4.24. Regarding 2012A we found that it can be reproduced by a progenitor star with a mass at the moment of the explosion $M_{expl} = 10.28M_\odot$ (ZAMS mass $13M_\odot$) with metallicity [Fe/H]=-1 and velocity $v = 0km/s$, a mass of the ejecta of $M_{Ej} = 8.02M_\odot$, an explosion energy of $E = 0.21 foe$ and a mass of ^{56}Ni ejected of $M_{Ni} = 0.01M_\odot$. The shape of the LC can be found in figure 4.25. We also compared the LC obtained with HYPERION with other two theoretical LCs obtained by other authors which used exactly the same presupernova model: since we could not use the same progenitor employed by the other authors, we chose the most similar one studied in this work to obtain a meaningful comparison. We found that our LCs is more luminous in the plateau phase, and the plateau itself is shorter and this could be due to the different explosion energy (in our case 1.00 foe and a 15 $M_\odot$ model, in the others 1.25 foe and a 19 $M_\odot$ model), but we found a similar behaviour in the tail of the three LCs. In general, considering the differences in the presupernova model and in the explosion energy, the LCs do not show huge disagreements.

At the end of this work, we can imagine future prospective for HYPERION. As immediate extension, this tool could be used to calculate CCSNe event for models with an initial rotation velocity. We expect that a value of the initial rotation velocity different from zero would affect our models in two ways: the first is to increase the Carbon-Oxygen core and this would cause the increasing of the masses of the remnants in general, while the other effect of the rotation would bring, in particular

for high metallicity stars, an increase of the mass loss, excising more Hydrogen-rich matter from the envelope. We can also extend the number of presupernova models to obtain further data and to refine the prediction on stellar progenitor due to our fitting strategy. We could also consider more energetic explosions: this could be interesting in particular for massive star to study even very massive remnants.

Bibliography

[1] **Abbott, B.P. et al., LIGO Scientific Collaboration, Virgo Collaboration**, 2016, PRL 116, 061102

[2] **Abbott, B.P. et al., LIGO Scientific Collaboration, Virgo Collaboration**, 2016, PRL 116, 241103

[3] **Arcavi I.**, 2017, Hadbook of Supernovae, edited by Alsabti A. and Murdin P., Springer

[4] **Arnett W. D., Bahcall J. N. et al.**, 1989, ARA&A, 27, 629

[5] **Bailyn C.D., Jain R.K.**, 1998, ApJ, 499, 367

[6] **Bersten M. C., Hamui M.**, 2009, ApJ, 701, 200

[7] **Bersten M.C.**,2010, Phd Thesis, University of Chile

[8] **Bersten M. C., Benvenuto O., et al.**, 2011, ApJ, 729, 61

[9] **Bours M. C. P., Toonen S., et al.**, 2013, A&A, 552, A24

[10] **Burrows A., Dessart L. et al.**, 2006, Phys Rept, 442, 23

[11] **Burrows A., Dessart L. et al.**, 2007, ApJ, 664, 416

[12] **Chevalier R. A., Irwin C. M.**, 2011, ApJ, 729, L6

[13] **Chieffi A., Limongi M. et al**, 1998, ApJ, 502, 737

[14] **Colella P., Woodward P. R.**, 1984, Journal of Computational Physics, 54, 174

[15] **Colgate S.A.**, 1971, ApJ, 163, 221

[16] **Davies B., Beasor E. R.**, 2018, MNRAS, 474, 2116

[17] **Demorest P.B., Penucci T. et al**, 2010, Nature, 467, 1081

[18] **Elias-Rosa N., Van Dyk S.D. et al.**, 2011, ApJ, 742, 6

[19] **Elmhamdi A., Danziger I. J., et al.**, 2003, MNRAS, 338, 939

[20] **Ensman L., Burrows A.**, 1992, ApJ, 393, 724

[21] **Farr W.M., Sravan N.**, 2010, astro-ph/1011.1495

[22] **Ferguson J. W., Alexander D. R.**, 2005, ApJ, 623, 585

[23] **Fesen R. A., Shull M. J., et al.**, 1997, Astron. J., 113, 354

[24] **Filippenko A. V.**, 1988, Astronomical Society of Australia, 7, 540

[25] **Filippenko A. V.**, 1997, ARAA, 35, 309

[26] **Fryer C.L**, 2009, ApJ, 699, 409

[27] **Fryer C. L., Andrews S., et al.**, 2018, ApJ, 856, 63

[28] **Gal-Yam A., Leonard D.C. et al.**, 2007, ApJ, 656, 372

[29] **Gal-Yam A. et al.**, 2009, Nature, 462, 624

[30] **Gal-Yam A**, 2012, Nature, 337, 927

[31] **Grefenstette B.W., Harrison F.A. et al**, 2014, Nature, 506, 339

[32] **Grogin N. A., kocevski D. D. et al.**, 2011, ApJS, 197, 35

[33] **Hamui M., Pinto P. A.**, 2002, ApJL, 566, L2

[34] **Heger A, Fryer C.L. et al**, 2003, ApJ, 591, 288

[35] **Iglesias C. A., Rogers F. J.**, 1996, ApJ, 464, 943

[36] **Kippenhahn R., Weigert A.**, 1994, Stellar Structure and Evolution, ed. Springer-Verlag

[37] **Lattimier J. M.**, 2012, ARNPS, 62, 485

[38] **Leonard D. C., Kanbur S. M., et al.**, 2003, ApJ, 594, 247

[39] **Leonard D.C., Filippenko A.V. et al**, 2006, Nature, 440, 505

[40] **Li W., Leaman J. et al**, 2011, MNRAS, 412, 1441

[41] **Liu D., Wang B., et al.**, 2017, MNRAS, 473, 5352

[42] **Liebendorfer M., Mezzacappa A. et al**, 2011, Phys. Rev. D, 63, 2011

[43] **Limongi M., Chieffi A.**, 2003, ApJ, 592, 404

[44] **Limongi M.**, 2017, Handbook of Supernovae, Athem W. Alsabti, Springer

[45] **Limongi M., Chieffi A.**, 2018, ApJS, 237, 1

[46] **Manucci F., Della Valle M., et al.**, 2005, A&A, 433, 807

[47] **Mezzacappa A., Liebendorfer M. et al**, 2011, Phys. Rev. Lett, 86, 1935

[48] **Minkowskii R.**, 1941, Pub. Astron. Soc. Pacific., 53, 224

[49] **Morozova V., Piro A. L. et al.**, 2015, ApJ, 814, 63

[50] **Nadyozhin D. K.**, 1994, ApJSS, 92, 527

[51] **Osterbrock D. E.**, 2001, Bulletin of the American Astronomical Society, 33, 1330

[52] **Ozel F., Freire P.**, 2016, ARAA, 54, 401

[53] **Podsiadlowski P.**, 1992, Publications of the Astronomical Society of the Pacific, 104, 717

[54] **Podsiadlowski P., Hsu J.J.L. et al.**, 1993, Nature, 364, 6437

[55] **Popov D. V.**, 1993, ApJ, 414, 712

[56] **Postman M., Coe D. et al.**, 2012, ApJS, 199, 25

[57] **Quimby R.M., et al**, 2011, Nature, 474, 487

[58] **Ruffert M., Janka H.-Th, et al.**, 1994, Astronomische Gesellschaft Abstract Series, 10, 52

[59] **Schmidt B. P., Kirshner R. P. et al.**, 1992, ApJ, 395, 366

[60] **Schmidt B. P., Kirshner R. P. et al.**, 1994, ApJ, 432, 42

[61] **Schwab J., Podsiadlowski P. et al**, 2010, ApJ, 719, 722

[62] **Shaffner-Blelisch J., Sagart I. et al.**, 2009, PoS Confinement, 8, 138

[63] **Shapiro S.L., Tenkolsky S. A.**, 1983, *Black Holes, WD and Neutron Stars*, Wiley Inters Publ.

[64] **Smartt S. J., Gilmore G. F., et al.**, 2002, ApJ, 565, 1089

[65] **Smartt S. J.**, 2009, A&A, 47, 63

[66] **Sukhbold T., Ertl T. et al.**, 2016, ApJ, 821, 138

[67] **Swartx D. A., Sutherland P. G. et al.**, 1995, ApJ, 446, 766

[68] **Tamman G. A., Löffer W. et al.**, 1994, The Astrophysical Journal Supplement Series, 92, 487

[69] **Thorsett S.E., Chakrabarty D.**, 1999, ApJ, 512, 288

[70] **Timmes F. X., Woosley S. E.**, 1997, ApJ, 489, 160

[71] **Timmes F. X., Swesty D.**, 2000, ApJs, 126, 501

[72] **Tomasella L., Cappellaro E., et al.**, 2013, MNRAS, 434(2), 1636

[73] **Utrobin V. P.**, 2007, A&A, 461, 233

[74] **Utrobin V. P., Chungai N. N.**, 2015, A&A, 575, A100

[75] **Utrobin V. P., Wongwathanarat A., et al.**, 2017, ApJ, 846, 1

[76] **Woosley S.E., Bloom J. S.**, 2006, ARAA, 44, 507

[77] **Young T. R.**, 2004, ApJ, 617, 1233

[78] **Zaghloul M. R., Bourham M. A. et al.**, 2000, J. Phys. D: Appl. Phys., 33, 977

[79] **Zeilik M., Gregory S. A.**, 1998, Introductory Astronomy and Astrophysics, 4th edition, Sunders College Publishing

[80] **Zhang W., Woosley S.E. et al**, 2008, ApJ, 679, 639